

Ly α emission in galaxies at $z \simeq 5 - 6$: new insight from *JWST* into the statistical distributions of Ly α properties at the end of reionization[★]

Mengtao Tang^{1†}, Daniel P. Stark¹, Richard S. Ellis², Fengwu Sun¹, Michael Topping¹, Brant Robertson³, Sandro Tacchella^{4,5}, Santiago Arribas⁶, William M. Baker^{4,5}, Rachana Bhatawdekar⁷, Kristan Boyett^{8,9}, Andrew J. Bunker¹⁰, Stéphane Charlot¹¹, Zuyi Chen¹, Jacopo Chevallard¹⁰, Gareth C. Jones¹⁰, Nimisha Kumari¹², Jianwei Lyu¹, Roberto Maiolino^{4,5,2}, Michael V. Maseda¹³, Aayush Saxena^{10,2}, Lily Whitler¹, Christina C. Williams¹⁴, Chris Willott¹⁵ and Joris Witstok^{4,5}

¹ *Steward Observatory, University of Arizona, 933 N Cherry Ave, Tucson, AZ 85721, USA*

² *Department of Physics and Astronomy, University College London, Gower Street, London WC1E 6BT, UK*

³ *Department of Astronomy and Astrophysics, University of California, Santa Cruz, 1156 High Street, Santa Cruz, CA 95064, USA*

⁴ *Kavli Institute for Cosmology, University of Cambridge, Madingley Road, Cambridge, CB3 0HA, UK*

⁵ *Cavendish Laboratory, University of Cambridge, 19 JJ Thomson Avenue, Cambridge, CB3 0HE, UK*

⁶ *Centro de Astrobiología (CAB), CSIC-INTA, Cra. de Ajalvir Km. 4, 28850- Torrejón de Ardoz, Madrid, Spain*

⁷ *European Space Agency (ESA), European Space Astronomy Centre (ESAC), Camino Bajo del Castillo s/n, 28692 Villanueva de la Cañada, Madrid, Spain*

⁸ *School of Physics, University of Melbourne, Parkville 3010, VIC, Australia*

⁹ *ARC Centre of Excellence for All Sky Astrophysics in 3 Dimensions (ASTRO 3D), Australia*

¹⁰ *Department of Physics, University of Oxford, Denys Wilkinson Building, Keble Road, Oxford OX1 3RH, UK*

¹¹ *Sorbonne Université, CNRS, UMR 7095, Institut d'Astrophysique de Paris, 98 bis bd Arago, 75014 Paris, France*

¹² *AURA for European Space Agency, Space Telescope Science Institute, 3700 San Martin Drive, Baltimore, MD, 21210*

¹³ *Department of Astronomy, University of Wisconsin-Madison, 475 N. Charter St., Madison, WI 53706 USA*

¹⁴ *NSF's National Optical-Infrared Astronomy Research Laboratory, 950 North Cherry Avenue, Tucson, AZ 85719, USA*

¹⁵ *NRC Herzberg, 5071 West Saanich Rd, Victoria, BC V9E 2E7, Canada*

Accepted XXX. Received YYY; in original form ZZZ

ABSTRACT

JWST has recently sparked a new era of Ly α spectroscopy, delivering the first measurements of the Ly α escape fraction and velocity profile in typical galaxies at $z \simeq 6 - 10$. These observations offer new prospects for insight into the earliest stages of reionization. But to realize this potential, we need robust models of Ly α properties in galaxies at $z \simeq 5 - 6$ when the IGM is mostly ionized. Here we use new *JWST* observations from the JADES and FRESCO surveys combined with VLT/MUSE and Keck/DEIMOS data to characterize statistical distributions of Ly α velocity offsets, escape fractions, and EWs in $z \simeq 5 - 6$ galaxies. We find that galaxies with large Ly α escape fractions (> 0.2) are common at $z \simeq 5 - 6$, comprising 30 per cent of Lyman break selected samples. Comparing to literature studies, our census suggests that Ly α becomes more prevalent in the galaxy population toward higher redshift from $z \sim 3$ to $z \sim 6$, although we find that this evolution slows considerably between $z \sim 5$ and $z \sim 6$, consistent with modest attenuation from residual H I in the mostly ionized IGM at $z \simeq 5 - 6$. We find significant evolution in Ly α velocity profiles between $z \simeq 2 - 3$ and $z \simeq 5 - 6$, likely reflecting the influence of resonant scattering from residual intergalactic H I on the escape of Ly α emission near line center. This effect will make it challenging to use Ly α peak offsets as a probe of Lyman continuum leakage at $z \simeq 5 - 6$. We use our $z \simeq 5 - 6$ Ly α distributions to make predictions for typical Ly α properties at $z \gtrsim 8$ and discuss implications of a recently-discovered Ly α emitter at $z \simeq 8.5$ with a small peak velocity offset (156 km s^{-1}).

Key words: galaxies: evolution - galaxies: high-redshift - dark ages, reionization, first stars - cosmology: observations.

★ Some of the data presented herein were obtained at Keck Observatory, which is a private 501(c)3 non-profit organization operated as a scientific partnership among the California Institute of Technology, the University of California, and the National Aeronautics and Space Administration. The Ob-

servatory was made possible by the generous financial support of the W. M. Keck Foundation.

† E-mail: tangmtasua@arizona.edu

1 INTRODUCTION

Understanding the reionization of the hydrogen in the intergalactic medium (IGM) offers key clues to investigating the early history of structure formation. Over the past two decades, plenty of observational efforts have been made to constrain the history of reionization (see Stark 2016; Robertson 2022; Fan et al. 2023 for reviews). Measurements of the electron scattering optical depth faced by cosmic microwave background photons imply a mid-point of reionization at $z \approx 7.7$ (Planck Collaboration et al. 2020). Observations of quasar absorption spectra suggest that the IGM is partially neutral at $z \gtrsim 7$ (e.g., Bañados et al. 2018; Davies et al. 2018; Wang et al. 2020; Yang et al. 2020a; Greig et al. 2022) and indicate that the reionization of the intergalactic hydrogen likely comes to an end fairly late at $z \approx 5.5$ or below (e.g., Worseck et al. 2014; Becker et al. 2021; Bosman et al. 2022; Zhu et al. 2023).

Lyman-alpha ($\text{Ly}\alpha$, rest-frame $\lambda = 1215.67 \text{ \AA}$) emission from high-redshift galaxies provides another useful probe of the timeline of cosmic reionization (see Dijkstra 2014 and Ouchi et al. 2020 for reviews). Because the cross section for scattering by neutral hydrogen (HI) is large, $\text{Ly}\alpha$ photons from galaxies in the reionization era should be strongly suppressed by the damping wings of the partially neutral IGM (e.g., Miralda-Escudé 1998; Garel et al. 2021). Spectroscopic observations have shown that strong $\text{Ly}\alpha$ emitting galaxies (with $\text{Ly}\alpha$ equivalent width $\text{EW} \gtrsim 25 \text{ \AA}$) become much rarer from $z \approx 6$ to $z \gtrsim 7$ (e.g., Stark et al. 2010; Ono et al. 2012; Treu et al. 2013; Schenker et al. 2014; Pentericci et al. 2018; Kusakabe et al. 2020; Jones et al. 2024). Narrowband surveys have also demonstrated that the $\text{Ly}\alpha$ luminosity function declines between $z \approx 6$ and $z \approx 7$ (e.g., Ouchi et al. 2010; Santos et al. 2016; Ota et al. 2017; Konno et al. 2018). These observations suggest that the IGM transfers from significantly neutral (with neutral fraction $x_{\text{HI}} \gtrsim 0.5$) at $z \gtrsim 7$ (e.g., Mason et al. 2018a; Hoag et al. 2019; Whitler et al. 2020; Morales et al. 2021; Bolan et al. 2022) to highly ionized at $z \approx 5 - 6$, consistent with the evolution implied from quasar spectra.

Attention has recently been focusing on the small subset of galaxies with $\text{Ly}\alpha$ detections at $z \gtrsim 7$ (e.g., Oesch et al. 2015; Zitrin et al. 2015; Roberts-Borsani et al. 2016; Stark et al. 2017; Larson et al. 2022). Galaxies situated in ionized bubbles will have their $\text{Ly}\alpha$ emission redshifted significantly before encountering neutral hydrogen, greatly reducing the attenuation provided by the IGM. As such, $\text{Ly}\alpha$ emitters (LAEs) at $z \gtrsim 7$ are thought to provide signposts of early ionized regions in the mostly neutral IGM (e.g., Wyithe & Loeb 2005; Furlanetto et al. 2006). The larger the ionized bubble, the more that $\text{Ly}\alpha$ will be transmitted through the IGM (e.g., Dijkstra et al. 2007; Mason & Gronke 2020). Systematic searches for $\text{Ly}\alpha$ over wide ($> 1 \text{ deg}^2$) areas have been conducted at $z \gtrsim 7$, either spectroscopically following up ultraviolet (UV) continuum selected galaxies (e.g., Endsley et al. 2021; Endsley & Stark 2022; Cooper et al. 2023) or via narrowband filters that efficiently pick up line emitters (e.g., Zheng et al. 2017; Itoh et al. 2018; Goto et al. 2021). The results have uncovered a variety of likely ionized regions (e.g., Endsley et al. 2021; Jung et al. 2022; Cooper et al. 2023). Perhaps the most compelling of these surrounds an overdensity of galaxies spanning $11 \times 15 \text{ arcmin}^2$ in the 1.5 deg^2 Cosmic Evolution Survey (COSMOS) field. Spectroscopic follow-up has revealed that 9 of 10 $z \approx 7$ galaxies exhibit strong $\text{Ly}\alpha$ emission (Endsley & Stark 2022), well above the success rate typically found at these redshifts. These results are consistent with expectations for an ionized bubble spanning a radius of ≈ 3 physical Mpc (pMpc), carved out by an abundant population of faint galaxies.

JWST (Gardner et al. 2023) has now ushered in a new era of $\text{Ly}\alpha$

observations. Initial results have revealed $\text{Ly}\alpha$ out to $z \approx 11$ (Bunker et al. 2023b), while also confirming the downturn in $\text{Ly}\alpha$ emission at $z \gtrsim 7$ (e.g., Chen et al. 2024; Jones et al. 2024; Nakane et al. 2024). Among the most exciting early results have been detections of extremely strong $\text{Ly}\alpha$ emission at $z \approx 7 - 8$ where the IGM is expected to be significantly neutral (Fujimoto et al. 2023; Saxena et al. 2023; Chen et al. 2024). The rest-frame EWs of $\text{Ly}\alpha$ in these galaxies ($\approx 200 - 400 \text{ \AA}$) are close to the maximum intrinsic values expected for star forming galaxies (see Chen et al. 2024), suggesting that these galaxies must have large ($\gtrsim 1 \text{ pMpc}$) ionized sightlines that allow the majority of their $\text{Ly}\alpha$ emission to be transmitted through the IGM. Recent work has begun to identify large galaxy overdensities in $\gtrsim 1 \text{ arcmin}^2$ areas around the strong $\text{Ly}\alpha$ emitters (e.g., Endsley et al. 2023a; Chen et al. 2024; Whitler et al. 2024), consistent with the source requirements for carving out such a large ionized bubble.

The spectroscopic capabilities of *JWST* with the Near Infrared Spectrograph (NIRSpec; Jakobsen et al. 2022) or the Near Infrared Camera (NIRCam; Rieke et al. 2023a) grisms (Greene et al. 2017) have also introduced new methods for characterizing $\text{Ly}\alpha$ in early galaxies. Rest-frame optical spectra enable detection of hydrogen Balmer lines (i.e., $\text{H}\alpha$, $\text{H}\beta$) from which the intrinsic $\text{Ly}\alpha$ luminosity can be predicted under nominal recombination assumptions. Comparison to the observed $\text{Ly}\alpha$ flux yields the escape fraction of $\text{Ly}\alpha$. We expect this quantity to decrease at redshifts where the IGM is significantly neutral (see Chen et al. 2024). The emission line spectra also constrain the systemic redshift, allowing the velocity profile of $\text{Ly}\alpha$ to be computed. Typically $\text{Ly}\alpha$ emission emerges redshifted from the line center, reflecting transfer through outflowing neutral gas (e.g., Verhamme et al. 2006; Dijkstra 2014). As the IGM becomes neutral, the $\text{Ly}\alpha$ profiles will be further altered as the H I damping wing will preferentially scatter photons near the line center. As a result, we should only expect to see $\text{Ly}\alpha$ emerging near the systemic redshift if galaxies are situated in very large bubbles (Saxena et al. 2023). $\text{Ly}\alpha$ velocity profiles thus provide an independent method for mapping ionized bubbles across *JWST* deep imaging fields (Lu et al. 2024).

The results described above underscore the potential of *JWST* for advancing our understanding of reionization. But if we are to realize this potential, we must extract the imprint of reionization on the distribution of $\text{Ly}\alpha$ strengths and velocity profiles. This task requires a robust “intrinsic¹ model” of $\text{Ly}\alpha$ in galaxies just after reionization (i.e., at $z \approx 5 - 6$), when the IGM is mostly ionized. Over the past decade, large spectroscopic campaigns with Keck and Very Large Telescope (VLT) have taken steps toward establishing an intrinsic model for $\text{Ly}\alpha$ emission in star forming galaxies (e.g., Vanzella et al. 2009; Stark et al. 2010, 2011; Bacon et al. 2017; Pentericci et al. 2018; Urrutia et al. 2019). In addition to measuring the EW distribution of $\text{Ly}\alpha$ near the end of reionization, these observations have quantified how the intrinsic $\text{Ly}\alpha$ distributions are likely to change as galaxy properties (i.e., dust attenuation, stellar population age) evolve at $z \gtrsim 6$. With these datasets in hand, $\text{Ly}\alpha$ measurements at $z \gtrsim 7$ have been effectively mapped to constraints on both IGM neutral fractions (e.g., Mesinger et al. 2015; Mason et al. 2018a; Bolan et al. 2022; Jones et al. 2024; Nakane et al. 2024) and ionized bubble sizes in the vicinity of known $\text{Ly}\alpha$ emitters (e.g., Tilvi et al. 2020; Jung et al. 2022; Leonova et al. 2022; Tang et al. 2023; Chen et al. 2024; Whitler et al. 2024; Witstok et al. 2024b).

¹ Here we refer to intrinsic as the $\text{Ly}\alpha$ emission that would emerge from galaxies if surrounded by the ionized IGM at the end of reionization. This includes processing through the circumgalactic medium and the ionized IGM.

Unfortunately, the intrinsic Ly α models developed over the last decade are not equipped to interpret the large body of data that *JWST* is now providing at $z \gtrsim 7$. Ly α escape fractions and velocity profiles are now routinely measured at $z \gtrsim 7$ (e.g., Bunker et al. 2023b; Jung et al. 2023; Tang et al. 2023; Chen et al. 2024; Saxena et al. 2024), but we currently have no statistical knowledge of the distribution of either quantity in galaxies at $z \simeq 5 - 6$. While the Ly α datasets are sufficiently deep at these redshifts, measurements of velocity profiles (requiring systemic redshifts) and Ly α escape fractions (requiring hydrogen Balmer lines) have never been possible prior to *JWST*. Even interpretation of Ly α EWs faces challenges. The current intrinsic $z \simeq 5 - 6$ models have largely been derived from bright galaxies ($H < 27$) for which continuum measurements were possible with the *Hubble Space Telescope* (*HST*). However, *JWST* spectroscopic measurements at $z \gtrsim 7$ are rapidly pushing to fainter galaxies ($H = 27 - 30$), with several of these showing extremely intense Ly α emission that likely indicates location in a large ionized bubble (Saxena et al. 2023; Chen et al. 2024). We expect to see enhanced Ly α emission in the vicinity of these strong Ly α emitters, with the IGM transmission increasing in lockstep with the bubble radius. But without knowledge of the Ly α EW distribution in similarly low luminosity samples at $z \simeq 5 - 6$, it will be impossible to reliably use $z \gtrsim 7$ measurements to compute the size of ionized regions around strong Ly α emitters.

In this paper, we use new *JWST* data to improve our understanding of the Ly α properties in galaxies at $z \simeq 5 - 6$, with the ultimate goal of developing the intrinsic models necessary to interpret the Ly α measurements now being obtained at $z \gtrsim 7$ with *JWST*. Our parent sample is based on deep Ly α spectroscopy that has been conducted in the Great Observatories Origins Deep Survey (GOODS; Giavalisco et al. 2004) North (Stark et al. 2010, 2011) and South (Bacon et al. 2017, 2023; Urrutia et al. 2019) fields. We use the deep *JWST*/NIRCam imaging in these fields from the *JWST* Advanced Deep Extragalactic Survey (JADES; Eisenstein et al. 2023a) to characterize the physical properties of sources with Ly α spectroscopic constraints. The deep NIRCam photometry also crucially provides the underlying continuum required for extending the Ly α EW distributions to faint galaxies. In addition, we utilize H α measurements obtained in the two GOODS fields from the First Reionization Epoch Spectroscopically Complete Observations (FRESCO) survey (Oesch et al. 2023). FRESCO utilizes *JWST*/NIRCam Wide Field Slitless Spectroscopy (WFSS; Greene et al. 2017), delivering H α emission line measurements for all galaxies in its footprint at $z \simeq 5 - 6$. The FRESCO H α spectra provide the systemic redshifts necessary for mapping the Ly α detections into the rest-frame, delivering our first look at the Ly α velocity profiles in faint galaxies at $z \simeq 5 - 6$. The H α line is also key for predicting the intrinsic Ly α luminosities required for Ly α escape fraction measurements. We compute Ly α escape fractions of $z \simeq 5 - 6$ galaxies using the H α flux from FRESCO and that inferred from color excesses in JADES spectral energy distributions (SEDs; e.g., Simmonds et al. 2024). With this new observational database, we derive statistical distributions of Ly α properties (Ly α EW, Ly α escape fraction) in $z \simeq 5 - 6$ Ly α break selected (hereafter Lyman break selected) samples for use in interpreting emerging $z \gtrsim 7$ measurements.

The organization of this paper is as follows. In Section 2, we describe a sample of Ly α emitters with H α emission line measurements at $z \simeq 5 - 6$. We characterize the Ly α properties (EW, escape fraction, and velocity profile) of sources in our Ly α emitter sample and discuss the impact of neutral hydrogen and dust in Section 3. We then introduce a more general, Lyman break selected galaxy population at $z \simeq 5 - 6$ and derive the Ly α EW and Ly α escape fraction distri-

butions in Section 4, seeking to explore how frequently the typical $z \simeq 5 - 6$ galaxies show large Ly α EWs and Ly α escape fractions. Using our $z \simeq 5 - 6$ sample as a baseline, we discuss the implications for early ionized regions around Ly α emitters in the reionization era in Section 5. Finally, we summarize our conclusions in Section 6. Throughout the paper we adopt a Λ -dominated, flat universe with $\Omega_\Lambda = 0.7$, $\Omega_M = 0.3$, and $H_0 = 70 \text{ km s}^{-1} \text{ Mpc}^{-1}$. All magnitudes are quoted in the AB system (Oke & Gunn 1983) and all EWs are quoted in the rest frame.

2 DATA AND ANALYSIS

In this section, we assemble and analyze a sample of Ly α emitters with *JWST* measurements of the H α strength and redshift. We describe the construction of our sample in Section 2.1, and measurements of Ly α emission line flux in Section 2.2. We fit the NIRCam-based SEDs of the Ly α emitters in Section 2.3. Utilizing the new H α measurements to constrain intrinsic Ly α luminosities and systemic redshifts, we characterize the Ly α escape fraction and Ly α velocity offset. We also use the continuum constrained by NIRCam photometry to derive the Ly α EW. The methodology of these measurements is described in Section 2.4.

2.1 Selection of Ly α emitter sample at $z \simeq 5 - 6$

Our sample consists of Ly α emitting galaxies in the two GOODS fields. We describe the Ly α emitters in GOODS-South in Section 2.1.1 and GOODS-North in Section 2.1.2.

2.1.1 Ly α emitter sample in GOODS-South

There have been numerous Ly α surveys in GOODS-South. In GOODS-South, our analysis centers on the publicly available MUSE-Wide² (Herenz et al. 2017; Urrutia et al. 2019) and MUSE-Deep³ (Bacon et al. 2017, 2023; Inami et al. 2017) surveys. These programs identify Ly α emitters using the integral field spectrograph Multi Unit Spectroscopic Explorer (MUSE; Bacon et al. 2010) at VLT. The Wide Field Mode was used in the surveys, which has a 1 arcmin \times 1 arcmin field of view. MUSE covers the wavelength in optical from 4750 Å to 9350 Å, with an average spectral resolution of ~ 2.5 Å (corresponding to a velocity resolution of $\simeq 100 \text{ km s}^{-1}$ at $\lambda \simeq 7000$ Å). The wavelength range of MUSE allows the detection of Ly α emission in galaxies at $2.9 < z < 6.7$.

The MUSE-Wide survey provides a relatively shallower dataset covering a wider area than MUSE-Deep. The current MUSE-Wide survey covers an area of $\sim 44 \text{ arcmin}^2$ with 44 pointings, with 1 hour exposure time on each pointing. This results in a 5σ emission line detection limit of $\simeq 2 \times 10^{-18} \text{ erg s}^{-1} \text{ cm}^{-2}$ for point sources. The MUSE-Deep survey focuses on the *Hubble* Ultra Deep Field (HUDF; Beckwith et al. 2006), providing much deeper data over a smaller area. MUSE-Deep has released three datasets (all of which we use): a 9-pointing campaign with 10-hour exposure times (MOSAIC; Bacon et al. 2017), a single 31-hour pointing (UDF-10; Bacon et al. 2017), and a new, deeper 141-hour pointing MUSE eXtremely Deep Field (MXDF; Bacon et al. 2023). The 5σ detection limits for point sources are 5×10^{-19} , 2.5×10^{-19} , and $1 \times 10^{-19} \text{ erg s}^{-1} \text{ cm}^{-2}$ in MOSAIC, UDF-10, and MXDF, respectively. We refer readers to Urrutia et al.

² <https://musewide.aip.de/>

³ <https://amused.univ-lyon1.fr/>

(2019) for a full description of the data reduction process for MUSE-Wide, and Bacon et al. (2017, 2023) for MUSE-Deep. In total, there are 479 and 1308 Ly α emitting galaxies at $2.9 < z < 6.7$ with Ly α line S/N > 5 in the MUSE-Wide and Deep catalogs, respectively. The MUSE-Wide survey mainly identifies the more rare luminous Ly α emitters with Ly α luminosity brighter than the L^* of the Ly α luminosity function at $3 < z < 6$ ($L^* \sim 10^{42.2}$ erg s $^{-1}$; Herenz et al. 2019). On the other hand, the MUSE-Deep survey primarily is comprised of the abundant population of sub- L^* LAEs.

In this paper, our focus is on the Ly α properties of galaxies at redshifts at the tail end of reionization ($z \approx 5 - 6$), limiting us to a subset of the total MUSE samples. Rest-frame optical emission lines are important to quantify Ly α properties including the Ly α escape fraction ($f_{\text{esc,Ly}\alpha}$) and the Ly α velocity offset ($\Delta v_{\text{Ly}\alpha}$). We use the available *JWST*/NIRCam F444W grism spectra obtained from the FRESCO survey to measure the rest-frame optical emission lines of MUSE Ly α emitters. Given the wavelength coverage of F444W grism (3.8 – 5.1 μm), we focus on the redshift range at $4.9 < z < 6.5$ to allow H α detection. Among the 479 and 1308 Ly α emitters in the MUSE-Wide and MUSE-Deep surveys, there are 69 and 289 galaxies at $4.9 < z < 6.5$, respectively. We find 3 duplicates between MUSE-Wide and MUSE-Deep sources, leaving $69 + 289 - 3 = 355$ MUSE identified Ly α emitters at $4.9 < z < 6.5$ in total.

We now identify a Ly α selected sample with H α line detections in GOODS-South at $4.9 < z < 6.5$. We cross-match the MUSE Ly α emitter catalog to the NIRCam grism emission line catalog based on a joint analysis of FRESCO and JADES data (Sun et al. in prep.). We visually inspect the MUSE Ly α narrowband image and NIRCam F444W image (Sun et al. in prep.) of each Ly α emitter and identify the matched NIRCam source. Among the 355 MUSE Ly α emitters at $4.9 < z < 6.5$, there are 82 sources with H α emission line detections (here an H α detection refers to an H α line detected in the NIRCam grism spectrum). For the remaining 273 Ly α emitters, the H α emission lines are not detected either because the expected position of H α is out of the individual F444W grism spectra or the H α fluxes are below the FRESCO detection limit (5σ emission line sensitivity $\sim 2 \times 10^{-18}$ erg s $^{-1}$ cm $^{-2}$ for a point source; Oesch et al. 2023). In order to derive the Ly α properties, we also need to measure the Ly α flux and Ly α redshift accurately. Therefore, we removed 18 galaxies whose Ly α emission lines are contaminated by sky line residuals. We also removed four objects identified as active galactic nuclei (AGN) (Lyu et al. 2024; Matthee et al. 2024), leaving a final sample containing 60 galaxies with both Ly α and H α detections at $4.9 < z < 6.5$ in GOODS-South. In Section 3 we will primarily focus on this sample, but we will also discuss the potential bias of this sample relative to the entire Ly α emitting galaxy sample (i.e., including both sources with and without H α detection) therein.

2.1.2 Ly α emitter sample in GOODS-North

In addition to the Ly α emitters identified from the public VLT/MUSE catalogs targeting the GOODS-South field, we also include Ly α emitters at $4.9 < z < 6.5$ in the GOODS-North field identified from a large spectroscopic survey taken with the DEep Imaging Multi-Object Spectrograph (DEIMOS; Faber et al. 2003) at the Keck II telescope. We direct readers to Stark et al. (2010) and Stark et al. (2011) for detailed descriptions of the survey. Below we briefly summarize the DEIMOS spectra. Our Keck/DEIMOS survey targeted *B*-, *V*-, and *i*-band dropouts (i.e., $z \sim 4 - 6$ Lyman break galaxies). The dropouts were identified in Stark et al. (2009) utilizing the standard color selection criteria. The follow-up DEIMOS spectroscopic observations were performed between 2008 and 2015 with eight

multi-object slitmasks. The slit width is 1.0 arcsec. Seven masks primarily targeting *B*- and *V*-band dropouts ($z_{\text{phot}} \sim 4 - 5$) were observed using the 600 line/mm grating blazed at 7500 Å, covering wavelength 4850 – 10150 Å with a resolution of 3.5 Å (velocity resolution ≈ 140 km s $^{-1}$). The remaining mask primarily targets *i*-band dropouts ($z_{\text{phot}} \sim 6$), and was observed using the 830 line/mm grating blazed at 8640 Å covering 6800 – 10100 Å (spectral resolution = 2.5 Å, corresponding to velocity resolution ≈ 87 km s $^{-1}$). The on-target integration time of each mask is between 3 and 12.5 hours with an average seeing = 0.5 – 1.1 arcsec, resulting in 5σ Ly α line flux limits of $0.3 - 2.0 \times 10^{-17}$ erg s $^{-1}$ cm $^{-2}$. The DEIMOS spectra were reduced following the methodology described in Stark et al. (2010). We summarize the DEIMOS observations in Table 1.

We visually inspect the DEIMOS spectrum of each galaxy to search for Ly α emission lines. We identify Ly α emission in 220 galaxies at $3 < z < 6.5$, including 32 Ly α emitters at $4.9 < z < 6.5$. Similar to our MUSE sample, we cross-match these 32 galaxies to the NIRCam grism emission line catalog in Sun et al. (in prep.) in GOODS-North and find H α detections in 29 of them. For the remaining three systems without an H α detection, two of them have H α flux below the detection limit, and the expected H α position of another one is shifted out of its F444W grism spectrum. Again, we removed 9 sources for which the Ly α emission lines are contaminated by sky line residuals, and one AGN identified in Matthee et al. (2024). This leaves a sample of 19 galaxies with both Ly α and H α detections at $4.9 < z < 6.5$ in GOODS-North. Combining with the sample in GOODS-South, we have identified 79 Ly α emitting galaxies with H α detections at $4.9 < z < 6.5$. We list these 79 systems in Table A1.

2.2 Measurements of Ly α flux

For the 79 galaxies with Ly α and H α detections at $4.9 < z < 6.5$ in our sample, we measure their Ly α emission line fluxes from MUSE or DEIMOS spectra in a self-consistent way. Before analyzing the Ly α fluxes of our sources, we first consider the potential aperture loss for Ly α emission. We then present the measurements of Ly α fluxes.

For the 60 VLT/MUSE sources in our $4.9 < z < 6.5$ sample, we take advantage of the 1D MUSE spectra extracted and published by the MUSE-Wide (Urrutia et al. 2019) and MUSE-Deep (Bacon et al. 2023) teams. For objects in MUSE-Wide, we use the point spread function (PSF; full width at half maximum FWHM ≈ 0.7 arcsec for MUSE) weighted 1D spectra extracted with the LSDCat software (Herenz & Wisotzki 2017) from the 3D MUSE data cube by Urrutia et al. (2019). For objects in MUSE-Deep, we use the reference spectra provided by Bacon et al. (2023). Among the extractions used in Bacon et al. (2023), the ORIGIN algorithm (Mary et al. 2020) is primarily favored for extracting spectra of Ly α emitters. The reference spectra of the most of our MUSE-Deep sources (29 out of 36) are extracted with ORIGIN. Source blending increases in deep exposures, and the spectra of blended sources are better extracted with the de-blended algorithm (Bacon et al. 2023). There are 5 blended sources (MUSE-547, MUSE-2071, MUSE-6294, MUSE-6462, and MUSE-7125) in our MUSE-Deep sample, and their reference spectra are extracted with the de-blended algorithm ODIN. For galaxies with very bright Ly α emission, the spectra are best extracted with the NBEXT algorithm (Bacon et al. 2023). MUSE-68 and MUSE-7605 are the two bright Ly α emitters in our MUSE-Deep sample, and their spectra are extracted with NBEXT. Comparing the MUSE-Wide and MUSE-Deep spectra for duplicates, we find that the Ly α emission line profiles extracted from MUSE-Wide and MUSE-Deep are consistent. The

Mask ID	R.A. (hh:mm:ss)	Decl. (dd:mm:ss)	Date	Exposure Time (s)	N_{dropout}	Grating (line/mm)	Seeing (arcsec)
gn_A	12:37:06.02	+62:16:33.2	April 2008	21600	94	600	1.0
gn_B	12:37:16.83	+62:15:00.4	April 2008	21600	107	600	0.8
gn_C	12:37:16.29	+62:15:04.9	April 2008	20400	100	600	1.1
kcGNv1B	12:37:02.14	+62:13:48.1	March 2009	18000	108	600	1.0
kcGNv2B	12:36:55.53	+62:14:24.9	March 2009	25200	79	600	0.5
GNm1v5	12:36:54.84	+62:14:11.6	April 2010	45000	23	830	0.8
Bdrop	12:36:46.16	+62:13:26.3	June 2012	16800	73	600	1.0
GN_AZ	12:37:15.18	+62:14:19.0	March 2015	10800	79	600	1.0

Table 1. Summary of Keck/DEIMOS observations of $z \simeq 4 - 6$ dropouts in the GOODS-North field. Observations were taken in between 2008 and 2015. N_{dropout} represents the number of B -, V -, and i -band dropouts (primary targets) placed on each mask.

difference of Ly α fluxes measured between the MUSE-Wide and MUSE-Deep spectra of duplicates is less than 10 per cent.

We consider the effects of aperture loss of Ly α fluxes measured by MUSE. It has been established that Ly α emitting galaxies are commonly surrounded by extended Ly α halos (e.g., Matsuda et al. 2012; Hayes et al. 2013; Momose et al. 2014; Matthee et al. 2016; Wisotzki et al. 2016; Leclercq et al. 2017; Wu et al. 2020; Guo et al. 2023; Zhang et al. 2024). From the segmentation maps (used to extract 1D spectra) published by Urrutia et al. (2019) and Bacon et al. (2023), we find that the MUSE spectra extraction apertures of our $z \simeq 5 - 6$ Ly α emitters have a median diameter = 1.5 arcsec. The Ly α line flux measured within the above mentioned MUSE aperture (as well as slit spectrographs including Keck/DEIMOS and the JWST/NIRSpec) could miss a portion of the flux from the Ly α halo. Here we estimate the ratio of Ly α flux recovered by MUSE measurements to the total Ly α flux. To do this, we generate a Ly α surface brightness profile for a typical galaxy at $z \simeq 5 - 6$ based on the Ly α halo measurements in Leclercq et al. (2017) and estimate the fraction of the Ly α flux within the MUSE aperture. Leclercq et al. (2017) fit individual Ly α surface brightness profile with a two-component model (a core and a halo), each described by an exponentially decreasing distribution. About 65 per cent of the total Ly α flux comes from the halo. The median scale length of the halo is 3.8 kpc at $z \simeq 5 - 6$, while the average scale length of the core is $\simeq 1/10$ of the halo scale length. Then we create the Ly α surface brightness profile based on the above parameters, assuming exponential decreasing distributions for both the core and the halo component. After convolving with MUSE PSF, we estimate that about 75 per cent of the total Ly α flux for a $z \simeq 5 - 6$ galaxy will be recovered when extracting the line flux using the MUSE aperture.

Similarly, the Keck/DEIMOS slit spectra should also miss a portion of the total Ly α flux due to the slit loss. We estimate the DEIMOS slit loss for Ly α flux following the same procedures for estimating MUSE aperture loss. We note that our DEIMOS sources are brighter than our MUSE sources (median absolute UV magnitude $M_{\text{UV}} = -19.6$ for DEIMOS vs. $M_{\text{UV}} = -18.8$ for MUSE). However, Leclercq et al. (2017) show that the Ly α halo scale length does not change significantly with M_{UV} . Therefore, we use the same Ly α surface brightness profile model generated utilizing the parameters measured in Leclercq et al. (2017) to estimate the fraction of in-slit light. We find that $\simeq 57$ per cent of the total Ly α flux will be recovered within the 1.0 arcsec width DEIMOS slit. Here we note that the MUSE or DEIMOS aperture loss of Ly α flux is estimated based on the median parameters of Ly α surface brightness profile measurements at $z \simeq 5 - 6$, and thus it could vary among individual sources. Taking the Ly α halo scale length range of $z \simeq 5 - 6$ Ly α emitters (1 – 10 kpc) reported in Leclercq et al. (2017), we estimate that the fraction of total Ly α flux recovered by MUSE (1 arcsec width

DEIMOS slit) measurement ranges from 61 to 86 per cent (44 to 63 per cent). This suggests the true total flux may vary by 0.8 – 1.1 \times relative to that derived in this paper.

We now derive the Ly α fluxes of the 79 Ly α emitters at $4.9 < z < 6.5$ in our sample. Because the Ly α emission line profile at high redshift can be complex, we compute the line flux by directly integrating the flux between rest-frame 1212 Å and 1220 Å ($\simeq \pm 1000$ km s $^{-1}$ in velocity space). This wavelength window captures the total Ly α flux for Ly α emitting galaxies (e.g., Du et al. 2020; Matthee et al. 2021). We next examine the impact of the underlying continuum to the integrated Ly α line flux. For all the 79 galaxies, the continua measured from spectra are faint with relatively low S/N (< 5). Therefore, we estimate the underlying continuum flux densities using the available JWST/NIRCam or HST photometry (Section 2.4). We find that the continua make negligible changes (< 10 per cent) to the integrated Ly α fluxes of these 79 Ly α emitters. Motivated by these, we do not subtract the underlying continua from the integrated Ly α fluxes for our Ly α emitters.

The observed Ly α fluxes of the 60 MUSE sources in our sample range from 1.2×10^{-18} to 5.5×10^{-17} erg s $^{-1}$ cm $^{-2}$. These Ly α fluxes are similar to those presented in the MUSE-Wide and Deep data catalogs in Urrutia et al. (2019) and Bacon et al. (2023), with differences < 0.1 dex for all the 60 MUSE sources. To ensure the Ly α fluxes of MUSE and DEIMOS sources are measured in a self-consistent way, we will adopt our own Ly α flux measurements throughout the paper. For the 19 DEIMOS sources, the observed Ly α fluxes are from 2.8×10^{-18} to 3.5×10^{-17} erg s $^{-1}$ cm $^{-2}$. In order to be consistent with the MUSE measurements, we convert the Ly α fluxes measured from the DEIMOS slit for the MUSE aperture. Using the aperture losses estimated for DEIMOS 1.0 arcsec slit and MUSE aperture, we multiply the observed DEIMOS Ly α fluxes by a factor of $0.75/0.57 = 1.3$. After conversion, the Ly α fluxes of the 19 DEIMOS Ly α emitters are from 3.6×10^{-18} to 4.6×10^{-17} erg s $^{-1}$ cm $^{-2}$. To evaluate the uncertainties of Ly α fluxes, we resample the flux densities of each spectrum 1000 times by taking the observed flux densities as mean values and the errors as standard deviations. We measure the Ly α fluxes from the resampled spectra of each source using the same methods and take the standard deviation as the uncertainty. In Table A1, we list the Ly α fluxes of the 79 galaxies with both Ly α and H α detections at $4.9 < z < 6.5$.

One of the primary goals of this paper is to provide a baseline for interpreting the Ly α measurements at $z \gtrsim 7$ with JWST/NIRSpec. Therefore, we also need to consider the possible aperture loss for NIRSpec micro-shutter assembly (MSA; Ferruit et al. 2022) observations, and how this compares to MUSE aperture loss. To estimate the NIRSpec MSA aperture loss for Ly α emission, we generate the same Ly α surface brightness profile based on the measurements in

Leclercq et al. (2017) as we did for MUSE and DEIMOS aperture loss estimation. We assume the source is centered in the NIRSpec micro-shutter and convolve the Ly α surface brightness profile with the NIRSpec PSF using the WebbPSF package (Perrin et al. 2014). We estimate that ≈ 50 per cent of the total Ly α flux at $z \approx 5 - 6$ will be recovered by NIRSpec MSA measurement. Considering the *JWST* data reduction pipeline⁴ (Bushouse et al. 2024) will perform an aperture correction assuming a point source, the pipeline corrected Ly α flux will recover ≈ 60 per cent of the total Ly α flux. Comparing to the fraction of Ly α flux recovered by MUSE aperture (≈ 75 per cent), the typical Ly α flux measured with a NIRSpec MSA shutter will be $0.6/0.75 = 80$ per cent of the flux measured with MUSE. We note that if the source is not centered in the MSA shutter, there will be a 10–20 per cent systematic uncertainty as the NIRSpec PSF depends on the position of the target in the shutter (e.g., de Graaff et al. 2024). We test the aperture losses by cross-matching $z \approx 5 - 6$ Ly α emitters identified in MUSE surveys to the public NIRSpec survey (Bunker et al. 2023a; Saxena et al. 2024; Witstok et al. 2024b). There are three matched Ly α emitters (all in the HUDF field): MUSE-852 (ID 16625 in Saxena et al. 2024; Witstok et al. 2024b), MUSE-3089 (ID 9365), and MUSE-6231 (ID 14123). We find that the NIRSpec Ly α fluxes of these sources are $\approx 70 - 80$ per cent of the fluxes measured from MUSE, which is consistent with the NIRSpec to MUSE flux ratio estimated from aperture loss (≈ 80 per cent). In the future, a larger reference sample is required to estimate the aperture correction between Ly α measured from IFU and slit spectroscopy.

2.3 SED fitting of Ly α emitter sample

To derive the physical properties of the 79 galaxies with Ly α and H α detections in our $4.9 < z < 6.5$ sample, we fit their available SEDs with stellar population and photoionization models. We utilize the *JWST*/NIRCam imaging taken as a part of the JADES observations targeting the two GOODS fields. The current JADES NIRCam observations utilizes nine NIRCam filters (F090W, F115W, F150W, F200W, F277W, F335M, F356W, F410M, and F444W), covering a wavelength range of $0.8 - 5.0 \mu\text{m}$. The JADES NIRCam data reduction is introduced in literature (Eisenstein et al. 2023a; Rieke et al. 2023b; Robertson et al. 2023; Tacchella et al. 2023b), and will be fully described in Tacchella et al. (in prep.). Among the 79 Ly α emitters with H α detections at $4.9 < z < 6.5$ in our sample, 61 lie in the JADES NIRCam footprint (52/60 in GOODS-South and 9/19 in GOODS-North). For these 61 Ly α emitters, we visually inspect the MUSE Ly α narrowband images or the *HST* images used to select DEIMOS targets (Stark et al. 2010; see also Section 2.1.2) with JADES NIRCam images. We have identified JADES NIRCam counterparts for all these 61 galaxies. For each of these 61 galaxies, we take advantage of the F090W to F444W photometry provided in the JADES photometry catalog (Rieke et al. 2023b; Robertson et al. in prep.).

We use the JADES 0.2 arcsec diameter circular aperture (“CIRC1”) fluxes to compute the NIRCam colors, which reduces the background noise associated with larger apertures (Hainline et al. 2024b). We also use the CIRC1 fluxes to derive the UV slopes of our sources. The UV slope is computed by fitting a power law ($f_\lambda \propto \lambda^\beta$) to the JADES NIRCam broadband fluxes at rest-frame wavelengths $1250 - 2600 \text{ \AA}$ (Calzetti et al. 1994). Then we use the Kron (Kron 1980) aperture ($k = 2.5$) fluxes, which represent the total fluxes, for SED fitting but keep the CIRC1 colors. We modify the Kron aperture

fluxes using the following procedures. For each object, we compute the median ratio of fluxes measured within $k = 2.5$ Kron apertures to CIRC1 apertures in NIRCam F115W, F150W, and F200W filters. The Kron aperture fluxes used here are corrected to the total fluxes using the NIRCam PSFs (Rieke et al. 2023b). Next, we multiply all the NIRCam CIRC1 fluxes by this factor to obtain the modified Kron aperture fluxes.

We fit the modified JADES NIRCam Kron aperture photometry of the 61 galaxies using the Bayesian galaxy SED modelling and interpreting tool BayEsian Analysis of GaLaxy sEds (BEAGLE, version 0.23.0; Chevallard & Charlot 2016). The BEAGLE setup and SED fitting procedures follow the description in Tang et al. (2023), and we summarize these below. Models used in BEAGLE combine the latest version of the Bruzual & Charlot (2003) stellar population synthesis models and the Gutkin et al. (2016) photoionization models of star-forming galaxies with the CLOUDY code (Ferland et al. 2013). The redshift is fixed to the systemic redshift measured from H α emission lines (Sun et al. in prep.). We assume a constant star formation history (CSFH), allowing the galaxy age to vary between 1 Myr and the age of the Universe at the given redshift with a log-uniform prior. We assume a Chabrier (2003) initial mass function (IMF) with a stellar mass range of $0.1 - 300 M_\odot$. We allow the metallicity to vary in the range $-2.2 \leq \log(Z/Z_\odot) \leq 0.25$ ($Z_\odot = 0.01524$; Caffau et al. 2011) and the dust-to-metal mass ratio (ξ_d) to span the range $\xi_d = 0.1 - 0.5$. The interstellar metallicity is set to be equal to the stellar metallicity. The ionisation parameter U is adjusted in the range $-4.0 \leq \log U \leq -1.0$. We adopt log-uniform priors for metallicity and ionization parameter, and a uniform prior for dust-to-metal mass ratio. We assume the Small Magellanic Cloud (SMC) extinction curve (Pei 1992) to account for the dust attenuation, allowing the V -band optical depth τ_V to vary between 0.001 and 5 with a log-uniform prior. Finally, we adopt the prescription of Inoue et al. (2014) to include the absorption of IGM. When fitting the SEDs, we remove fluxes in filters that lie blueward of Ly α to avoid introducing the uncertain flux contribution from Lyman series emission and absorption.

From the BEAGLE models we derive the median values from the posterior probability distributions and the marginalized 68 per cent credible intervals. For the 61 Ly α emitters at $4.9 < z < 6.5$ with JADES photometry, their SEDs suggest that the light is dominated by very young stellar populations, with luminosity-weighted age ranging from 2 Myr to 263 Myr (median age = 14 Myr) and specific star formation rate (sSFR) = $4 - 575 \text{ Gyr}^{-1}$ (median sSFR = 69 Gyr^{-1}) assuming CSFH. These reflect that our Ly α emitters are likely dominated by a recent burst or upturn in star formation history. The stellar masses derived from BEAGLE CSFH models occupy the relatively low-mass space, with $1.2 \times 10^7 - 9.3 \times 10^8 M_\odot$ (median = $4.7 \times 10^7 M_\odot$). We note that the stellar masses derived from CSFH models correspond to the very young stellar populations which dominate the rest-frame UV to optical SEDs. Older stellar populations can be easily outshined by the light of young stars, but increasing the stellar mass up to over an order of magnitude (e.g., Roberts-Borsani et al. 2020; Laporte et al. 2021; Tacchella et al. 2022, 2023a; Tang et al. 2022; Whitler et al. 2023). However, this effect will not strongly impact the main results presented in this paper (Section 3) because they do not depend on the stellar mass.

We characterize the [O III]+H β EWs using the JADES NIRCam SEDs. From BEAGLE models, we derive the rest-frame [O III]+H β EW = $249 - 5206 \text{ \AA}$ for the 61 Ly α emitters at $4.9 < z < 6.5$, with a median of 1283 \AA . This median [O III]+H β EW is nearly 2 times larger than the average EW of galaxies in the reionization era ($\approx 700 - 800 \text{ \AA}$; e.g., Endsley et al. 2023b,a), similar to that in

⁴ <https://github.com/spacetelescope/jwst>

emission line selected samples ($\simeq 1000 \text{ \AA}$; e.g., Matthee et al. 2023; Rinaldi et al. 2023; Tang et al. 2023). This is consistent with the very young luminosity-weighted ages inferred from models for our Ly α emitters at $4.9 < z < 6.5$ (e.g., Chevallard et al. 2018; Tang et al. 2019, 2023).

The NIRCcam SEDs also constrain the hydrogen ionizing photon production efficiency (ξ_{ion}). Throughout this paper we use the most commonly definition of ξ_{ion} in literature: ξ_{ion} is the hydrogen ionizing photon production rate per unit intrinsic UV luminosity density at rest-frame 1500 \AA (L_{UV}), where L_{UV} is the observed UV luminosity (including both stellar and nebular continuum) corrected for dust attenuation (see Chevallard et al. 2018 for definitions of various ξ_{ion}). We find large ionizing photon production efficiencies for our Ly α emitters at $4.9 < z < 6.5$ (median $\xi_{\text{ion}} \simeq 10^{25.6} \text{ erg}^{-1} \text{ Hz}$), comparable to the $z \gtrsim 6$ population (median $\xi_{\text{ion}} \simeq 10^{25.5-25.7} \text{ erg}^{-1} \text{ Hz}$; e.g., Endsley et al. 2023b; Simmonds et al. 2023; Tang et al. 2023). The results indicate that the majority of our Ly α emitters at $4.9 < z < 6.5$ have hard ionizing spectra. We find that assuming a different SFH (e.g., a burst on top of more evolved stellar population or a non-parametric SFH) in SED fitting does not change the derived ξ_{ion} significantly. In Table A2 we present the galaxies properties inferred from BEAGLE models for the 61 Ly α emitters with H α detection at $4.9 < z < 6.5$.

2.4 Characterization of Ly α emission line properties

Deep *JWST*/NIRCcam imaging observations allow us to constrain the underlying continuum that is essential to derive the Ly α EW. In addition, the H α emission lines measured from NIRCcam grism spectra provide constraints to the intrinsic Ly α luminosity and systemic redshift, enabling us to quantify the Ly α escape fraction and Ly α velocity offset. These properties allow us to investigate the neutral hydrogen and dust distribution of galaxies as well as the ionization state of the surrounding IGM. In the following we derive the Ly α EWs, Ly α escape fractions, and Ly α velocity offsets for the 79 galaxies with Ly α and H α detections at $4.9 < z < 6.5$ in our sample.

We compute the Ly α emission line EWs using the aperture corrected Ly α fluxes derived in Section 2.2 and the underlying continuum flux densities. For the 61 galaxies with JADES NIRCcam observations (Section 2.3), we estimate the continuum from NIRCcam photometry. For the other 18 galaxies we utilize the *HST* broadband photometry obtained from the *Hubble* Legacy Field (HLF; Whitaker et al. 2019) archive, which includes all the *HST* imaging data in the two GOODS fields (e.g., Ellis et al. 2013; Illingworth et al. 2013). We visually inspect the Ly α images of these 18 Ly α emitters with *HST* images, and we find *HST* counterparts for all of them. Then we fit the photometry from filters covering rest-frame $1250 - 2600 \text{ \AA}$ with a power law $f_{\lambda} \propto \lambda^{\beta}$. From the best-fit $f_{\lambda}(\lambda)$ relation we derive the average continuum flux density at rest-frame $1225 - 1250 \text{ \AA}$ (Kornei et al. 2010; Stark et al. 2010). The derived Ly α EWs of the 60 MUSE Ly α emitters with H α detections at $4.9 < z < 6.5$ are from 12 \AA to 534 \AA (rest-frame), with a median value of 111 \AA . The absolute UV magnitudes of our MUSE sources at rest-frame 1500 \AA (M_{UV}) range from -21.3 to -17.2 , with a median $M_{\text{UV}} = -18.7$. For the 19 DEIMOS sources, we compute the Ly α EWs from 11 \AA to 212 \AA with a median EW = 76 \AA after converting the Ly α fluxes measured with DEIMOS slits to the MUSE aperture. The absolute UV magnitudes of these 19 systems are from -21.0 to -18.4 with a median $M_{\text{UV}} = -19.6$. Comparing to our MUSE sources, our DEIMOS sample extends to lower Ly α EW and brighter M_{UV} . The uncertainties of Ly α EWs are estimated by adding the uncertainties of Ly α fluxes (Section 2.2) and the errors of continua in quadrature.

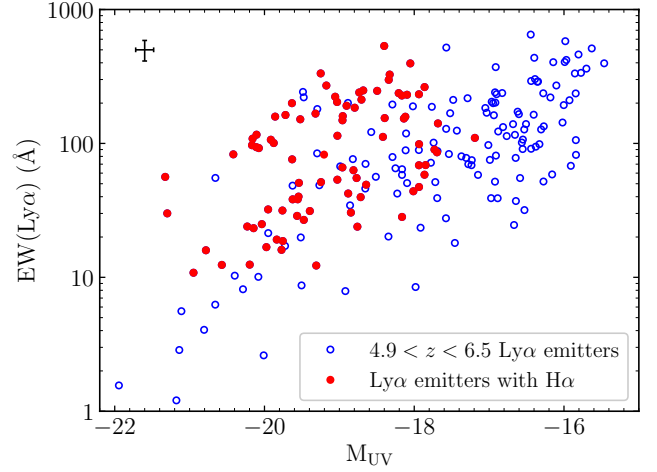


Figure 1. Ly α EW versus absolute UV magnitude (M_{UV}) of all the Ly α emitting galaxies at $4.9 < z < 6.5$ identified from VLT/MUSE (Section 2.1.1) and Keck/DEIMOS (Section 2.1.2) observations (open blue circles). The typical uncertainties are shown as the error bars at the upper left of the figure. We have identified H α detections in 79 galaxies to derive Ly α properties including Ly α escape fraction and Ly α velocity offset. These 79 sources with both Ly α and H α detections are marked by red circles.

We summarize the Ly α EWs in Table A1. In Fig. 1, we show the M_{UV} and Ly α EW for the 79 galaxies with Ly α and H α detections (open red circles).

To compute the Ly α escape fractions, we use the NIRCcam F444W grism spectra obtained from FRESKO observations and processed by Sun et al. (in prep.) to measure the H α luminosities and hence derive the intrinsic Ly α luminosities. For each object, the H α flux was derived by fitting a Gaussian profile to the 1D NIRCcam grism spectrum. The 1D spectrum was optimally extracted (Horne 1986) from the 2D grism spectrum using the 2D emission line profile (Sun et al. in prep.). The typical aperture size for extracting 1D NIRCcam grism spectra is 0.75 arcsec , which is similar to the MUSE aperture size after deconvolving the MUSE PSF (Section 2.2). It has been noticed in Sun et al. (in prep.) that the H α fluxes measured from NIRCcam grism spectra are slightly lower (by a factor of 0.82) than those inferred from NIRCcam imaging. This may be explained if the extended H α emission line component is missed in the over-subtraction of sky continuum (Sun et al. in prep.). To examine this discrepancy, we compare the H α fluxes measured from NIRCcam grism spectra to those inferred from BEAGLE models (Section 2.3) for our objects. We find that the grism measured H α fluxes are on average $0.82\times$ of the fluxes inferred from SED fitting, consistent with the result found in Sun et al. (in prep.). Because the NIRCcam grism spectra allow direct measurement of H α lines that are free of nearby emission lines such as [N II] $\lambda\lambda 6548, 6584$, we still use the spectral measured H α luminosity to infer the intrinsic Ly α luminosity. To correct the spectral measured H α flux to the total flux, we multiply with a factor derived from the comparison between spectral flux and SED inferred value: $1/0.82 = 1.22$.

We then correct the observed H α luminosities for dust attenuation. For the 61 galaxies with JADES NIRCcam photometry measurements, we derive the dust attenuation to the H α emission line ($A_{\text{H}\alpha}$) from BEAGLE models (Table A2). The dust attenuation is low for the $z \simeq 5 - 6$ galaxies with both Ly α and H α detections in our sample, with a median value of $A_{\text{H}\alpha} = 0.007 \text{ mag}$. For the 18 galaxies without

JADES NIRC*am* SEDs, we apply the above median dust attenuation inferred from BEAGLE models of the 61 galaxies with JADES SEDs.

The dust-corrected H α luminosity ($L_{\text{H}\alpha}$) is converted to the intrinsic Ly α luminosity ($L_{\text{Ly}\alpha,\text{int}}$) assuming case B recombination. We apply $L_{\text{Ly}\alpha,\text{int}} = 8.7 \times L_{\text{H}\alpha}$ (see the discussion on the 8.7 factor in Hayes 2015 and Henry et al. 2015) assuming an electron temperature $T_e = 10000$ K and an electron density $n_e = 100 \text{ cm}^{-3}$. The 25 – 50 – 75 per centile values of the computed Ly α escape fractions of our 79 sources are 0.14, 0.26, and 0.54. We note that varying the electron temperature and electron density in $T_e = 5000 - 20000$ K and $n_e = 100 - 1000 \text{ cm}^{-3}$ does not impact the $L_{\text{Ly}\alpha}/L_{\text{H}\alpha}$ ratio and hence the calculated $f_{\text{esc,Ly}\alpha}$ significantly. We also note that assuming case B recombination, which is valid for optically-thick H II regions, may not always be applicable. If a galaxy is leaking a large fraction of Ly α emission through optically-thin H I gas, which might be the case for a subset of our sources with very large Ly α escape fractions (assuming case B recombination), case A recombination may be a better approximation. Assuming case A recombination, we utilize $L_{\text{Ly}\alpha,\text{int}} = 11.4 \times L_{\text{H}\alpha}$ (Osterbrock & Ferland 2006). The resulting Ly α escape fractions are 1.3 times lower than the values derived assuming case B recombination, with 25 – 50 – 75 percentile values = 0.10, 0.20, and 0.41. We list Ly α escape fractions assuming both case B and case A recombination in Table A1. In order to ensure robust comparison with values in the literature (e.g., Hayes et al. 2010; Matthee et al. 2016; Yang et al. 2017; Chen et al. 2024; Saxena et al. 2024), we will adopt Ly α escape fractions assuming case B recombination in the following sections.

We note that the Ly α escape fractions computed here include the contribution from extended Ly α halos. The extended Ly α emission is not only produced by recombinations inside galaxies but also other origins (cooling radiation, Ly α fluorescence, satellite galaxies; e.g., Leclercq et al. 2017; Kusakabe et al. 2020; Leclercq et al. 2020; Herrero Alonso et al. 2023). Although it is difficult to quantify the contribution of each origin, recent simulations suggest that the scattering of Ly α emission produced by recombinations inside the galaxy dominates the inner region ($r < 7$ kpc) at $3 < z < 6$ (Mitchell et al. 2021). Therefore, the Ly α emission covered by our MUSE apertures (radius ≈ 0.75 arcsec, corresponding to $r \lesssim 4.5$ kpc at $z \approx 5 - 6$) is not likely significantly impacted by that from non-recombination origins or nearby sources.

Finally, we quantify the Ly α velocity offset of the 79 galaxies in our $4.9 < z < 6.5$ Ly α -selected sample. The systemic redshifts are derived by fitting the H α emission lines in NIRC*am* grism spectra with Gaussian profiles. We measure the Ly α redshifts ($z_{\text{Ly}\alpha}$) from the peak of the Ly α emission lines identified from VLT/MUSE and Keck/DEIMOS spectra. In order to be consistent with *JWST* measurements, we convert the wavelengths of MUSE and DEIMOS spectra from air to vacuum using the formula in Ryabchikova et al. (2015)⁵, and the Ly α redshifts are derived based on vacuum wavelengths. For the 79 galaxies with Ly α and H α detections in our sample, their Ly α velocity offsets are from $+61 \text{ km s}^{-1}$ to $+725 \text{ km s}^{-1}$. We estimate the uncertainty of Ly α velocity offset following the similar way in estimating the Ly α flux uncertainty. For each galaxy, we resample the flux densities of its spectrum 1000 times and take the standard deviation of Ly α velocity offsets derived from the 1000 resampled spectra as the uncertainty. We note that the wavelength calibration for NIRC*am* grism spectra is also subject to an uncertainty of $\sim 10 - 20 \text{ \AA}$ (Sun et al. in prep.), corresponding to a velocity uncer-

tainty of $\approx 100 \text{ km s}^{-1}$ for F444W grism. This uncertainty randomly scatters the derived velocity offsets but does not systematically shift the velocity offsets to one direction. We summarize the Ly α velocity offsets of the 79 Ly α emitters in our sample in Table A1. In the following section we will discuss the Ly α properties of systems in our Ly α -selected sample at $4.9 < z < 6.5$.

3 THE PROPERTIES OF LY α EMITTERS AT $Z \approx 5 - 6$

Before considering the Ly α properties of the more general (Lyman break selected) population of $z \approx 5 - 6$ galaxies (Section 4), we first use new *JWST* observations to investigate the subset known to show Ly α emission. We characterize the relationship of Ly α EW and Ly α escape fraction in our Ly α emitter sample in Section 3.1, with particular interest in the systems with the largest escape fractions (> 0.5) and largest Ly α EWs ($> 100 \text{ \AA}$). In Section 3.2 and Section 3.3, we quantify the velocity structure of Ly α lines relative to the systemic redshift (determined from new H α redshifts) and discuss the potential impact of the IGM on the line profiles at $z \approx 5 - 6$.

3.1 Galaxies with large Ly α EWs and Ly α escape fractions

Galaxies with extremely large Ly α EWs ($> 100 - 300 \text{ \AA}$) have recently been discovered at $z \gtrsim 7$ (Saxena et al. 2023; Chen et al. 2024), providing signposts of ionized bubbles in the mostly neutral universe. If we are to link these sources to useful information about the early IGM, we will need to understand what separates the most extreme Ly α emitters (EW $> 100 - 300 \text{ \AA}$) from the more commonly-studied population with moderate-EW Ly α (EW = $10 - 50 \text{ \AA}$). Our Ly α emitter sample spans from EW = 10 to 500 \AA (Fig. 1), allowing us to investigate this question at $z \approx 5 - 6$ where the impact of the IGM damping wing on Ly α is minimal.

Prior to interaction with the IGM, the Ly α EW is largely regulated by a combination of ionizing photon production (which sets the intrinsic luminosity of the line) and transmission of line photons through the interstellar medium (ISM) and the circumgalactic medium (CGM). On one hand, we may expect that the strongest Ly α emitters are simply those that are able to transmit most of their Ly α photons through the ISM and CGM. Alternatively, the galaxies with Ly α EW $> 100 \text{ \AA}$ may stand out as those with an extreme population of ionizing sources that are boosting the strength of the line relative to other galaxies (e.g., Maseda et al. 2020, 2023). According to the stellar population synthesis models used in this paper (see Section 2.3), the intrinsic Ly α EW will increase by a factor of 6 between an age of 300 Myr and 2 Myr (here assuming CSFH). This change reflects the difference in the ionizing photon production efficiency (parameterized as ξ_{ion} , the hydrogen ionizing photon production rate per unit intrinsic luminosity density at rest-frame 1500 \AA) in these stellar populations, ranging from $\xi_{\text{ion}} = 10^{25.3} \text{ erg}^{-1} \text{ Hz}$ at 300 Myr to $\xi_{\text{ion}} = 10^{26.1} \text{ erg}^{-1} \text{ Hz}$ at 2 Myr. In this case, we would expect that the most extreme Ly α emitters stand out as the sources dominated by the youngest stellar populations.

We investigate these possibilities in the 61 galaxies in our sample with NIRC*am*-based SEDs (which constrain age) and grism-based H α measurements (which constrain the Ly α escape fraction). To illustrate the trends, we first show four representative sources spanning the full range in Ly α EW, from 23 \AA to 533 \AA (see Fig. 2). It is immediately apparent that the inferred age does not vary with the Ly α EW. In all four galaxies, we see young ages (≈ 10 Myr) linked with efficient ionizing production. In contrast, the Ly α escape

⁵ <https://www.astro.uu.se/valdwiki/Air-to-vacuum%20conversion>

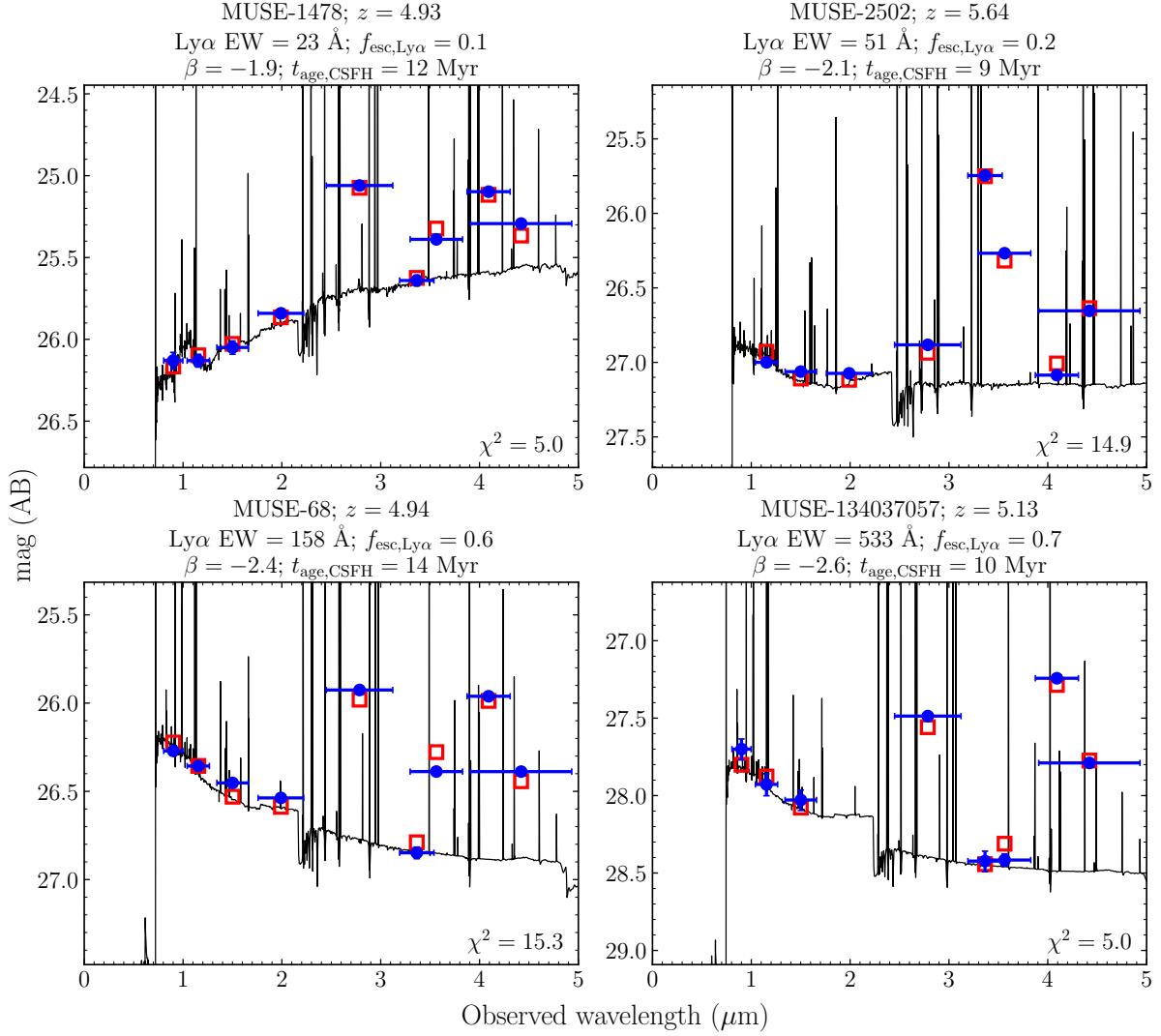


Figure 2. JADES SEDs of example galaxies in the four Ly α EW bins (top two panels: Ly α EW $\simeq 20 \text{ \AA}$, 50 \AA ; bottom two panels: 150 \AA , and 500 \AA). Observed *JWST*/NIRCam photometry is shown by blue circles. The spectra (black lines) and synthetic photometry (red squares) are derived from the posterior median of BEAGLE models. All the SEDs show large flux excesses with respect to the continuum in some of the NIRCam long wavelength filters (F277W, F335M, F356W, F410M, F444W), indicating intense rest-frame optical line emission (e.g., [O III]+H β , H α +[N III]) often associated with very young stellar populations (CSFH age $\simeq 10$ Myr). All these four galaxies present very efficient ionizing (and hence Ly α) photon production inferred from BEAGLE ($\xi_{\text{ion}} \gtrsim 10^{25.6} \text{ erg}^{-1} \text{ Hz}$), while the Ly α escape fraction varies with Ly α EW, with $f_{\text{esc,Ly}\alpha} = 0.1$ seen in the Ly α EW $\simeq 20 \text{ \AA}$ system to $f_{\text{esc,Ly}\alpha} = 0.7$ at Ly α EW $\simeq 500 \text{ \AA}$.

fraction shows a clear trend, increasing from relatively modest transmission ($f_{\text{esc,Ly}\alpha} = 0.1 - 0.2$) in the two moderate-EW Ly α emitters to near-unity ($f_{\text{esc,Ly}\alpha} = 0.6 - 0.7$) in the two most extreme line emitters (EW = $150 - 500 \text{ \AA}$). For these four galaxies, variations in line transmission (and not production efficiency) are what separates galaxies with moderate and extreme Ly α emission.

The full Ly α selected sample with H α detections shows a similar picture. We find a positive correlation between the Ly α EW and the Ly α escape fraction (top right panel of Fig. 3), with Ly α emitters with EW = 20 \AA generally showing $f_{\text{esc,Ly}\alpha} = 0.1$, and those with EW $\simeq 100 - 500 \text{ \AA}$ having $f_{\text{esc,Ly}\alpha} = 0.6$. This trend is qualitatively consistent with relations found in other samples at a variety of redshifts (e.g., Yang et al. 2017; Jaskot et al. 2019; Izotov et al. 2024; Saxena et al. 2024) and indicates that the transmission of Ly α is likely playing a dominant role in regulating the Ly α EW. In Fig. 3, we show how galaxy properties vary with Ly α EW. In the top left

panel, we see the derived ionizing photon production efficiency as a function of Ly α EW, with the results showing extremely young galaxies ($\lesssim 20$ Myr) with Ly α EW spanning the full range in our sample ($20 - 500 \text{ \AA}$). Saxena et al. (2024) also shows $z \gtrsim 6$ galaxies with large ionizing photon production efficiencies (often associated with very young ages) spanning a wide range of Ly α EW ($\simeq 20 - 300 \text{ \AA}$). While young galaxies will have enhanced Ly α production, this does not guarantee they will be observed with the largest Ly α EWs.

Our $z \simeq 5 - 6$ sample includes 23 galaxies with extremely large Ly α escape fractions ($f_{\text{esc,Ly}\alpha} > 0.5$). These systems appear to have blue UV slopes ($\beta < -2.1$), with a median $\beta = -2.4$ and the bluest UV slope down to $\beta = -2.8$ (bottom left panel of Fig. 3). Since UV slope is a tracer of dust attenuation (e.g., Calzetti et al. 1994; Meurer et al. 1999), the above finding indicates that Ly α emitters in our sample with enhanced Ly α transmission are likely associated with low dust content (e.g., Verhamme et al. 2008; Hayes et al. 2011;

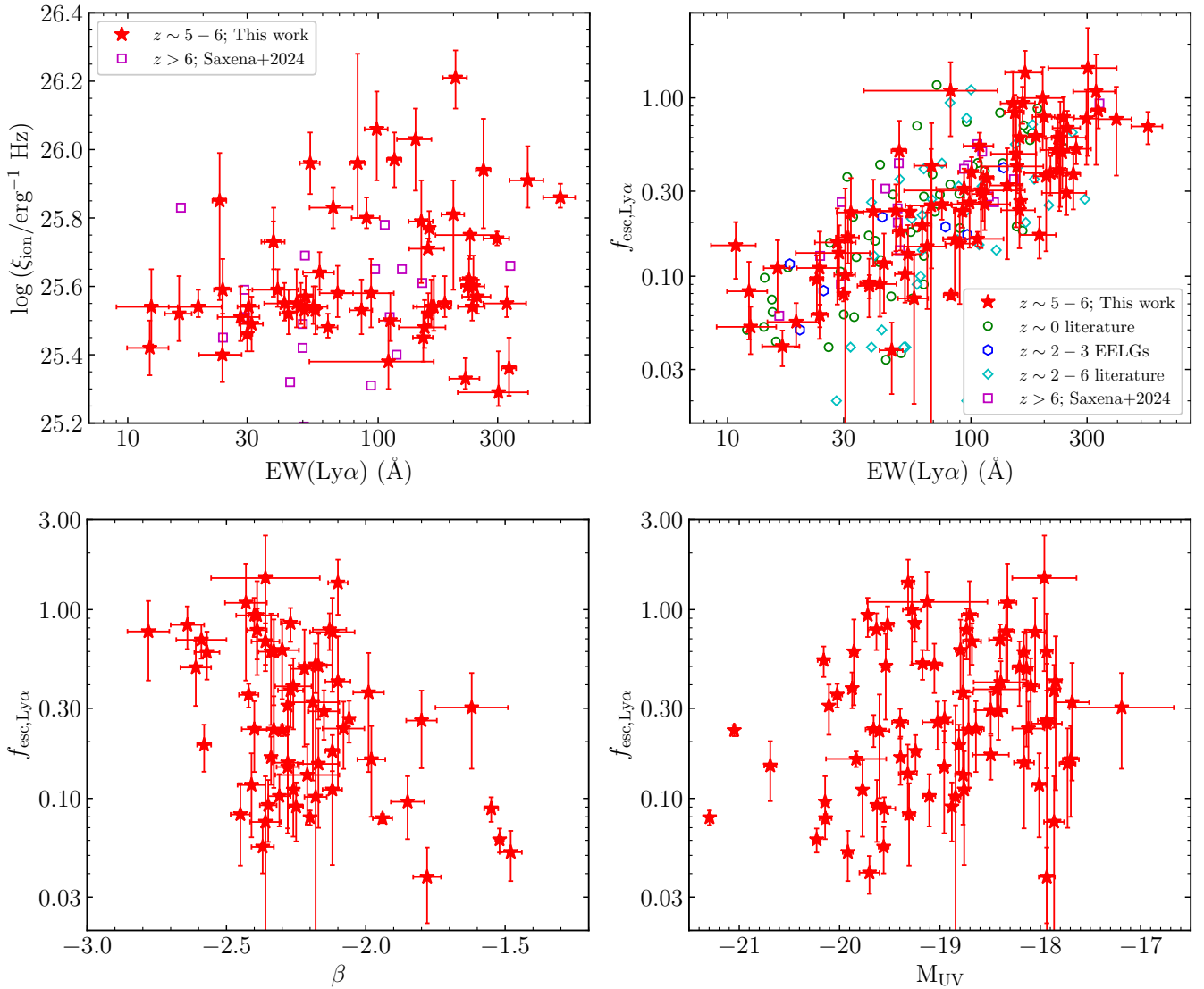


Figure 3. Top left panel: ionizing photon production efficiency (ξ_{ion}) inferred from BEAGLE models versus $\text{Ly}\alpha$ EW for the 61 $\text{Ly}\alpha$ emitters with $\text{H}\alpha$ detections and JADES NIRCcam SEDs at $4.9 < z < 6.5$ (red stars). We find galaxies that are efficient in producing ionizing photons ($\xi_{\text{ion}} > 10^{25.6} \text{ erg}^{-1} \text{ Hz}$, hence with very large intrinsic $\text{Ly}\alpha$ EWs $> 300 \text{ \AA}$) span a wide range of observed $\text{Ly}\alpha$ EW from $\approx 20 \text{ \AA}$ to 400 \AA . Top right panel: $\text{Ly}\alpha$ escape fraction (assuming case B recombination) as a function of $\text{Ly}\alpha$ EW for the 79 $\text{Ly}\alpha$ emitters in our sample (red stars). We find a tight correlation between $\text{Ly}\alpha$ EW and $\text{Ly}\alpha$ escape fraction. As a comparison, we overplot $z \approx 0$ Green peas (Yang et al. 2017; Jaskot et al. 2019) or metal-poor star-forming galaxies (Izotov et al. 2024) (open green circles), extreme emission line galaxies (EELGs) at $z \sim 2-3$ (open blue hexagons; Tang et al. 2021, 2024), $\text{Ly}\alpha$ emitters at $z \sim 2-6$ (open cyan diamonds; Matthee et al. 2021; Roy et al. 2023), and $\text{Ly}\alpha$ emitters at $z \geq 6$ (open magenta squares; Saxena et al. 2024). Bottom left and right panels: $\text{Ly}\alpha$ escape fraction versus UV slope and M_{UV} for the 79 $\text{Ly}\alpha$ emitters in our sample. Galaxies with larger $\text{Ly}\alpha$ escape fractions tend to be bluer systems.

Matthee et al. 2016; Lin et al. 2024). The UV slope is also impacted by a variety of other properties (i.e., age, metallicity, ionizing photon escape), so it is possible that the blue colors are additionally driven by these factors (Bouwens et al. 2010a; Chisholm et al. 2022; Topping et al. 2022, 2024). We may also expect galaxies with large $\text{Ly}\alpha$ escape fractions to be fainter systems with very young stellar ages (e.g., $\lesssim 10$ Myr). This is because large gaseous disks may have not yet developed in faint galaxies (e.g., Erb et al. 2014) and the strong feedback associated with intense bursts can clear the pathway (e.g., Kimm et al. 2019; Ma et al. 2020; Kakiichi & Gronke 2021), both are conducive to the leakage of $\text{Ly}\alpha$ photons. While we do see that some of the galaxies with $f_{\text{esc,Ly}\alpha} > 0.5$ in our $\text{Ly}\alpha$ selected sample

are faint ($M_{\text{UV}} = -18$) with young CSFH ages (2–10 Myr), we also find $f_{\text{esc,Ly}\alpha} > 0.5$ among relatively bright ($M_{\text{UV}} = -20$) systems (bottom right panel of Fig. 3) and galaxies with more evolved stellar populations (CSFH age ≈ 100 Myr). We will discuss the dependence of $\text{Ly}\alpha$ transmission on galaxy properties for the entire Lyman break selected sample in Section 4 to explore whether very large $\text{Ly}\alpha$ escape fractions ($f_{\text{esc,Ly}\alpha} > 0.5$) are more frequent in a subset of systems (e.g., with bluer UV slopes, fainter M_{UV} , or younger CSFH ages).

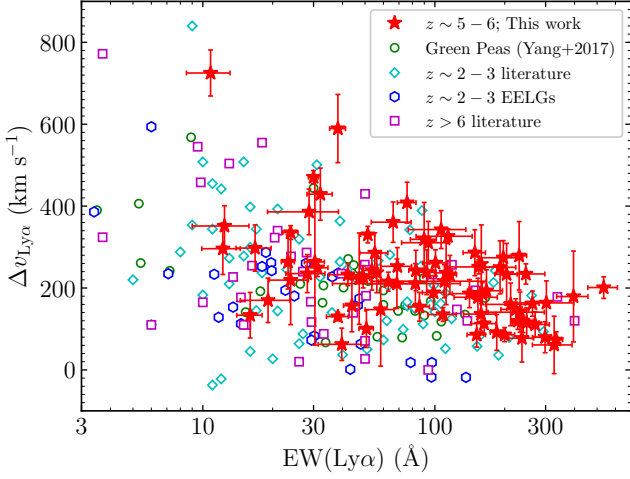


Figure 4. Ly α velocity offset versus Ly α EW for the 79 Ly α emitters with H α detections at $4.9 < z < 6.5$ (red stars). While our strong Ly α emitters at $4.9 < z < 6.5$ tend to have lower Ly α velocity offsets comparing to those with lower Ly α EWs, there are EW > 100 Å Ly α emitters presenting relatively large Ly α velocity offsets (≥ 200 km s $^{-1}$) indicating dense neutral hydrogen along the sightlines. For comparison, we overplot literature data at lower and higher redshifts including Green Peas (open green circles; Yang et al. 2017), Ly α emitters at $z \approx 2-3$ (open cyan diamonds; Finkelstein et al. 2011; McLinden et al. 2011, 2014; Hashimoto et al. 2013; Erb et al. 2014; Matthee et al. 2021), EELGs at $z \approx 2-3$ (open blue hexagons; Tang et al. 2021, 2024), and $z > 6$ galaxies (open magenta squares; Maiolino et al. 2015; Stark et al. 2015, 2017; Willott et al. 2015; Inoue et al. 2016; Pentericci et al. 2016; Bradač et al. 2017; Laporte et al. 2017; Mainali et al. 2017; Hashimoto et al. 2019; Hutchison et al. 2019; Endsley et al. 2022; Bunker et al. 2023b; Tang et al. 2023; Saxena et al. 2024).

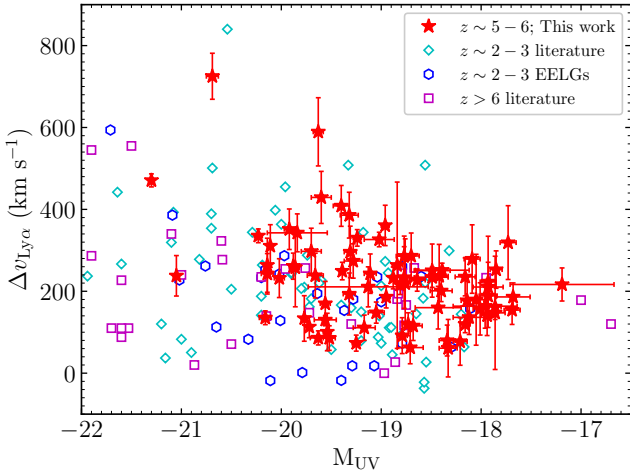


Figure 5. Ly α velocity offset versus absolute UV magnitude for the 79 Ly α emitters with H α detections at $4.9 < z < 6.5$ (red stars). We overplot literature data as a comparison, including Ly α emitters at $z \approx 2-3$ (open cyan diamonds; Erb et al. 2014; Matthee et al. 2021) and EELGs at $z \approx 2-3$ (open blue hexagons; Tang et al. 2021, 2024), as well as $z > 6$ galaxies (open magenta squares; Maiolino et al. 2015; Stark et al. 2015, 2017; Willott et al. 2015; Inoue et al. 2016; Pentericci et al. 2016; Bradač et al. 2017; Laporte et al. 2017; Mainali et al. 2017; Hashimoto et al. 2019; Hutchison et al. 2019; Endsley et al. 2022; Bunker et al. 2023b; Tang et al. 2023; Saxena et al. 2024).

3.2 Ly α peak velocity offsets of LAEs at $z \approx 5 - 6$

The Ly α velocity profile provides insight to the escape of Ly α through the ISM and CGM (e.g., Dijkstra 2017; Blaizot et al. 2023; Almada Monter & Gronke 2024). Trends between the Ly α velocity offset and galaxy properties have been established in Ly α emitter samples at $z \approx 0.3 - 2$ (e.g., Erb et al. 2014; Hashimoto et al. 2015; Yang et al. 2017; Tang et al. 2024). Galaxies with the largest EW Ly α emission at these redshifts are generally found with the smallest Ly α velocity offsets (e.g., Erb et al. 2014; Tang et al. 2021, 2024), likely reflecting lower H I column densities which in turn allow Ly α to escape without significant diffusion to large velocities (e.g., Verhamme et al. 2006, 2015). When Ly α is seen to emerge near the line center ($\lesssim 100$ km s $^{-1}$), it may point to situations where Ly α emerges through low density channels that are optically thin to Lyman continuum (LyC) emission (e.g., Behrens et al. 2014; Verhamme et al. 2015; Dijkstra et al. 2016; Naidu et al. 2017; Rivera-Thorsen et al. 2017; Izotov et al. 2021; Choustikov et al. 2024a). Prior to the launch of *JWST*, Ly α velocity profiles at $z \gtrsim 5$ could only be constrained in a few sources with systemic redshifts measured from non-resonant UV lines (i.e., C III) or far-infrared lines ([C II] 158 μ m) (e.g., Stark et al. 2017; Cassata et al. 2020; Matthee et al. 2020; Endsley et al. 2022). As such samples are small, it has long been unclear how common low velocity offsets are in $z \approx 5 - 6$ galaxies.

We explore the velocity profiles at $z \approx 5 - 6$ using the 79 galaxies in our sample with Ly α and H α measurements. As expected, the velocity offset decreases with increasing Ly α EW (Fig. 4). In the weakest Ly α emitters in our sample (EW = 10 – 30 Å), we find large velocity offsets (median $\Delta v_{\text{Ly}\alpha} = 300$ km s $^{-1}$). These decrease to a median $\Delta v_{\text{Ly}\alpha} = 180$ km s $^{-1}$ in the strongest Ly α emitters (EW > 100 Å). Notably absent in our $z \approx 5 - 6$ sample are galaxies with very low Ly α velocity offsets. Among the 39 strongest Ly α emitters (EW > 100 Å) in our sample, only 7 galaxies present low Ly α velocity offsets with $\Delta v_{\text{Ly}\alpha} < 100$ km s $^{-1}$ and none of them shows $\Delta v_{\text{Ly}\alpha} < 50$ km s $^{-1}$. On the contrary, the strongest Ly α emitters (EW $\gtrsim 100$ Å) at $z \approx 2 - 3$ occasionally show Ly α peaks closer to the line center ($\Delta v_{\text{Ly}\alpha} < 100$ km s $^{-1}$; e.g., Erb et al. 2014; Rivera-Thorsen et al. 2017; Matthee et al. 2021; Tang et al. 2024). Among galaxies with large [O III]+H β EWs (> 600 Å), existing data suggests the median Ly α peak velocity offset of large EW Ly α emitters at $z \approx 2 - 3$ is 20 km s $^{-1}$ Tang et al. (2024), considerably lower than that of strong Ly α emitters at $z \approx 5 - 6$ ($\Delta v_{\text{Ly}\alpha} = 180$ km s $^{-1}$) with the same [O III]+H β EWs. This may indicate significant evolution in Ly α peak velocities at $2 < z < 6$, with the small offset sources linked to LyC leakage (though with scatter; Pahl et al. 2024) disappearing as we enter the reionization era.

Previous work has demonstrated that Ly α velocity offsets are often largest in the most massive galaxies (e.g., Erb et al. 2014; Shibuya et al. 2014; Stark et al. 2017; Mason et al. 2018a; Endsley et al. 2022), likely reflecting larger reservoirs of neutral gas through which Ly α photons must escape. This trend is also seen when looking at absolute UV magnitude. Luminous galaxies have been found with very large velocity offsets ($\Delta v_{\text{Ly}\alpha} = 300 - 800$ km s $^{-1}$) at lower redshifts ($z \approx 2 - 3$; e.g., Erb et al. 2014) and at $z > 6$ (e.g., Endsley et al. 2022; Bunker et al. 2023b; Tang et al. 2023). In Fig. 5, we plot the Ly α velocity offset versus absolute UV magnitude for both our Ly α selected sample at $4.9 < z < 6.5$ and Ly α emitters over different redshifts from literature. While luminous galaxies ($M_{\text{UV}} < -20.5$) are few (three galaxies) in our sample, they appear to show the largest velocity offsets (median $\Delta v_{\text{Ly}\alpha} = 470$ km s $^{-1}$). On the other hand, the less luminous systems ($M_{\text{UV}} = -20$ to -18) have lower Ly α velocity offsets with a median value of $\Delta v_{\text{Ly}\alpha} = 220$ km s $^{-1}$, consistent with

the $\Delta v_{\text{Ly}\alpha} - M_{\text{UV}}$ trend seen in literature (e.g., Prieto-Lyon et al. 2023). Based on this $z \approx 5 - 6$ baseline sample, we may expect luminous galaxies to be easier to detect in Ly α at $z \geq 7$ as the large velocity Ly α emission faces less attenuation from the neutral IGM (e.g., Stark et al. 2017; Mason et al. 2018b; Hashimoto et al. 2019; Endsley et al. 2022).

To better demonstrate the shift in Ly α velocity profiles over $2 \lesssim z \lesssim 6$, we create a composite Ly α spectrum of our $z \approx 5 - 6$ galaxies. We stack the individual spectra following the procedures described in Tang et al. (2024) which we summarize below. Our goal is to identify the velocity profile associated with the strongest Ly α emitters, so we create a composite for those systems in our sample with Ly α EW $> 40 \text{ \AA}$. To create the composite spectrum, we shift individual spectra (after converting air wavelengths to vacuum) to the rest-frame using the systemic redshifts inferred from H α or [O III] $\lambda 5007$ lines. Then we interpolate each spectrum to a common wavelength scale with a bin size of 0.2 \AA in rest-frame, which is larger than the wavelength bin size of each individual spectrum. We next normalize each individual spectrum using its measured Ly α flux. The individual spectra are stacked by median-combining the individual flux densities in each wavelength bin. Finally, we convert the rest-frame wavelengths to the velocity space ($\Delta v = c(\lambda_{\text{rest}} - \lambda_{\text{Ly}\alpha})/\lambda_{\text{Ly}\alpha}$, where c is the speed of light and $\lambda_{\text{Ly}\alpha} = 1215.67 \text{ \AA}$) to illustrate the velocity profile of Ly α emission line. We compare this to line profiles of $z \approx 2 - 3$ galaxies matched in [O III]+H β EW and described in (Tang et al. 2024). That paper presents resolved ($R \sim 3900$) Ly α spectroscopy of $z \approx 2 - 3$ galaxies with [O III]+H β EW $> 600 \text{ \AA}$ using Binospec (Fabricant et al. 2019) on the MMT. For details, the reader is directed to Tang et al. (2024).

The composite Ly α profile of our $z \approx 5 - 6$ Ly α emitters is shown in the top panel of Fig. 6 as the black solid line. We see its Ly α peak at a relatively large velocity offset ($\Delta v_{\text{Ly}\alpha} = 230 \text{ km s}^{-1}$), similar to that of many of the individual spectra shown in Fig. 4. We find only a small portion of emission at the line center – the fraction of Ly α flux emitted within $\pm 100 \text{ km s}^{-1}$ of the systemic redshift (the so-called ‘‘Ly α central escape fraction’’; e.g., Naidu et al. 2022) is 9 per cent. The result suggests that the strongest Ly α emitters (EW $> 40 \text{ \AA}$) at $z \approx 5 - 6$ may be uniformly covered by dense neutral hydrogen ($N_{\text{HI}} \approx 10^{19} - 10^{20} \text{ cm}^{-2}$ assuming an expanding shell model, e.g., Hashimoto et al. 2015; Verhamme et al. 2015, or equivalently the total H I column density $\approx 10^{19} - 10^{20} \text{ cm}^{-2}$ assuming a clumpy slab model, e.g., Li & Gronke 2022). Such H I column densities are optically thick to LyC emission (e.g., Verhamme et al. 2015), indicating that strong Ly α emitters at $z > 5$ may have neutral gas distributions that do not facilitate large LyC escape fractions. This is significantly different from lower redshifts where strong Ly α emitters are closely linked to LyC leakage (e.g., Steidel et al. 2018; Fletcher et al. 2019; Flury et al. 2022; Naidu et al. 2022; Pahl et al. 2023) and have Ly α profiles that reveal low H I column densities (e.g., Erb et al. 2014; Rivera-Thorsen et al. 2017; Vanzella et al. 2018; Jaskot et al. 2019; Izotov et al. 2021; Matthee et al. 2021). This is clearly seen in the bottom panel of Fig. 6, where the composite shows strong Ly α peaking near the line center, with half of the flux emitted within $\pm 100 \text{ km s}^{-1}$ of the systemic redshift (Tang et al. 2024).

Naively we may interpret the disappearance of strong Ly α emitters with small peak velocity offsets ($< 100 \text{ km s}^{-1}$) and large Ly α central escape fractions (≥ 20 per cent) as evidence that large LyC escape fractions ($f_{\text{esc,LyC}} \geq 0.2$; e.g., Naidu et al. 2022; Choustikov et al. 2024a) are becoming less common as we enter the reionization era. But more likely we are seeing the imprint of the IGM on Ly α profiles at $z \approx 5 - 6$. Even if the IGM is mostly ionized at these redshifts, the IGM density is high enough for the residual neutral hydrogen

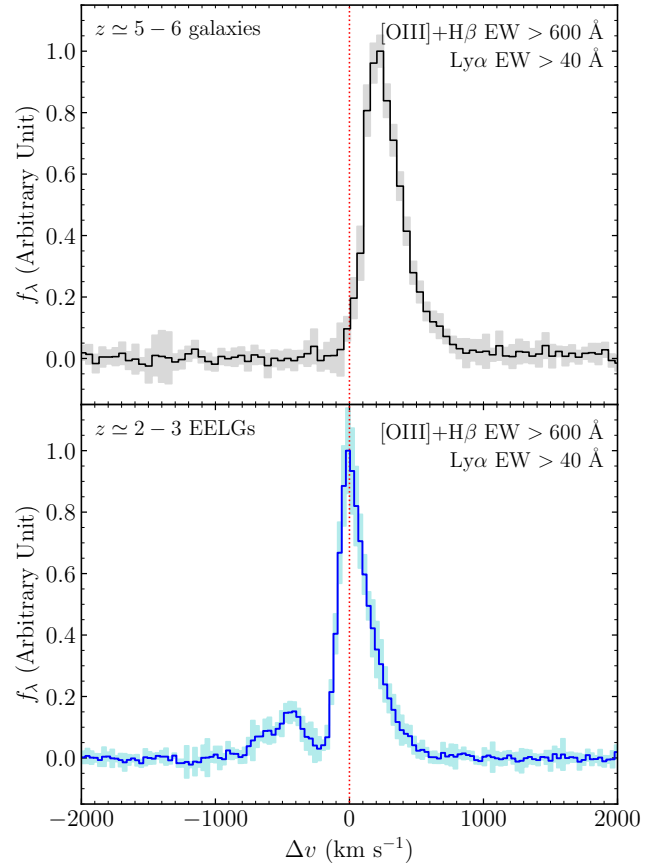


Figure 6. Comparison of composite Ly α profile between $z \approx 5 - 6$ galaxies (top panel, black line) and $z \approx 2 - 3$ galaxies (bottom panel, blue line; Tang et al. 2024). The 1σ variations are shown as the shaded regions. We compare galaxies selected with the same criteria ([O III]+H β EW $> 600 \text{ \AA}$ and Ly α EW $> 40 \text{ \AA}$; Tang et al. 2024) in both samples. The red dotted line shows $\Delta v_{\text{Ly}\alpha} = 0 \text{ km s}^{-1}$ derived using the systemic redshifts inferred from H α or [O III] $\lambda 5007$ lines. While the composite Ly α profile at $z \approx 2 - 3$ presents a significant fraction of Ly α flux emitted at the line center (~ 50 per cent) and a blue peak, the bulk of the Ly α flux of $z \approx 5 - 6$ galaxies is shifted to redder wavelengths with a peak at $\Delta v_{\text{Ly}\alpha} \approx 230 \text{ km s}^{-1}$.

($x_{\text{HI}} \geq 10^{-5} - 10^{-4}$; e.g., Yang et al. 2020b; Bosman et al. 2022) to efficiently scatter Ly α photons near the line center. The transmission (\mathcal{T}) at $\Delta v_{\text{Ly}\alpha} = 0 \text{ km s}^{-1}$ is expected to be negligible ($\mathcal{T} \approx 0.16$ at $z \sim 5$ and $\mathcal{T} \approx 0.01$ at $z \sim 6$; e.g., Inoue et al. 2014; Becker et al. 2015; Bosman et al. 2018; Eilers et al. 2018; Yang et al. 2020b; Bosman et al. 2022), effectively attenuating any Ly α peaking near systemic. If the IGM is infalling onto galaxies, there is likely further scattering of Ly α photons within $\sim 100 \text{ km s}^{-1}$ on the red side of the line center (e.g., Santos 2004; Dijkstra et al. 2007; Laursen et al. 2011; Mason et al. 2018a). We note that if $z > 5$ galaxies occasionally reside in underdense regions or quasar proximity zones the transmission near the line center may be boosted (e.g., Bosman et al. 2020; Mason & Gronke 2020). But in general the IGM effects will make it difficult at $z \approx 5 - 6$ to recover Ly α emission with velocity profiles linked to LyC leakage (i.e., those with small velocity offsets).

At lower redshifts, Ly α emission provides one of the best indicators of LyC emission. While it has always been clear that the IGM damping wing will make the connection between Ly α and LyC emission less useful at $z \geq 7$, the results presented in this paper suggest

that the utility of Ly α as a probe of ionizing photon leakage is likely to also be limited at $z \approx 5 - 6$. If galaxies at these redshifts with the largest escape fractions have ionized channels that facilitate direct escape of Ly α at the line center (or at small positive velocity offsets), the IGM will strongly scatter their Ly α emission, making them unlikely to enter Ly α emitter samples. They will be identifiable in continuum-selected samples, likely with properties similar to those of leakers at lower redshifts (e.g., blue UV colors, low masses; e.g., Chisholm et al. 2022; Flury et al. 2022; Kim et al. 2023; Pahl et al. 2023). But because their Ly α is heavily attenuated by the IGM, we will need to rely on other techniques to more clearly reveal this population as strong LyC leakers. Efforts to detect Mg II emission (e.g., Henry et al. 2018; Chisholm et al. 2020; Xu et al. 2022, 2023) and low ionization absorption lines (e.g., Heckman et al. 2001; Shapley et al. 2003; Erb 2015; Reddy et al. 2016; Chisholm et al. 2018; Steidel et al. 2018; Saldana-Lopez et al. 2022) are challenging, but they provide the best path to selecting galaxies with conditions that are conducive to escape of ionizing radiation. UV slopes provide another promising indicator (e.g., Bouwens et al. 2010a; Ono et al. 2010; Raiter et al. 2010; Robertson et al. 2010; Chisholm et al. 2022; Topping et al. 2022; Kim et al. 2023). Recent cosmological hydrodynamical simulation also suggests composite indicators for predicting LyC escape fraction (Choustikov et al. 2024b).

We next consider implications of the velocity offsets in the strong Ly α emitters at $z \approx 5 - 6$. The presence of prominent Ly α emission (EW > 100 Å) in galaxies with large velocity offsets (> 200 km s⁻¹) suggests there must be a population that is able to transmit a large fraction of Ly α emission through fairly large column densities of neutral hydrogen. We suggest this may be possible in cases where the dust content is low enough for scattered Ly α emission to emerge through H I without being absorbed (e.g., Stark et al. 2010; Hayes et al. 2011; Matthee et al. 2016). Given the low stellar masses (median $4 \times 10^7 M_{\odot}$) and very blue UV slopes (median $\beta = -2.3$) in the EW > 100 Å Ly α emitters, it seems plausible that we may be seeing such an effect in the $z \approx 5 - 6$ sample. This could be further amplified if the CGM is compact, allowing more of the Ly α to appear centrally concentrated and higher in surface brightness. Deep rest-frame UV spectroscopy have hinted that neutral gas may indeed be more compact at higher redshifts (Jones et al. 2012). There are examples of strong Ly α emitters with large velocity offsets at lower redshifts (e.g., XLS-6 and XLS-24 in Matthee et al. 2021), and indeed they tend to have very blue UV slopes ($\beta \lesssim -2.5$) suggesting minimal absorption of Ly α photons. Such galaxies should become more common at $z \approx 5 - 6$ as the population shifts toward lower mass galaxies with bluer UV slopes (e.g., Topping et al. 2024).

Finally we investigate the Ly α velocity offset distribution of strong Ly α emitters (EW > 50 Å) at $z \approx 5 - 6$. We fit the probability density function of the Ly α velocity offsets of the 57 Ly α emitters with EW > 50 Å in our sample with a truncated Gaussian distribution, which accounts for the disappearance of galaxies with very low Ly α velocity offsets ($\Delta v_{\text{Ly}\alpha} \lesssim 60 \text{ km s}^{-1}$) at $z \approx 5 - 6$:

$$\begin{aligned} p(\Delta v) &= A \cdot \exp[-(\Delta v - \mu)^2 / (2\sigma^2)] \quad (\text{when } \Delta v \geq \Delta v_{\text{cut}}) \\ p(\Delta v) &= 0 \quad (\text{when } \Delta v < \Delta v_{\text{cut}}). \end{aligned}$$

Where A , μ , and σ are the amplitude, mean, and standard deviation of the Gaussian distribution, and Δv_{cut} is the minimum Ly α velocity offset at $z \approx 5 - 6$. We fit the distribution using a Bayesian approach, considering uniform priors: $\mu = 50 - 500 \text{ km s}^{-1}$, $\sigma = 20 - 200 \text{ km s}^{-1}$, and $\Delta v_{\text{cut}} = 0 - 100 \text{ km s}^{-1}$. Then we derive the posterior probability distributions of the above four parameters using the EMCEE package (Foreman-Mackey et al. 2013). We find that the Ly α velocity offset distribution of strong Ly α emitters at $z \approx 5 - 6$ can be

described by a mean value of $\Delta v_{\text{Ly}\alpha} = 199 \text{ km s}^{-1}$, a standard deviation $\sigma = 82 \text{ km s}^{-1}$, and a minimum offset at $\Delta v_{\text{cut}} = 61 \text{ km s}^{-1}$. This demonstrates that only 33 per cent of the EW > 50 Å Ly α emitters at $z \approx 5 - 6$ show relatively small Ly α velocity offsets with $\Delta v_{\text{Ly}\alpha} = 60 - 150 \text{ km s}^{-1}$. The Ly α velocity offset distribution at $z \approx 5 - 6$ will be useful for predicting how frequently we might expect to find Ly α emitters with low velocity offsets in ionized bubbles at $z \gtrsim 7$. We note this distribution would likely be different in more luminous galaxies at this redshift (Endsley et al. 2022). We will discuss this in Section 5.

As a comparison with our $z \gtrsim 5$ measurements, we derive the Ly α velocity offset distribution of $z \approx 2$ Ly α emitters from Matthee et al. (2021) and Tang et al. (2024), requiring the same Ly α EWs (> 50 Å) and [O III]+H β EWs (> 600 Å) as our $z \approx 5 - 6$ sample. Following the approach described above, we find that the mean and standard deviation of the Ly α velocity offset distribution at $z \approx 2$ are 116 km s⁻¹ and 100 km s⁻¹, respectively. This indicates that 63 per cent of the EW > 50 Å Ly α emitters at $z \approx 2$ show small Ly α velocity offsets with $\Delta v_{\text{Ly}\alpha} < 150 \text{ km s}^{-1}$ and even 25 per cent show $\Delta v_{\text{Ly}\alpha}$ close to the systemic redshift (< 50 km s⁻¹). This distribution suggests the disappearance of galaxies with very small Ly α velocity offsets from $z \approx 2$ to $z \approx 5 - 6$, consistent with the trend shown in Fig. 4. Further data at $z \approx 2 - 3$ targeting extreme line emitters will be useful for better establishing the evolution in Ly α line profiles.

3.3 The strength of blue peaks in Ly α emission at $z \approx 5 - 6$

At lower redshifts ($z \lesssim 5$), Ly α profiles generally show a weak peak blueward of the systemic redshift (e.g., Jaskot & Oey 2014; Henry et al. 2015; Yang et al. 2017; Gazagnes et al. 2020; Izotov et al. 2020; Hayes et al. 2021; Matthee et al. 2021). Such blue peak Ly α emission usually originates from Ly α photons that have diffused through the near side of the outflowing gas (e.g., Verhamme et al. 2006, 2015; Gronke & Dijkstra 2016; Ouchi et al. 2020; Li & Gronke 2022). At $z > 5$, due to the high IGM density, the blue peak Ly α emission should be strongly attenuated by resonant scattering from residual neutral hydrogen even in regions that have been reionized (Gunn & Peterson 1965). However, potential blue peak detections have been presented in four galaxies at $z \gtrsim 6$ (Hu et al. 2016; Matthee et al. 2018; Songaila et al. 2018; Bosman et al. 2020; Meyer et al. 2021). This implies that these systems may be surrounded by intergalactic gas with a higher ionized hydrogen fraction than is typical, perhaps due to hard local radiation fields (e.g., Mason & Gronke 2020; Torralba-Torregrosa et al. 2024). Another potential explanation is that these galaxies have atypically strong blue Ly α emission due to inflowing gas (e.g., Trebitsch et al. 2016; Ao et al. 2020; Li et al. 2022). How commonly blue-sided Ly α emission appears at $z \approx 5 - 6$ (when the IGM is mostly ionized) is not yet known, making it challenging to physically interpret any detections that emerge at $z \gtrsim 6$.

We characterize blue peaks in the 79 Ly α emitters with H α -based systemic redshifts at $z \approx 5 - 6$. Here we aim to constrain the strength of Ly α emission on the blue side of the line center. To do this, we quantify the ratio of Ly α that is blueward of the systemic redshift to that redward (hereafter the blue-to-red flux ratio), by integrating the Ly α flux at velocities -1000 to 0 km s^{-1} of the Ly α resonance and at 0 to $+1000 \text{ km s}^{-1}$. The integration range is chosen to be similar with the literature (e.g., Matthee et al. 2018, 2021; Hayes et al. 2021).

Most of our galaxies (77 of 79) present a single Ly α peak with no emission blueward of systemic. We derive the upper limits of the blue-to-red Ly α flux ratio for these 77 single-peaked Ly α emitters, which are uniformly < 0.15 (5σ). As a comparison, we consider

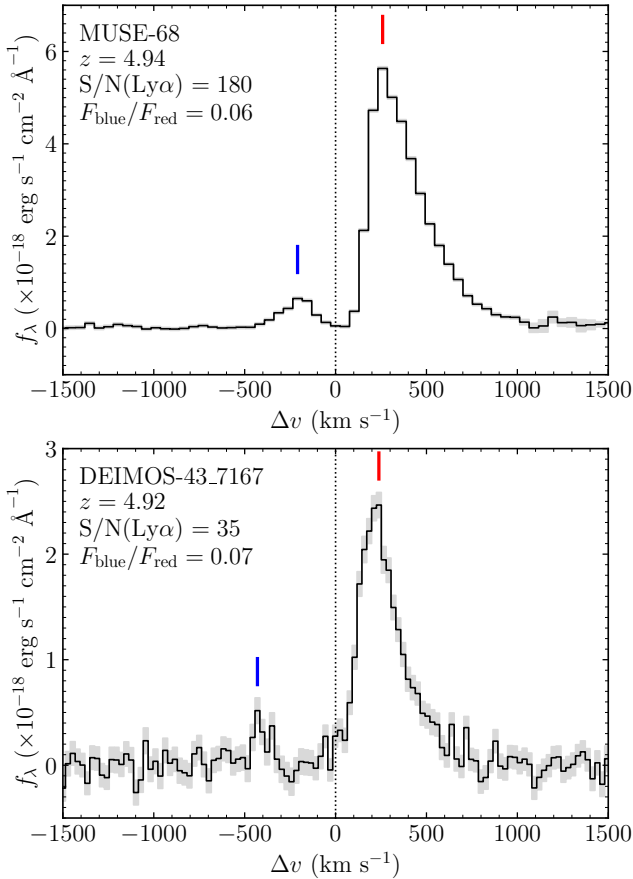


Figure 7. Ly α spectra of the two Ly α emitters with blue peaked Ly α emission in our $z \approx 5 - 6$ sample (top panel: MUSE-68; bottom panel: DEIMOS-43_7167). The spectra are shown in the velocity space using the systemic redshifts measured from H α emission lines. The error spectra are presented by grey shaded regions. The blue and red peaked Ly α emission are marked by the blue and red lines. These two galaxies are at the lowest redshift among our sample ($z \approx 4.9$) with the highest S/N Ly α detections (S/N = 180 and 35). The blue-to-red flux ratios of these two galaxies are 0.06 – 0.07.

the Ly α profiles of Ly α emitters at $z < 0.44$ (Hayes et al. 2021) and $z \sim 2$ (Matthee et al. 2021; Tang et al. 2024) where the IGM is mostly transparent to blueshifted Ly α photons. For those with similar Ly α EWs ($\approx 20 - 300 \text{ \AA}$ with a median EW $\approx 80 \text{ \AA}$) to our $z \approx 5 - 6$ sample, the blue peak Ly α emission at $z \approx 0 - 2$ is much more prominent, with an average blue-to-red flux ratio ≈ 0.3 . This suggests that the galaxies showing strong blue peak Ly α emission at low redshift ($z \approx 0 - 2$) disappear at the tail of reionization ($z \approx 5 - 6$), as would be expected from the increasing IGM opacity at earlier times (e.g., Madau 1995; Inoue et al. 2014; Eilers et al. 2018; Yang et al. 2020b).

To further illustrate the evolution of blue-sided Ly α emission, we generate a composite Ly α spectrum for all the 79 Ly α emitters with H α detections in our sample, following the same procedures described in Section 3.2. In the composite, we still do not detect any emission line feature blueward the systemic redshift, with an implied blue-to-red flux ratio < 0.04 (5σ). Comparing with the average Ly α profiles at $z \approx 0 - 2$ (Hayes et al. 2021; Matthee et al. 2021; Tang et al. 2024) with matched Ly α EWs, the average blue-to-red flux ratio of our $z \approx 5 - 6$ sample is less than 13 per cent of that at $z \approx 0 - 2$

(≈ 0.3). This is consistent with the decline of the IGM transmission at the Ly α resonance with redshift, from $\mathcal{T} = 0.9 - 1$ at $z \approx 0 - 2$ to just $\mathcal{T} = 0.16$ ($z = 5$) and $\mathcal{T} = 0.01$ ($z = 6$) assuming the Inoue et al. (2014) IGM transmission model. Given the typically low S/N with which blue peaks are detected at $z \approx 2 - 3$, it is not surprising that we do not see them at $z \approx 5 - 6$ if the IGM is only transmitting at most 10 per cent of the line emission.

While most of our Ly α emitters show a single, redshifted Ly α peak, we do identify two $z \gtrsim 5$ double-peaked Ly α emitting galaxies (MUSE-68 and DEIMOS-43_7167) with a peak blueward of the line center (Fig. 7). These two systems are at the lowest redshift ($z = 4.9$) in our sample, where the IGM opacity is likely the lowest. This increases the transmission of blue peak Ly α line relative to other sources in our sample, making blue peaks easier to detect. The blue peaks in both galaxies are much weaker than the red peaks, with blue-to-red flux ratios of 0.06 (MUSE-68; top panel of Fig. 7) and 0.07 (DEIMOS-43_7167; bottom panel of Fig. 7). Given typical transmission factors at $z = 4.9$ ($\mathcal{T} = 0.16$; Inoue et al. 2014), we would expect intrinsic blue-to-red flux ratios of ≈ 0.4 for the two sources. These intrinsic values are consistent with average ratios at $z \approx 0 - 2$, suggesting that these sources are not atypical in their blue peak flux fractions. The two galaxies with blue peaks also have the largest S/N among Ly α detections in our sample, with S/N(Ly α) = 180 for MUSE-68 (whose Ly α spectrum is obtained from the deepest MUSE field used in this work, MXDF) and S/N(Ly α) = 35 for DEIMOS-43_7167. In contrast, most of the other sources in our sample have S/N(Ly α) < 25 . The visibility of blue Ly α peaks of these two sources may primarily reflect their low redshifts (maximizing IGM transmission) and the S/N of the spectra. Finally we note that the two galaxies with blue peaks in our sample have $5 - 10\times$ lower blue-to-red flux ratios than those presented in the literature at $z \gtrsim 6$ ($= 0.3 - 0.7$; Hu et al. 2016; Matthee et al. 2018; Songaila et al. 2018; Bosman et al. 2020; Meyer et al. 2021). The four galaxies with blue peak Ly α detections in the literature at $z \gtrsim 6$ are relatively brighter with $M_{UV} < -21$. The absence of very prominent blue peaks in our sample suggests that these very large blue-to-red flux ratios must be relatively rare in the faint $z \approx 5 - 6$ galaxies which dominate our sample. It is conceivable they become more common in more luminous galaxies where our statistics are currently limited.

4 Ly α PROPERTIES IN LYMAN BREAK GALAXIES

In Section 3, we have demonstrated that galaxies with large EW ($> 100 \text{ \AA}$) Ly α emission and high Ly α transmission ($f_{\text{esc,Ly}\alpha} > 0.5$) are common among the Ly α selected sample at $z \approx 5 - 6$. We showed the strongest Ly α emitters tend to have relatively large velocity offsets, reflecting significant column densities of H I. In this section, we seek to explore how frequently the typical, Lyman break galaxies (LBGs) at $z \sim 5 - 6$ present large Ly α EWs and transmission by establishing the Ly α EW and Ly α escape fraction distributions. We present the selection of $z \sim 5 - 6$ galaxies using Lyman-break techniques in Section 4.1. Then we describe the methodology of constructing Ly α EW and escape fraction distributions in Section 4.2. Finally, we present the distributions of Ly α properties of our LBGs at $z \sim 5 - 6$ in Section 4.3.

4.1 Identification of Lyman break galaxies at $z \sim 5 - 6$

To establish the Ly α EW and Ly α escape fraction distributions at $z \sim 5 - 6$, we need to identify a sample of typical $z \sim 5 - 6$ galaxies. We now select star-forming galaxies at $z \sim 5 - 6$ via the standard

Lyman-break techniques, using the JADES *JWST*/NIRCam imaging (see Section 2.3) and the complementary *HST* Advanced Camera for Surveys (ACS) imaging from the HLF archive. Here we focus on the GOODS-South field overlapped with JADES observations as well as the MUSE-Wide and the MUSE-Deep observations. Using MUSE exposure maps (Bacon et al. 2017, 2023; Urrutia et al. 2019), we only consider the regions that have exposure time > 80 per cent of the designed exposure time of each MUSE observation (1 hour for MUSE-Wide, 10 hours for MOSAIC, 31 hours for UDF-10, and 141 hours for MXDF) and are overlapped with JADES observations. This allows us to derive robust Ly α properties (including both detections and upper limits) for all the LBGs covered by the MUSE field of view. We do not apply this study to the GOODS-North field because our Keck/DEIMOS observations only target a portion of LBGs within the DEIMOS field of view.

The Lyman-break galaxies at $z \sim 5$ ($4.5 \lesssim z \lesssim 5.5$) and $z \sim 6$ ($5.5 \lesssim z \lesssim 6.5$) were identified separately, using the rest-frame UV color computed from JADES CIRC1 aperture (0.2 arcsec diameter aperture) fluxes (see descriptions in Section 2.3). At $z \sim 5$, the Lyman break is located at $\approx 0.73 \mu\text{m}$, thus LBGs at this redshift range should appear as strong *HST* ACS/F606W dropouts. We select $z \sim 5$ star-forming galaxies using the similar criteria utilized in Bouwens et al. (2021):

$$\begin{aligned} \text{F606W} - \text{F814W} &> 1.2 \\ \text{F090W} - \text{F150W} &< 0.9 \\ \text{F606W} - \text{F814W} &> 1.2 \times (\text{F090W} - \text{F150W}) + 1.3. \end{aligned}$$

For objects with the $S/N < 1$ in F606W, we set the F606W flux to its 1σ upper limit. In addition, we require a non-detection ($S/N < 2$) in ACS/F435W.

We next select galaxies at $z \sim 6$ using the F775W dropout criteria utilized in Endsley et al. (2023a), which build on the approach of previous studies (e.g., Bunker et al. 2004; Bouwens et al. 2015):

$$\begin{aligned} \text{F775W} - \text{F090W} &> 1.2 \\ \text{F090W} - \text{F150W} &< 1.0 \\ \text{F775W} - \text{F090W} &> \text{F090W} - \text{F150W} + 1.2. \end{aligned}$$

Again, we set the F775W flux to its 1σ upper limit if its $S/N < 1$. We also require a non-detection in F435W with $S/N < 2$, and a strong dropout in F606W: $\text{F606W} - \text{F090W} > 2.7$, or $\text{F606W} - \text{F090W} > 1.8$ if $S/N(\text{F606W}) < 2$, where the F606W flux is set to its 1σ upper limit if $S/N(\text{F606W}) < 1$. If the F775W dropout is extremely strong ($\text{F775W} - \text{F090W} > 2.5$), we will ignore the F435W non-detection and the F606W dropout criteria.

To ensure robust dropout detection, we put a magnitude limit to the filter at rest-frame UV. This is because when the rest-frame UV band (i.e., F814W at $z \sim 5$, or F090W at $z \sim 6$) is very faint, we are not likely measure the Lyman break given the 1σ upper limit in the dropout band (i.e., F606W at $z \sim 5$, or F775W at $z \sim 6$). In HUDF, the typical 1σ depth of F606W (F775W) is 30.2 AB mag (e.g., Bouwens et al. 2015). To ensure we are able to measure the Lyman break with $\text{F606W} - \text{F775W} > 1.2$ at $z \sim 5$ ($\text{F775W} - \text{F090W} > 1.2$ at $z \sim 6$), we require the galaxies in our $z \sim 5$ ($z \sim 6$) sample in HUDF to present $\text{F814W} < 29$ ($\text{F090W} < 29$). In the other regions in GOODS-South, the typical 1σ depth of F606W (F775W) is 29.7 AB mag (29.2). Therefore, we require our $z \sim 5$ ($z \sim 6$) galaxies in those regions to present $\text{F814W} < 28.5$ ($\text{F090W} < 28$). Finally, to ensure the selected sources are real, we also require $S/N > 5$ in at least one NIRCam filter and $S/N > 3$ in at least three NIRCam filters for all the galaxies in our $z \sim 5$ and $z \sim 6$ LBG samples (Endsley et al. 2023a).

Because we aim to derive Ly α property distributions for LBGs at

$z \sim 5 - 6$, we must consider the potential bias of LBG selection to Ly α emitting galaxies. The presence of strong Ly α emission at the lower bound of redshift range probed by each dropout selection (e.g., $z \approx 4.5$ for F606W dropouts, or $z \approx 5.5$ for F775W dropouts) may boost the dropout filter and thus dilute the Lyman break color (e.g., Stanway et al. 2008). We cross-match the MUSE Ly α emitting galaxy catalog to our F606W and F775W dropout sample, and we find that several strong Ly α emitters (Ly α EW $\gtrsim 50 \text{ \AA}$) at $4.5 < z < 4.8$ are missed in the F606W dropout selection. While there are also strong Ly α emitters at $5.5 < z < 5.8$ missed in the F775W dropout selection, they are selected as F606W dropouts because the presence of strong Ly α boosts the F814W flux and hence these systems are still included in our total $z \sim 5 - 6$ LBG sample. Similarly, strong Ly α emission at $4.5 < z < 4.8$ can boost the F606W flux and hence the F435W – F606W color. Therefore, to include the missing strong Ly α emitters at $4.5 < z < 4.8$, we also identify a sample of F435W dropout sources using the criteria presented in Bouwens et al. (2021):

$$\begin{aligned} \text{F435W} - \text{F606W} &> 1 \\ \text{F814W} - \text{F115W} &< 1 \\ \text{F435W} - \text{F606W} &> 1.8 \times (\text{F814W} - \text{F115W}) + 1. \end{aligned}$$

We then cross-match the selected F435W dropouts with MUSE Ly α emitters. We add Ly α emitters at $z > 4.5$ that fall in the F435W dropout sample into our $z \sim 5 - 6$ LBG sample.

We visually inspected the *JWST*/NIRCam and *HST*/ACS imaging of every selected Lyman-break galaxy at $z \sim 5 - 6$ to remove suspicious objects usually due to diffraction spikes, hot pixels, or diffuse emission from nearby bright low redshift objects. We also examined whether there are brown dwarfs selected as F606W or F775W dropouts. After cross-matching with the JADES brown dwarf catalog (Hainline et al. 2024a), we find that we are not selecting any brown dwarfs as Lyman break galaxies. AGN were removed by cross-matching our dropouts with AGN catalogs in literature (Maiolino et al. 2023; Lyu et al. 2024; Matthee et al. 2024; Sun et al. in prep.)

Our final LBG sample contains 543 sources at $z \sim 5$ (F606W dropout) and 171 sources at $z \sim 6$ (F775W dropout) in the GOODS-South field overlapped with JADES and MUSE observations. For LBGs with spectroscopic redshift measurements (i.e., either from MUSE Ly α detection or NIRCam grism H α detection), we move those at $4.5 < z_{\text{spec}} < 5.5$ ($5.5 < z_{\text{spec}} < 6.5$) to the $z \sim 5$ ($z \sim 6$) sample no matter whether they were selected as F435W, F606W, or F775W dropouts. Among the total 714 LBGs in our $z \sim 5 - 6$ sample, Ly α emission lines are detected in 167 sources with MUSE observations (Urrutia et al. 2019; Bacon et al. 2017, 2023), and H α emission lines are detected in 161 sources with NIRCam grism observations (Sun et al. in prep.). These include 64 sources with both Ly α and H α emission line detections, comprising all 52 MUSE-identified galaxies at $4.9 < z < 6.5$ with Ly α and H α detections (and NIRCam imaging) introduced in Section 2. The remaining 12 sources have Ly α emission near skylines. In the analysis presented in Section 3, we do not include galaxies with Ly α lines obscured by skylines (see Section 2.1.1). In this section, because we will consider the incompleteness due to skyline obscuration (Section 4.2), we will keep these systems in the LBG sample.

For the 167 LBGs with Ly α detections, we derive their Ly α emission line fluxes and EWs from MUSE spectra using the same approach described in Section 2. For the remaining galaxies without Ly α detection, we put the 5σ upper limit to their Ly α fluxes. The typical 5σ upper limit of flux for galaxies in the MUSE-Wide field is $2 \times 10^{-18} \text{ erg s}^{-1} \text{ cm}^{-2}$, and for galaxies in the MUSE-Deep field is $5 \times 10^{-19} \text{ erg s}^{-1} \text{ cm}^{-2}$ (MOSAIC), $2.5 \times 10^{-19} \text{ erg s}^{-1} \text{ cm}^{-2}$

(UDF-10), or 1×10^{-19} erg s $^{-1}$ cm $^{-2}$ (MXDF). The upper limits of Ly α EW for LBGs without Ly α emission detection are computed using the 5σ upper limits on Ly α flux and the underlying continuum flux densities derived from broadband photometry.

We fit the NIRCcam F090W to F444W SEDs of the 714 LBGs at $z \sim 5-6$ in our sample with BEAGLE models following the same procedures described in Section 2.3. For those without spectroscopic redshifts, we fit the redshift in the range $3 \leq z \leq 8$ assuming a uniform prior. The absolute UV magnitude of our LBGs span a wide range from -21.6 to -16.6 , and the UV slope varies from -3.2 to -0.7 (Fig. 8). The [O III]+H β EWs inferred from BEAGLE models span from ≈ 100 Å to ≈ 5000 Å with a median value of ≈ 704 Å (corresponding to a median CSFH age of ≈ 50 Myr). The properties of these LBGs at $z \sim 5-6$ are comparable to the properties of galaxies in the reionization era (e.g., Endsley et al. 2023a; Topping et al. 2024; Fig. 8), suggesting that our LBG sample provides an ideal baseline for understanding the Ly α properties of $z \gtrsim 7$ galaxies at redshifts where the impact of the neutral IGM is less important.

We then derive the Ly α escape fractions for all the LBGs in our $z \sim 5-6$ sample. Because not all the LBGs have H α line measurements, we derive the intrinsic Ly α luminosities of all our sources from BEAGLE models instead of from the observed H α luminosity to avoid bias against those without H α measurements. From BEAGLE models, we first infer the H α luminosities. To examine whether the SED inferred H α luminosities are robust, we compare the H α fluxes measured from NIRCcam grism spectra with those inferred from BEAGLE models for the 161 LBGs with grism H α detections. We find that on average the grism H α fluxes are 0.82 times of those inferred from SEDs, likely owing to that a small portion of H α emission is missed in the over-subtraction of sky continuum in NIRCcam grism spectra (Sun et al. in prep.). This comparison is consistent with the results found in our $z \approx 5-6$ Ly α emitters (Section 2.4) and in the joint analysis of FRESCO and JADES data by Sun et al. (in prep.). We then correct the BEAGLE inferred H α luminosities for dust attenuation and convert to Ly α luminosities assuming case B recombination (Section 2.4). The Ly α escape fraction of each LBG is computed as the ratio of the observed Ly α luminosity (measured Ly α luminosity for detection, or 5σ upper limit for non-detection) to the model inferred intrinsic Ly α luminosity. We force the Ly α escape fraction to 1 for sources with computed $f_{\text{esc,Ly}\alpha} > 1$.

4.2 Methodology for deriving Ly α property distributions

We establish the distributions of Ly α EW and Ly α escape fraction for our LBGs at $z \sim 5-6$ using a Bayesian approach (Schenker et al. 2014; Endsley et al. 2021; Boyett et al. 2022; Chen et al. 2024). We assume a log-normal distribution for both quantities (Schenker et al. 2014; Endsley et al. 2021; Chen et al. 2024). In this subsection we describe the methodology for deriving the log-normal distribution.

Before deriving the Ly α property distributions, we need to take into account the incompleteness of the Ly α measurements. Ly α emission lines with relatively faint fluxes could be hidden by random noise fluctuations. And since the Ly α lines are measured from the ground, they could be partially obscured by sky lines. Here we estimate the completeness for detecting a Ly α emission line in the MUSE data for a range of redshifts, absolute UV magnitudes, and Ly α EWs. We start by creating a MUSE sky line spectrum at $\lambda = 4800 - 9300$ Å (i.e., the wavelength range covered by the MUSE data) using the average MUSE spectrum. We consider wide grids of redshift ($z = 4.5 - 6.5$), M_{UV} ($= -22$ to -16), and Ly α EW ($= 1 - 1000$ Å), creating a Ly α line profile for each set of parameters (z , M_{UV} , and Ly α EW) assuming a FWHM = 230 km s $^{-1}$ (i.e., equal to the median FWHM

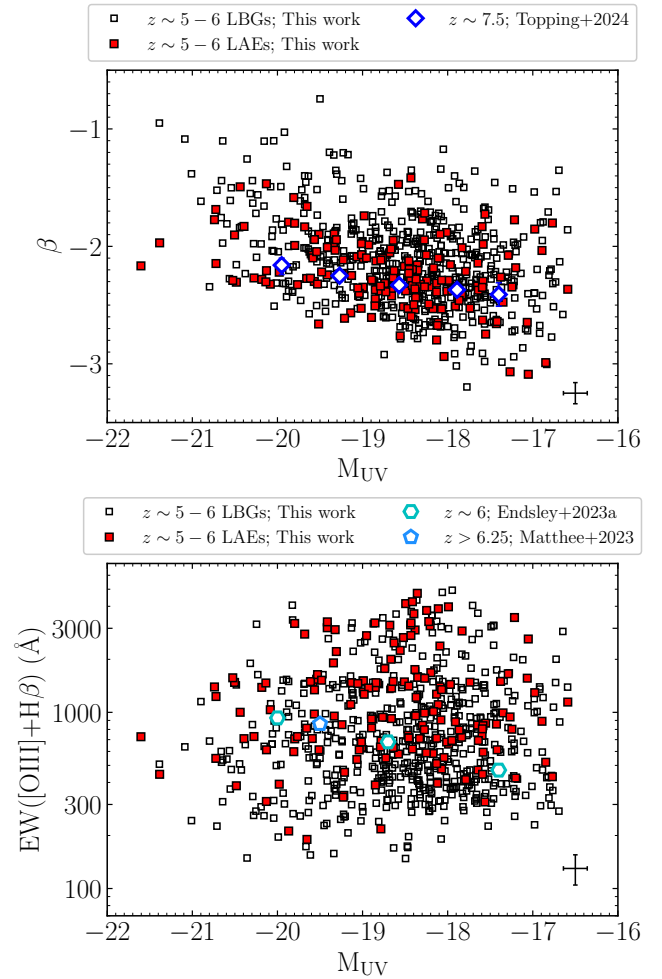


Figure 8. Absolute UV magnitude versus UV slope (top panel) and [O III]+H β EWs (inferred from BEAGLE models; bottom panel) for the LBGs at $z \sim 5-6$ in our sample (open black squares), with those with Ly α detections marked as red squares. The typical uncertainties are shown as the black error bars at the lower right of each panel. As a comparison, we overplot the median UV slope of $z \sim 7$ LBGs (open blue diamonds) presented in Topping et al. (2024) in the top panel, and the median [O III]+H β EWs of $z \sim 5-9$ galaxies (open cyan hexagon; Endsley et al. 2023a; open dodger-blue pentagon; Matthee et al. 2023) in the bottom panel.

The physical properties of our $z \sim 5-6$ LBGs are comparable to the galaxy population in the reionization era.

measured for our Ly α emitters at $z \approx 5-6$). For each Ly α profile, we insert it into the MUSE sky line spectrum 1000 times. And for each simulated emission line spectrum, we randomly perturb the flux density of each wavelength pixel based on the error spectrum. The completeness is calculated as the fraction of realizations in which the emission line is detected at $> 5\sigma$ level.

For either the Ly α EW or the Ly α escape fraction, the distribution is modeled with a set of parameters $\theta = [\mu, \sigma]$, where μ is the mean of the log-normal distribution and σ is the standard deviation. For Ly α EW distribution, we consider uniform priors for the model parameters: $\mu = 0 - 6$ (corresponding to mean Ly α EW $\approx 1 - 400$ Å in linear space) and $\sigma = 0.01 - 3$ (Schenker et al. 2014; Endsley et al. 2021). For Ly α escape fraction distribution, we use an uniform prior for μ ($= -9$ to 0 , corresponding to mean $f_{\text{esc,Ly}\alpha} \approx 0.0001 - 1$

in linear space), and a Gaussian prior for σ (mean = 0.6, standard deviation = 0.3; [Chen et al. 2024](#)).

For each set of model parameters θ , the log-normal distribution is given by

$$p(x|\theta) = \frac{A}{\sqrt{2\pi}\sigma \cdot x} \cdot \exp\left[-\frac{(\ln x - \mu)^2}{2\sigma^2}\right], \quad (1)$$

where x is the Ly α EW or the Ly α escape fraction, and A is the normalization parameter. For the Ly α EW distribution, the normalization parameter A equals 1. For the Ly α escape fraction distribution, because we only consider the range $f_{\text{esc,Ly}\alpha} = 0 - 1$, the normalization parameter is computed as:

$$\int_0^1 p(x|\theta) dx = 1$$

$$A = \frac{2}{1 + \text{erf}[-\mu/(\sqrt{2}\sigma)]}.$$

And for each galaxy with Ly α detection, we also compute the Gaussian measurement uncertainty as

$$p(x)_{\text{obs},i} = \frac{1}{\sqrt{2\pi}\sigma_{\text{obs},i}} \cdot \exp\left[-\frac{(x - x_{\text{obs},i})^2}{2\sigma_{\text{obs},i}^2}\right], \quad (2)$$

where $x_{\text{obs},i}$ and $\sigma_{\text{obs},i}$ are the observed value and the uncertainty of Ly α EW or Ly α escape fraction for the i^{th} object. The likelihood of the entire sample is computed as the product of the individual likelihood of each object in the sample. For each galaxy with Ly α detection (i^{th}), the individual likelihood for Ly α EW distribution is computed as

$$p(\text{obs}, i|\theta)_{\text{det}} = \int_0^{\infty} p(x)_{\text{obs},i} \cdot p(x|\theta) dx. \quad (3)$$

And for Ly α escape fraction distribution the individual likelihood is:

$$p(\text{obs}, i|\theta)_{\text{det}} = \int_0^1 p(x)_{\text{obs},i} \cdot p(x|\theta) dx. \quad (4)$$

For each galaxy without Ly α detection, we write the individual likelihood as

$$p(\text{obs}, i|\theta)_{\text{lim}} = p(x < x_{5\sigma}|\theta) + p(x > x_{5\sigma}|\theta) \cdot (1 - C) \quad (5)$$

The first term $p(x < x_{5\sigma}|\theta)$ considers the likelihood that the Ly α flux is under the 5σ upper limit and thus is undetected. The second term $p(x > x_{5\sigma}|\theta) \cdot (1 - C)$ considers the likelihood that the Ly α flux is larger than the 5σ upper limit, but the emission is not detected due to the impact of skyline obscuration. Here C is the completeness (see Section 4.1).

Now we compute the total likelihood for a given set of parameters as

$$p(\text{obs}|\theta) \propto \prod_i p(\text{obs}, i|\theta) \quad (6)$$

Using Bayes' theorem, we write the posterior probability distribution for the model parameters as

$$p(\theta|\text{obs}) \propto p(\theta) \cdot p(\text{obs}|\theta) \quad (7)$$

where $p(\theta)$ is the prior of model parameters. Finally, we derive the distribution using a Markov Chain Monte Carlo (MCMC) approach to sample the model parameter space using the `emcee` package ([Foreman-Mackey et al. 2013](#)). For each model parameter, we derive its posterior probability distribution and compute the median value and the marginal 68 per cent credible interval.

4.3 Distributions of Ly α EW and Ly α escape fraction

4.3.1 Overview of Ly α EW and Ly α escape fraction distributions

Based on the methodology described in the above subsection, we derive the Ly α EW and Ly α escape fraction distributions for the LBGs at $z \sim 5 - 6$. We note that our distributions are determined using apertures that are equivalent to the *HST* segmentation map convolved with the MUSE PSF, typically corresponding to 1.5 arcsec diameter for the Keck and VLT spectra (Section 2.2). Comparison with observations with other facilities will require modest flux conversions given the different apertures. In particular, we will discuss these conversions when comparing to emerging *JWST*/NIRSpec observations in Section 5.1.

The posterior median values and 68 per cent credible intervals of parameters of log-normal EW distributions are shown in Table 2 and Table 3. For the entire sample, we infer that the parameters of the Ly α EW distribution are $\mu = 2.76_{-0.14}^{+0.13}$ (corresponding to a median Ly α EW = 15 Å) and $\sigma = 1.48_{-0.10}^{+0.11}$. This indicates that strong Ly α emission is common at $z \sim 5 - 6$, with 38_{-4}^{+4} per cent of the LBGs showing Ly α EW > 25 Å (the so-called ‘‘Ly α fraction’’; e.g., [Stark et al. 2010](#)). Focusing on the M_{UV} range that is mostly used in literature ($-20.25 < M_{\text{UV}} < -18.75$), we find that 33_{-5}^{+6} per cent of these systems present Ly α EW > 25 Å. More extreme Ly α emitters (EW > 50 Å) appear less commonly in Lyman break selected samples. Our distributions indicate Ly α fractions of 22_{-3}^{+3} per cent and 11_{-2}^{+2} per cent for EW > 50 Å and 100 Å, respectively.

From the Ly α escape fraction distribution, we see that many $z \simeq 5 - 6$ LBGs transmit a large fraction of their Ly α emission. We find the parameters are $\mu = -2.06_{-0.14}^{+0.14}$ (median $f_{\text{esc,Ly}\alpha} = 0.13$) and $\sigma = 1.55_{-0.15}^{+0.16}$. This suggests that 32_{-4}^{+4} per cent of the $z \sim 5 - 6$ galaxies show $f_{\text{esc,Ly}\alpha} > 0.2$. This is more than 4 times the typical Ly α escape fraction of $z \sim 2$ galaxies (0.05; [Hayes et al. 2010](#)), suggesting the transmission of Ly α emission increases between $z \simeq 2$ and $z \simeq 5 - 6$. Very high escape fractions are also seen in our dataset. Our distribution suggests 11_{-1}^{+1} per cent of the UV continuum selected sample at $z \simeq 5 - 6$ have $f_{\text{esc,Ly}\alpha} > 0.5$. This baseline value will be particularly useful for predicting how commonly we might expect to detect galaxies with similarly large Ly α transmission at $z \gtrsim 7$ with *JWST*. We will come back to discuss this in Section 5.

To assess the impact of the assumed distribution, we also fit our data with a commonly used declining exponential distribution $p(x) = A \cdot \exp(-x/x_0)$ (e.g., [Dijkstra et al. 2011](#); [Jung et al. 2018](#)), where x is Ly α EW or Ly α escape fraction and x_0 is the characteristic e -folding scale of EW or $f_{\text{esc,Ly}\alpha}$. We find that the declining exponential distributions indicate that the fractions of galaxies showing large Ly α EWs or large Ly α escape fractions are similar to those derived from log-normal distributions. Therefore, we argue that choosing different distribution models (log-normal or declining exponential) does not impact our results significantly.

4.3.2 Dependence of Ly α distributions on galaxy properties

One of the primary goals of this subsection is to investigate the dependence of Ly α escape fraction and Ly α EW on galaxy properties. We first explore how the Ly α strength changes with rest-frame UV luminosity. It has been reported that UV-faint galaxies ($M_{\text{UV}} \simeq -19$) present stronger Ly α emission than more luminous systems ($M_{\text{UV}} \simeq -22$ to -20) (e.g., [Shapley et al. 2003](#); [Ando et al. 2006](#); [Stark et al. 2010](#); [De Barros et al. 2017](#); [Arrabal Haro et al. 2018](#)). The 25 – 75 percentile of the M_{UV} distribution in our sample ranges from -19.1 to

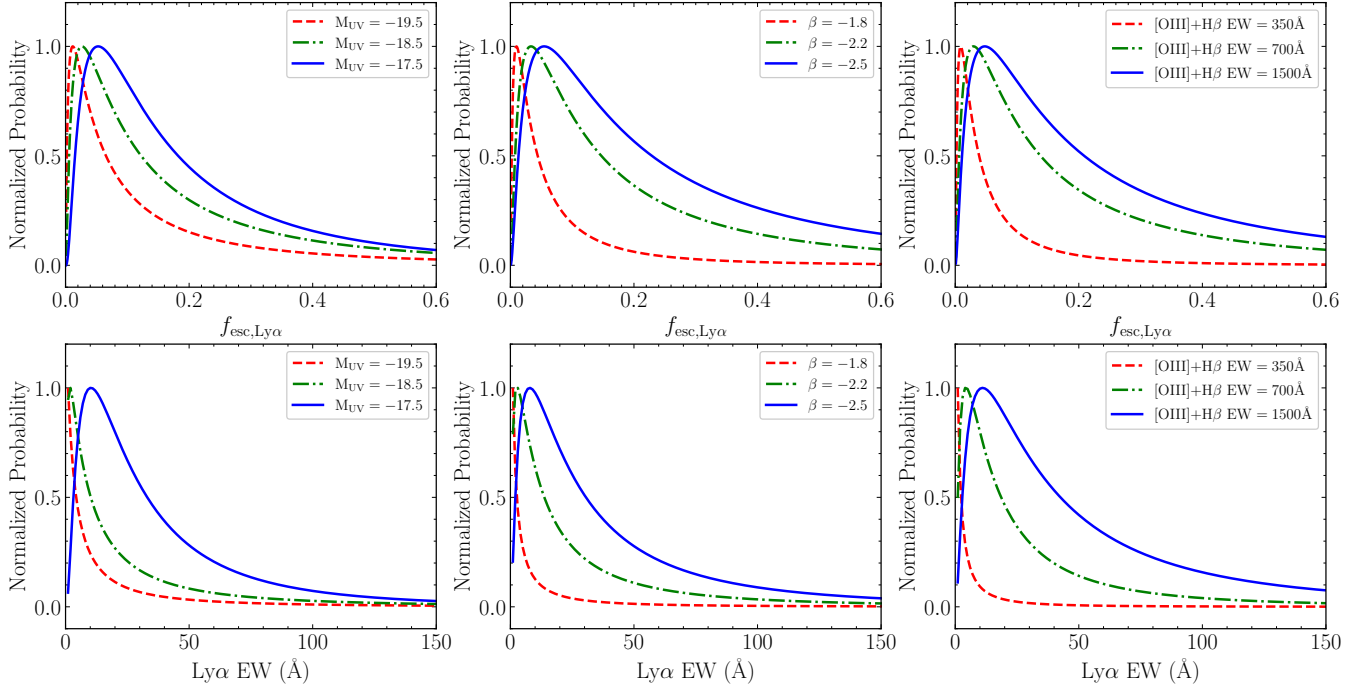


Figure 9. The derived log-normal distributions of Ly α escape fraction (top panels) and Ly α EW (bottom panels) for our LBGs at $z \sim 5 - 6$. We show distributions for different groups of LBGs binned by galaxy properties: absolute UV magnitude (left panels), UV slope (middle panels), and [O III]+H β EW (right panels). Different colors and line styles represent different properties. We see a trend that the average Ly α escape fraction and EW become higher towards fainter M_{UV} , bluer UV slopes, or higher [O III]+H β EWs at $z \sim 5 - 6$.

Sample	N_{gal}	e^μ (Å)	σ (dex)
All	714	15^{+2}_{-3}	$1.48^{+0.11}_{-0.10}$
Median $M_{UV} = -19.5$	238	10^{+2}_{-3}	$1.75^{+0.19}_{-0.17}$
Median $M_{UV} = -18.5$	238	16^{+5}_{-5}	$1.51^{+0.19}_{-0.16}$
Median $M_{UV} = -17.5$	238	27^{+5}_{-5}	$0.99^{+0.17}_{-0.14}$
Median $\beta = -1.8$	238	4^{+1}_{-1}	$1.99^{+0.26}_{-0.24}$
Median $\beta = -2.2$	238	18^{+4}_{-4}	$1.40^{+0.16}_{-0.14}$
Median $\beta = -2.5$	238	29^{+5}_{-4}	$1.16^{+0.14}_{-0.12}$
Median [O III]+H β EW = 350 Å	238	2^{+1}_{-1}	$1.82^{+0.30}_{-0.26}$
Median [O III]+H β EW = 700 Å	238	19^{+3}_{-3}	$1.24^{+0.15}_{-0.13}$
Median [O III]+H β EW = 1500 Å	238	41^{+6}_{-6}	$1.15^{+0.13}_{-0.12}$
$z \sim 5, -20.25 < M_{UV} < -18.75$	138	13^{+4}_{-3}	$1.64^{+0.23}_{-0.19}$
$z \sim 6, -20.25 < M_{UV} < -18.75$	82	8^{+4}_{-3}	$1.85^{+0.42}_{-0.33}$

Table 2. Posterior median values and 68 per cent credible intervals of parameters of Ly α EW distributions for our LBGs at $z \sim 5 - 6$. We list the median Ly α EW (e^μ) and the standard deviation (σ) for each subset, as well as the number of galaxies (N_{gal}).

-17.8 . The *JWST* dataset thus extends to considerably fainter galaxies but does not include the more luminous systems studied previously. To explore the luminosity dependence of Ly α EWs, we divide our $z \sim 5-6$ LBG sample into three groups with equal number of sources: a bright subset $M_{UV} \lesssim -19$ (median $M_{UV} = -19.5$), a moderately faint subset $-19 \lesssim M_{UV} \lesssim -18$ (median $M_{UV} = -18.5$), and a very faint subset $M_{UV} \gtrsim -18$ (median $M_{UV} = -17.5$). The results are consistent with the trend found previously in the literature, with Ly α EW becoming more prominent at lower luminosities. In particular, we find that UV faint galaxies with $M_{UV} \gtrsim -18$ typically show Ly α

Sample	N_{gal}	e^μ	σ (dex)
All	714	$0.13^{+0.02}_{-0.02}$	$1.55^{+0.16}_{-0.15}$
Median $M_{UV} = -19.5$	238	$0.10^{+0.02}_{-0.02}$	$1.46^{+0.19}_{-0.17}$
Median $M_{UV} = -18.5$	238	$0.14^{+0.03}_{-0.03}$	$1.30^{+0.18}_{-0.16}$
Median $M_{UV} = -17.5$	238	$0.16^{+0.03}_{-0.03}$	$1.05^{+0.19}_{-0.17}$
Median $\beta = -1.8$	238	$0.05^{+0.01}_{-0.01}$	$1.28^{+0.20}_{-0.18}$
Median $\beta = -2.2$	238	$0.16^{+0.03}_{-0.03}$	$1.26^{+0.19}_{-0.15}$
Median $\beta = -2.5$	238	$0.24^{+0.06}_{-0.04}$	$1.22^{+0.19}_{-0.16}$
Median [O III]+H β EW = 350 Å	238	$0.04^{+0.04}_{-0.01}$	$1.25^{+0.18}_{-0.17}$
Median [O III]+H β EW = 700 Å	238	$0.16^{+0.04}_{-0.03}$	$1.31^{+0.18}_{-0.15}$
Median [O III]+H β EW = 1500 Å	238	$0.23^{+0.06}_{-0.04}$	$1.25^{+0.18}_{-0.15}$
$z \sim 5, -20.25 < M_{UV} < -18.75$	138	$0.15^{+0.05}_{-0.03}$	$1.36^{+0.19}_{-0.18}$
$z \sim 6, -20.25 < M_{UV} < -18.75$	82	$0.09^{+0.03}_{-0.03}$	$1.15^{+0.21}_{-0.18}$

Table 3. Posterior median values and 68 per cent credible intervals of parameters of Ly α escape fraction distributions for our LBGs at $z \sim 5 - 6$. We list the median Ly α escape fraction (e^μ) and the standard deviation (σ) for each subset, as well as the number of galaxies (N_{gal}).

EWs $2.7\times$ higher than more luminous systems with $M_{UV} \lesssim -19$ (bottom middle panel of Fig. 9) when comparing the mean values of Ly α EW distributions (Table 2). As has been discussed extensively in the literature (e.g., Shapley et al. 2003; Ando et al. 2006; Stark et al. 2010), this luminosity trend is likely related to the dependence of dust content on luminosity (e.g., Bouwens et al. 2009, 2012; Reddy & Steidel 2009), with the more luminous systems presenting more attenuation to Ly α than less luminous galaxies.

Previous studies have revealed significant trends between Ly α strength and UV slope (e.g., Shapley et al. 2003; Stark et al. 2010;

Matthee et al. 2016; Endsley et al. 2021). We quantify this trend in our Lyman break selected $z \sim 5 - 6$ sample. Most earlier results have focused on how the Ly α strength increases between galaxies with significant reddening ($\beta \simeq -1.4$) and those with little sign of reddening ($\beta \simeq -2.0$). Our sample extends to much bluer colors, with the 25-75th percentile values of the slope distribution ranging from $\beta = -2.4$ to -1.9 . How Ly α properties vary between blue ($\beta \simeq -2.0$) and extremely blue ($\beta \simeq -2.5$) is not known observationally. We derive the Ly α escape fraction and Ly α EW distributions for three equally-divided subsets: galaxies with $-2.0 \lesssim \beta \lesssim -1.0$ (median $\beta = -1.8$), $-2.3 \lesssim \beta \lesssim -2.0$ (median $\beta = -2.2$), and $-3.0 \lesssim \beta \lesssim -2.3$ (median $\beta = -2.5$). We do find that the bluest subset presents the largest Ly α escape fractions (top middle panel of Fig. 9). In particular, we find that galaxies with $\beta \simeq -2.5$ have Ly α escape fractions that are on average $4.8\times$ higher than those with $\beta \simeq -1.8$ (Table 2). However, we see the variation of Ly α escape fraction between the $\beta = -2.2$ and $\beta = -2.5$ subsets is less significant, with $f_{\text{esc,Ly}\alpha}$ only increasing by $1.6\times$ (Table 3). We find a similar trend in Ly α EW, with the EW modestly increasing (by a factor of 1.6) from the $\beta = -2.2$ subset to the $\beta = -2.5$ subset (bottom middle panel of Fig. 9). This suggests that the increase in Ly α strength toward bluer colors begins to slow for galaxies with $\beta \lesssim -2$. Physically this may be expected if the variations of UV slope in this regime are less uniformly linked to dust attenuation. It may be other factors less strongly linked to Ly α escape (i.e., gas-phase metallicity, stellar population properties) play a significant role of regulating the UV slope in this blue regime (e.g., Bouwens et al. 2012; Topping et al. 2022; Cameron et al. 2023a).

At lower redshifts ($z \simeq 2 - 3$), it has been shown that strong Ly α emission becomes more common among the most extreme [O III]+H β line emitting galaxies (Du et al. 2020; Tang et al. 2021, 2024, e.g.). We explore this trend in our dataset at $z \sim 5 - 6$. Previous investigations of luminous galaxies ($\gtrsim L_{\text{UV}}^*$) at $z \sim 7$ have revealed that galaxies with large [O III]+H β EWs ($> 800 \text{ \AA}$) also present large Ly α EWs (Endsley et al. 2021). Here we extend this study to the more abundant low luminosity population ($\lesssim L_{\text{UV}}^*$) at the tail end of reionization using our LBG sample. We quantify both the Ly α EW and Ly α escape fraction distributions in three subsets: [O III]+H β EW = 100–500 \AA (median EW = 350 \AA), 500–1000 \AA (median EW = 700 \AA , similar to the average EW of $z > 6$ systems; e.g., Labbé et al. 2013; De Barros et al. 2019; Endsley et al. 2023b), and $> 1000 \text{ \AA}$ (median EW = 1500 \AA), where [O III]+H β EWs are derived from BEAGLE models. We find that the most extreme [O III] emitters have much stronger Ly α emission (bottom right panel of Fig. 9). Comparing to galaxies with [O III]+H β EW $\simeq 350 \text{ \AA}$, those with [O III]+H β EW $\simeq 1500 \text{ \AA}$ show $20\times$ larger Ly α EWs (Table 2). The [O III]+H β EW $\simeq 1500 \text{ \AA}$ galaxies also show Ly α EWs $2\times$ larger than those with more typical [O III]+H β EWs ($\simeq 700 \text{ \AA}$) seen at $z > 5$. We also see that Ly α escape fraction increases with [O III]+H β EW (bottom right panel of Fig. 9). Galaxies with [O III]+H β EW $\simeq 1500 \text{ \AA}$ have Ly α escape fraction $5\times$ higher than those with [O III]+H β EW $\simeq 350 \text{ \AA}$ (Table 3). This may suggest that the transmission of Ly α through the ISM and the CGM is enhanced in the most extreme [O III] emitters, similar to the results found at $z \simeq 2 - 3$ (Tang et al. 2021, 2024) and at $z \gtrsim 6$ (e.g., Boyett et al. 2024). This may be expected if the strong feedback associated with large sSFR disrupts the surrounding gas and boosts the transfer of Ly α photons (e.g., Kimm et al. 2019; Ma et al. 2020; Kakiichi & Gronke 2021). It is likely that the Ly α trend is also influenced by the production efficiency of Ly α , as the largest sSFR galaxies generally produce more ionizing photons per unit star formation rate and hence have larger intrinsic Ly α EWs (e.g., Chen et al. 2024). These results stress the importance of considering rest-frame optical EWs when assessing the visibility of Ly α emission in

the reionization era. In general, [O III]+H β EWs are the most readily constrained from flux excesses in SEDs. Of course in very UV-faint ($M_{\text{UV}} \gtrsim -17$) galaxies with very low metallicities ($Z \lesssim 0.05 Z_{\odot}$), the Ly α emission may reach to very high EWs ($> 100 \text{ \AA}$) while the [O III]+H β EWs are low due to the relatively low number of oxygen atoms (e.g., Endsley et al. 2023a; Maseda et al. 2023).

In the final portion of this section, we investigate the evolution of Ly α fraction with redshift. To be consistent with previous studies, we focus on systems with $-20.25 < M_{\text{UV}} < -18.75$ and derive the Ly α EW distributions at $z \sim 5$ (138 LBGs) and $z \sim 6$ (82 LBGs) separately (Table 2). At $z \sim 5$, we find that 35^{+7}_{-7} per cent of our LBGs show strong Ly α emission with EW $> 25 \text{ \AA}$. Comparing to the Ly α fractions derived at $z \sim 3 - 4$ ($\simeq 15 - 25$ per cent; e.g., Cassata et al. 2015; Arrabal Haro et al. 2018; de La Vieuville et al. 2020; Kusakabe et al. 2020; Goovaerts et al. 2023), this result suggests that strong Ly α emission becomes more common from $z \sim 3$ to $z \sim 5$. This is consistent with previous studies (e.g., Stark et al. 2011; Arrabal Haro et al. 2018; Kusakabe et al. 2020) and also consistent with the implied evolution of the Ly α escape fraction discussed above. We expect the Ly α fraction to increase at higher redshifts due to a combination of the larger sSFRs (e.g., Salmon et al. 2015) and lower dust obscuration in higher redshift galaxies (e.g., Topping et al. 2024). The former leads to higher intrinsic Ly α EWs and the latter boosts the transmission of Ly α inside galaxies, both of which will enhance the observed Ly α EWs as we approach the reionization era.

We also consider the evolution in the Ly α fraction between $z \simeq 5$ and $z \simeq 6$. Whereas we find that the Ly α fraction increases between $z \simeq 3$ and $z \simeq 5$, we do not find clear evidence that this trend continues in the 250 Myr between $z \simeq 5$ and $z \simeq 6$. For systems with $-20.25 < M_{\text{UV}} < -18.75$, the Ly α fraction with EW $> 25 \text{ \AA}$ is broadly consistent at $z \sim 5$ (35^{+7}_{-7} per cent) and $z \sim 6$ (28^{+10}_{-10} per cent). The less rapid evolution at $5 < z < 6$ (relative to $3 < z < 5$) is broadly consistent with the trends found in previous studies (e.g., de La Vieuville et al. 2020; Kusakabe et al. 2020; Goovaerts et al. 2023). We find that the Ly α escape fraction may decrease between $z \simeq 5$ and $z \simeq 6$. At $z \simeq 5$, we find that 28^{+6}_{-6} per cent of our galaxies have Ly α escape fractions with $f_{\text{esc,Ly}\alpha} > 0.2$. At $z \sim 6$, this fraction decreases to 16^{+7}_{-7} per cent. This trend may reflect the impact of the IGM on galaxy samples at $z \simeq 6$. Because the IGM at $z \sim 6$ is not only denser but also slightly more neutral than that at $z \sim 5$ (e.g., Fan et al. 2023), the Ly α photons emerging from $z \sim 6$ galaxies are more likely to be scattered by the residual H I in the IGM, decreasing the Ly α escape fractions.

5 DISCUSSION

In this section, we use our Ly α distributions at $z \simeq 5 - 6$ to investigate Ly α emission in galaxies at $z \gtrsim 8$. We make predictions for $z \gtrsim 8$ Ly α emission line profiles in Section 5.1, and discuss implications of a recently discovered Ly α emitter at $z \simeq 8.5$ in Section 5.2.

5.1 Expectations for Ly α Deep in the Reionization Era

In Section 4, we have derived the range of Ly α properties in Lyman break selected galaxies at $z \simeq 5 - 6$, when the IGM is likely to be mostly ionized. Typical UV-faint galaxies at these redshifts have moderate EW Ly α lines, with median Ly α EW = 15 \AA and Ly α escape fraction = 0.13. The strongest Ly α lines are found more rarely, with only 11 per cent of the population seen with Ly α EW $> 100 \text{ \AA}$. In spite of the large ionized fraction, the IGM is already leaving its imprint on the Ly α distributions at $z \simeq 5 - 6$, with the

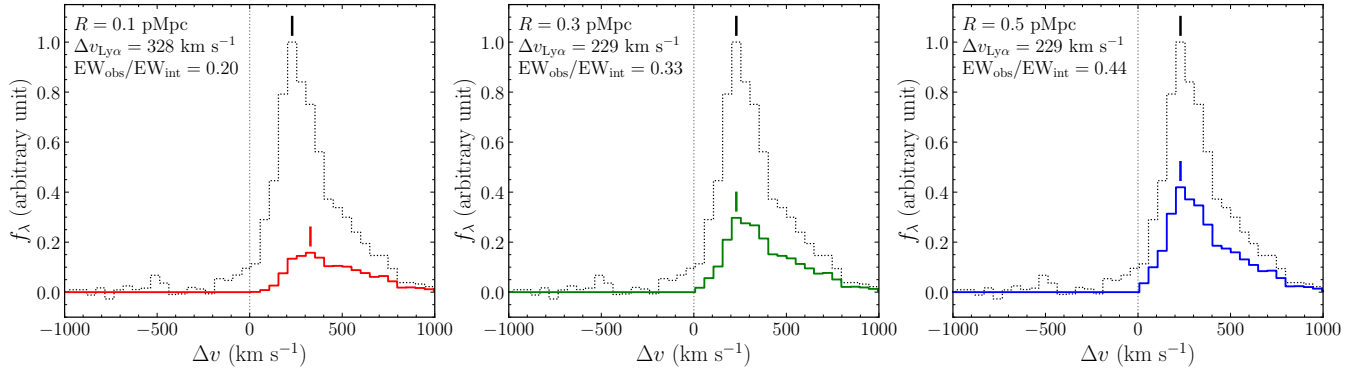


Figure 10. Impact of IGM damping wing absorption to Ly α profile at $z = 8.5$. The black dotted lines show the composite Ly α profile of moderately strong Ly α emitters ($EW = 50 - 100 \text{ \AA}$) at $z \approx 5 - 6$. We assume this profile is the intrinsic Ly α profile of Ly α emitters at $z \geq 7$. To estimate the IGM damping wing absorption, we consider a galaxy at $z = 8.5$ which reside in a series sizes of ionized bubbles ($R = 0.1 \text{ pMpc}$, left; $R = 0.3 \text{ pMpc}$, middle; $R = 0.5 \text{ pMpc}$, right) and adopting the damping wing attenuation calculation in [Miralda-Escudé \(1998\)](#). The resulting Ly α profiles after IGM absorption are shown by solid lines. We mark the Ly α peak velocities of the intrinsic profiles with black vertical lines and the IGM attenuated profiles with colored vertical lines. In a small bubble ($R = 0.1 \text{ pMpc}$), the Ly α peak velocity shifts from $\approx 230 \text{ km s}^{-1}$ to $\approx 330 \text{ km s}^{-1}$. In each panel, we list the Ly α velocity offset after IGM attenuation and the fraction of Ly α photons transmitted through the IGM comparing to the intrinsic value ($EW_{\text{obs}}/EW_{\text{int}}$).

residual H I significantly attenuating those strong Ly α emitters with line flux emerging near the systemic redshift.

At yet higher redshifts, the Ly α will be further weakened by the damping wing from the neutral H I outside of ionized bubbles, leading to the well-established drop in the Ly α fraction at $z \geq 7$ (e.g., [Caruana et al. 2012, 2014](#); [Schenker et al. 2014](#); [Pentericci et al. 2018](#); [Jones et al. 2024](#)). The current frontier of these investigations is at $z \geq 8$, where the neutral fraction is expected to be very large ($x_{\text{HI}} \geq 0.8$; e.g., [Mason et al. 2019](#); [Naidu et al. 2020](#); [Umeda et al. 2023](#); [Nakane et al. 2024](#)) and ionized bubbles are expected to be small. Around faint galaxies ($M_{\text{UV}} > -19$), the median bubble size is predicted to be $\approx 0.1 \text{ pMpc}$ at $z \approx 8$ for standard models where reionization is driven by low mass galaxies (e.g., [Mason & Gronke 2020](#); [Lu et al. 2024](#)). In contrast, only ≈ 10 per cent of faint galaxies ($M_{\text{UV}} > -19$) are predicted to lie in bubbles with $R \geq 0.5 \text{ pMpc}$ in these models ([Lu et al. 2024](#)). If the bubbles are indeed this small at $z \geq 8$, we expect Ly α to be significantly weakened relative to our baseline $z \approx 5 - 6$ model. However these predictions are very sensitive to the nature of the ionizing sources. If reionization is driven by more massive galaxies (e.g., [Naidu et al. 2020](#)), we would expect the ionized volume in the IGM to be dominated by larger structures, with bubbles in excess of $1 - 2 \text{ pMpc}$ potentially present at $z \geq 8$.

Observationally we still have very few Ly α detections at $z \geq 8$, with results mostly revealing upper limits (e.g., [Bunker et al. 2023a](#); [Curtis-Lake et al. 2023](#); [Fujimoto et al. 2023](#); [Nakajima et al. 2023](#); [Harikane et al. 2024](#)). If large bubbles are present, we should begin to find signatures of them in Ly α datasets with *JWST*. We can use our $z \approx 5 - 6$ distributions to investigate the range of Ly α lines that are likely to be found at $z \geq 8$. We consider a range of bubble sizes likely to be common at such high redshifts (0.1, 0.3, and 0.5 pMpc), assuming the neutral fraction is very large (i.e., $x_{\text{HI}} > 0.8$). The IGM will strongly attenuate Ly α at $z \geq 8$, so the galaxies that do present Ly α are likely those that would appear as the very strongest line emitters ($EW > 50 \text{ \AA}$) at $z \approx 5 - 6$. We thus consider Ly α profiles from our $z \approx 5 - 6$ composites as our input ‘‘intrinsic’’ models prior to attenuation from the IGM H I damping wing. We use both a moderate EW Ly α composite ($EW = 50 - 100 \text{ \AA}$) and one that includes extremely strong Ly α ($EW = 100 - 500 \text{ \AA}$). The composites

are derived following the procedures described in Section 3.2. Both stacks reveal roughly similar profiles, with Ly α peaked at redshifted velocity of $\approx 210 \text{ km s}^{-1}$ (black dotted lines in Fig. 10). We then apply the H I damping wing opacity to these profiles, assuming our three different ionized bubble sizes. In this simple model, we assume that H I transitions from fully ionized to fully neutral at the bubble radius.

The results are shown in Fig. 10. Here we focus on the moderate EW Ly α composite ($EW = 50 - 100 \text{ \AA}$), but the results do not differ if we were instead to adopt the stronger Ly α composite. Both have similar line profiles and thus will have comparable attenuation from the IGM damping wing. We see that the Ly α transmission tracks the bubble size, increasing from $\mathcal{T}_{\text{Ly}\alpha} = 0.20$ ($R = 0.1 \text{ pMpc}$) to 0.33 ($R = 0.3 \text{ pMpc}$), and finally to 0.44 ($R = 0.5 \text{ pMpc}$). The IGM damping wing removes preferentially more flux near the line center, which can shift the emergent Ly α profile to higher velocities. This is most prominent in galaxies situated in the smallest bubbles. In the mock Ly α spectrum, we see that in the $R = 0.1 \text{ pMpc}$ bubble the peak velocity shifts from 210 km s^{-1} to 328 km s^{-1} . Even if we consider an input Ly α profile with small velocity offset of $\approx 100 \text{ km s}^{-1}$ (i.e., consistent with the lowest Ly α velocity offsets seen in our $z \approx 5 - 6$ sample), we still find that in the $R = 0.1 \text{ pMpc}$ bubble the peak velocity shifts to $\geq 300 \text{ km s}^{-1}$. In the $R = 0.3$ and 0.5 pMpc bubbles, this effect is less significant given the reduced IGM opacities associated with these bubble sizes.

Given the IGM transmission factors derived above, we expect that the strongest Ly α emitters in our baseline $z \approx 5 - 6$ sample ($EW > 100 \text{ \AA}$) would have much weaker lines ($\geq 20 - 40 \text{ \AA}$) at $z \geq 8$. Recalling that only 10 per cent of $z \approx 5 - 6$ galaxies have Ly α with $EW > 100 \text{ \AA}$, this suggests that we must observe of order 10 $z \geq 8$ galaxies to recover a Ly α line with $EW > 20 \text{ \AA}$ if typical bubble sizes are in the range 0.1 – 0.5 pMpc. The velocity offsets of these strong Ly α emitters should be close to the intrinsic values seen at $z \approx 5 - 6$ ($\approx 200 \text{ km s}^{-1}$), provided bubble sizes are $R = 0.3 \text{ pMpc}$ and larger. If we were to discover stronger Ly α emitters at $z \geq 8$, it is likely to be a signpost of an unexpected population of yet larger bubbles. We must further account for the aperture corrections required to predict the Ly α flux in the NIRSpect microshutters. We have estimated

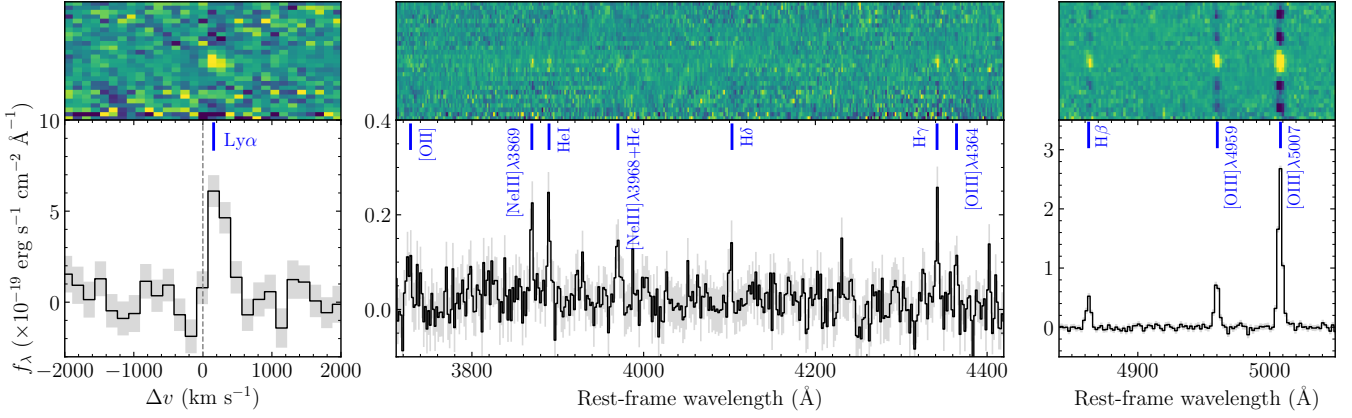


Figure 11. JADES 2D (top) and 1D (bottom) NIRSpect medium resolution grating spectra of the $z = 8.49$ Ly α emitter JADES-GS-z8.5-LAE. The error spectra are shown as the grey-shaded regions. Left panel: G140M/F070LP spectrum showing the region near the Ly α emission line. The detected Ly α line has EW = 17 Å and velocity offset $\Delta v_{\text{Ly}\alpha} = 156 \text{ km s}^{-1}$. Middle and right panels: G395M/F290LP spectrum showing rest-frame optical emission lines.

(see Section 2.2) that we are likely to recover ≈ 80 per cent of the emission recovered in our ground-based surveys, where this estimate is based on the expected Ly α surface brightness profiles (assuming they do not evolve with redshift), suggesting these EWs may be somewhat lower ($\gtrsim 16 - 32$ Å). Galaxies seen with moderate EW Ly α emission at $z \approx 5 - 6$ (EW = 50 Å) would be even weaker (8 – 16 Å) at $z \gtrsim 8$. We note that these values may change slightly if the surface brightness profiles are different at $z \gtrsim 8$, or if galaxies are significantly off-centered in the microshutter. Regardless, these estimates give a blueprint for what the strongest Ly α emitters are likely to look like at $z \gtrsim 8$, both in terms of their EW and velocity offset. We apply this blueprint to the existing *JWST*/NIRSpect public database in the next subsection.

5.2 New detection of Ly α emission at $z \approx 8.5$ with low $\Delta v_{\text{Ly}\alpha}$

With spectroscopic samples rapidly growing at $z \gtrsim 8$ (e.g., Bunker et al. 2023a; Curtis-Lake et al. 2023; Fujimoto et al. 2023; Nakajima et al. 2023; Harikane et al. 2024), it is now possible to extend the search for Ly α emitting galaxies to this early epoch. To date, there are only three galaxies in the literature at $z > 8$ with robust Ly α detections (Zitrin et al. 2015; Larson et al. 2022; Bunker et al. 2023b). All these three galaxies have large velocity offsets ($\Delta v_{\text{Ly}\alpha} \gtrsim 400 \text{ km s}^{-1}$) and relatively weak Ly α (EW $\lesssim 10 - 20$ Å; Zitrin et al. 2015; Larson et al. 2022, 2023; Bunker et al. 2023b; Tang et al. 2023). Two of these three galaxies with Ly α detections were identified in the Extended Groth Strip (EGS; Davis et al. 2007) field at $z \approx 8.7$ (Zitrin et al. 2015; Larson et al. 2022). Given their close proximity (≈ 4 pMpc) and the potential location of a galaxy overdensity in their surroundings (Leonova et al. 2022; Whitler et al. 2024), it has been suggested that these two systems trace a large ionized bubble at $z \approx 8.7$. An additional Ly α emitter at $z = 7.98$, JADES-GS+53.15682-27.76716, has been reported in the literature (Jones et al. 2024; Saxena et al. 2024; Witstok et al. 2024b). This galaxy has a relatively low Ly α velocity offset ($\Delta v_{\text{Ly}\alpha} = 167 \text{ km s}^{-1}$) and strong Ly α emission (EW ≈ 29 Å) among the existing $z \gtrsim 8$ galaxies with Ly α measurements. Further progress will require identification of more Ly α emitters at $z \gtrsim 8$, with particular attention to those with elevated EWs (> 15 Å) and small velocity offsets ($\lesssim 200 \text{ km s}^{-1}$) which may be signposts

of moderate or larger size ($R \gtrsim 0.3$ pMpc) ionized bubbles (Section 5.1).

As part of an ongoing effort to build a large database of Ly α measurements in the reionization era, we have identified a new Ly α detection at $z \approx 8.5$, JADES-GS+53.15891-27.76508 (hereafter JADES-GS-z8.5-LAE), in the JADES Cycle 2 program 3215 (Eisenstein et al. 2023b; D’Eugenio et al. 2024). The discovery of this Ly α emitting galaxy is also presented and discussed in Witstok et al. (2024a, ID: JADES-GS-z8-0-LA therein). This object was initially selected as a F105W-dropout from *HST* imaging in the HUDF (Bouwens et al. 2010b; Bunker et al. 2010; McLure et al. 2010). Lehnert et al. (2010) obtained spectroscopic observations of this galaxy with VLT/SINFONI (Eisenhauer et al. 2003), presenting a 6σ detection of Ly α emission at $z = 8.5549$ with a line flux of $6.1 \times 10^{-18} \text{ erg s}^{-1} \text{ cm}^{-2}$ and a rest-frame EW ≈ 200 Å. Later Bunker et al. (2013) reported the spectroscopic observations on this source with VLT/XSHOOTER (D’Odorico et al. 2006) and Subaru/MOIRCS (Ichikawa et al. 2006). These observations were unable to reproduce the line reported in Lehnert et al. (2010), placing a 2σ upper limit on the line flux of $\lesssim 2 \times 10^{-18} \text{ erg s}^{-1} \text{ cm}^{-2}$. Then NIRCcam imaging observations of JADES-GS-z8.5-LAE were obtained from the JADES Cycle 1 program (Eisenstein et al. 2023a). It was also selected as a candidate high redshift galaxy with photometric redshift $z_{\text{phot}} = 8.5$ using the dropout technique in Hainline et al. (2024b). NIRSpect observations of this source were performed as a part of the program 3215 using the MSA in October 2023 over five sub-pointings. Each pointing has an exposure time of 33263 s for the low spectral resolution ($R \sim 100$) PRISM/CLEAR setup, and 8316 s and 33263 s for the medium resolution (MR; $R \sim 1000$) G140M/F070LP and G395M/F290LP grating/filter setups, respectively. We refer readers to D’Eugenio et al. (2024) for details of the target selection and the follow up NIRSpect observations.

The NIRSpect spectra used here were reduced following the procedures described in Tang et al. (2023). In Fig. 11, we show the MR grating spectra of JADES-GS-z8.5-LAE. Strong rest-frame optical emission lines (H β , [O III]) are clearly seen in both the prism and the G395M/F290LP spectra. We derive the systemic redshift $z_{\text{sys}} = 8.4858 \pm 0.0004$ by simultaneously fitting those strong rest-frame optical lines measured in G395M/F290LP spectrum with Gaussian profiles. The Ly α emission line of JADES-GS-z8.5-LAE is detected

in the G140M/F070LP spectrum (Fig. 11). We measure the Ly α flux by directly integrating the flux density within a ± 1000 km s $^{-1}$ window, obtaining $F_{\text{Ly}\alpha} = 7.44 \pm 1.27 \times 10^{-19}$ erg s $^{-1}$ cm $^{-2}$. The rest-frame UV continuum of this galaxy is below the noise fluctuation in the G140M/F070LP spectrum, but is well detected in the prism spectrum. We measure the continuum flux density near the Ly α emission from the prism spectrum following the methods in [Chen et al. \(2024\)](#). We derive that the rest-frame Ly α EW is 21 ± 4 Å. Using the peak of the Ly α emission line measured in the G140M/F070LP spectrum, we calculate the Ly α redshift $z_{\text{Ly}\alpha} = 8.4907 \pm 0.0005$. This results in a Ly α velocity offset $\Delta v_{\text{Ly}\alpha} = 156 \pm 20$ km s $^{-1}$. We also constrain the Ly α escape fraction of JADES-GS-z8.5-LAE using the H β emission line flux (Table 4). Assuming case B recombination with $T_e = 10^4$ K, $n_e = 10^2$ cm $^{-3}$, the intrinsic Ly α /H β luminosity ratio is 24.9. By measuring of the H γ /H β ratio, we derive the dust attenuation is relatively small (details in the next paragraph) and correct the observed H β luminosity to the intrinsic value. Then we calculate the Ly α escape fraction $f_{\text{esc,Ly}\alpha} = 0.10 \pm 0.02$. The Ly α emission line of JADES-GS-z8.5-LAE detected in the NIRSpec spectra is ≥ 2000 km s $^{-1}$ bluewards the line shown in the VLT/SINFONI spectrum ($z = 8.5549$; [Lehnert et al. 2010](#)), with much lower line flux and EW than those reported in [Lehnert et al. \(2010\)](#), $F_{\text{Ly}\alpha} = 6.1 \times 10^{-18}$ erg s $^{-1}$ cm $^{-2}$, $\text{EW}_{\text{Ly}\alpha} \approx 200$ Å. These results are in disagreement with [Lehnert et al. \(2010\)](#), consistent with the upper limit ($F_{\text{Ly}\alpha} < 2 \times 10^{-18}$ erg s $^{-1}$ cm $^{-2}$) placed in [Bunker et al. \(2013\)](#).

Before discussing the potential bubble size this $z \approx 8.5$ source might sit in, we first investigate the physical properties of the galaxy, characterizing the rest-frame optical emission line properties and the NIRCam SED. Our analysis follows that presented in [Tang et al. \(2023\)](#). We present the detected emission lines of JADES-GS-z8.5-LAE in Table 4. We find strong [O III] emission lines with [O III] $\lambda 5007$ EW = 1250 Å, consistent with systems dominated by very young stellar populations (e.g., [Tang et al. 2019](#)). The Balmer emission line detections (H γ , H β) allow us to estimate the dust attenuation in nebular gas. We measure H γ /H β = $0.442^{+0.097}_{-0.087}$, close to the intrinsic H γ /H β ratio expected in the case B recombination (0.468, assuming $T_e = 10^4$ K; [Osterbrock & Ferland 2006](#)). This implies a relatively small extinction with $E(B - V) = 0.11$ assuming the [Cardelli et al. \(1989\)](#) extinction curve. With dust attenuation inferred from Balmer decrement, we quantify the ionization-sensitive [O III]/[O II] (O32; dust-corrected) and [Ne III]/[O II] (Ne3O2) ratios. These line ratios are large, with O32 = 18^{+8}_{-4} and Ne3O2 = $1.1^{+0.6}_{-0.4}$. These values are consistent with those found in galaxies at $z = 5 - 9$ (e.g., [Cameron et al. 2023b](#); [Sanders et al. 2023](#); [Saxena et al. 2024](#); [Tang et al. 2023](#)), well above the average ratios measured in galaxies at $z < 5$ (O32 $\approx 1 - 5$ and Ne3O2 $\approx 0.1 - 0.4$; e.g., [Sanders et al. 2016](#); [Steidel et al. 2016](#); [Shapley et al. 2023](#)). This indicates extreme ionizing conditions in this galaxy. We detect a tentative [O III] $\lambda 4363$ emission line with S/N = 3, enabling us to constrain the gas-phase oxygen abundance with direct method. Following the procedures in [Izotov et al. \(2006\)](#), we derive that the nebular gas of JADES-GS-z8.5-LAE is very metal-poor with $12 + \log(\text{O}/\text{H}) = 7.37^{+0.21}_{-0.10}$ ($0.05^{+0.02}_{-0.01} Z_{\odot}$, where the solar metallicity corresponds to a gas-phase oxygen abundance $12 + \log(\text{O}/\text{H}) = 8.71$; [Gutkin et al. 2016](#)). Using the strong-line ratio R23 $\equiv ([\text{O III}] + [\text{O II}])/\text{H}\beta$ ($= 7.0^{+0.9}_{-0.6}$) and applying the empirical metallicity calibration derived from $z = 2 - 9$ galaxies ([Sanders et al. 2024](#)), we derive the gas-phase oxygen abundance $12 + \log(\text{O}/\text{H}) = 7.31^{+0.11}_{-0.09}$ similar to that inferred from direct method.

The NIRCam photometry of JADES-GS-z8.5-LAE is computed

Line	$\lambda_{\text{rest,vacuum}}$ (Å)	Flux ($\times 10^{-20}$ erg s $^{-1}$ cm $^{-2}$)
Ly α	1215.67	74.4 ± 12.7
[O II]	3727.1, 3729.9	7.2 ± 2.2
[Ne III]	3869.8	7.6 ± 2.5
He I	3889.8	8.2 ± 2.1
[Ne III]+H ϵ	3968.6, 3971.2	10.3 ± 2.1
H δ	4102.9	6.0 ± 1.8
H γ	4341.7	9.6 ± 1.7
[O III]	4364.4	4.2 ± 1.4
H β	4862.7	21.6 ± 2.5
[O III]	4960.3	34.3 ± 2.9
[O III]	5008.2	110.0 ± 2.6

Table 4. Emission lines detected in the NIRSpec spectrum of JADES-GS+53.15891-27.76508. Line fluxes are measured from the MR grating spectrum.

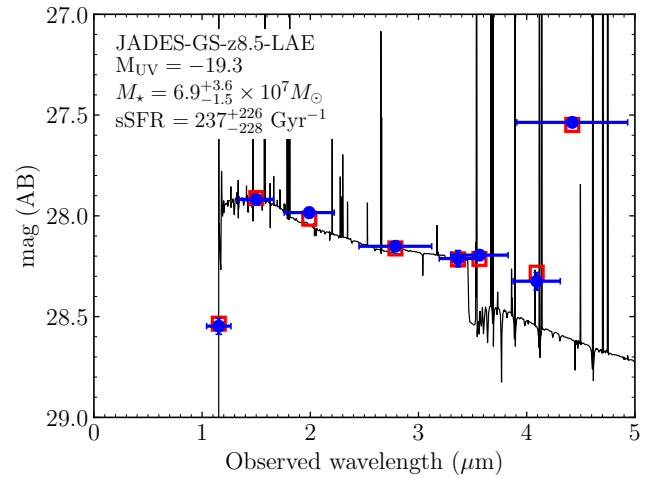


Figure 12. JADES NIRCam SED of JADES-GS-z8.5-LAE. Observed NIRCam photometry is shown by blue circles. The BEAGLE model spectrum is shown by the black line and the synthetic photometry is presented by open red squares.

following the procedures described in [Rieke et al. \(2023b\)](#) which will also be fully described in Robertson et al. (in prep.). The SED is shown in Fig. 12, demonstrating that it has $M_{\text{UV}} = -19.3$. The UV slope is blue ($\beta = -2.2$), consistent with the low dust attenuation inferred from Balmer decrement measurement. We fit the NIRCam SED of this galaxy with BEAGLE models following the same methods described in Section 2.3. The SED fitting results demonstrate that JADES-GS-z8.5-LAE has relatively low stellar mass with $M_{\star} = 6.9^{+3.6}_{-1.5} \times 10^7 M_{\odot}$. The rest-frame UV to optical light of this object is dominated by very young stellar populations (luminosity-weighted age = $1.6^{+0.7}_{-0.4}$ Myr), as expected for galaxies that have undergone a recent upturn in star formation.

The discovery of Ly α emission at $z \approx 8.5$ with a small velocity offset from the line center is suggestive of a moderate bubble size. Based on our mock Ly α profiles presented in Section 5.1, we would expect extremely small bubbles ($\lesssim 0.1$ pMpc) to have shifted line emission to larger velocities (> 300 km s $^{-1}$). We may therefore expect the galaxy to be situated in a bubble of order 0.3 pMpc or larger, significantly above the median value expected if the IGM

JADES ID	z_{phot}	M_{UV}
JADES-GS+53.13364-27.77895	$8.30^{+0.14}_{-0.11}$	-18.2 ± 0.1
JADES-GS+53.13939-27.78334	$8.35^{+0.09}_{-0.24}$	-18.0 ± 0.1
JADES-GS+53.15047-27.79684	$8.37^{+0.05}_{-0.24}$	-17.4 ± 0.1
JADES-GS+53.13621-27.77716	$8.43^{+0.19}_{-0.26}$	-17.8 ± 0.1
JADES-GS+53.18075-27.76077	$8.43^{+0.21}_{-0.26}$	-17.4 ± 0.1
JADES-GS+53.19495-27.78067	$8.45^{+0.14}_{-0.22}$	-18.1 ± 0.1
JADES-GS+53.15576-27.75095	$8.45^{+0.03}_{-0.30}$	-17.5 ± 0.1
JADES-GS+53.13356-27.77870	$8.48^{+0.21}_{-0.22}$	-18.1 ± 0.2
JADES-GS+53.17292-27.76656	$8.48^{+0.34}_{-0.37}$	-17.1 ± 0.1
JADES-GS+53.16326-27.76361	$8.48^{+0.08}_{-0.07}$	-17.5 ± 0.1
JADES-GS+53.16717-27.75152	$8.49^{+0.22}_{-0.24}$	-17.9 ± 0.1
JADES-GS+53.17861-27.74042	$8.50^{+0.24}_{-0.34}$	-18.5 ± 0.1
JADES-GS+53.16447-27.80218 ^a	$8.51^{+0.01}_{-0.12}$	-18.7 ± 0.1
JADES-GS+53.17770-27.78477	$8.52^{+0.12}_{-0.03}$	-18.2 ± 0.1
JADES-GS+53.18354-27.77014 ^b	$8.54^{+0.20}_{-0.02}$	-19.7 ± 0.1
JADES-GS+53.16337-27.77569	$8.54^{+0.20}_{-0.18}$	-17.8 ± 0.1
JADES-GS+53.16668-27.76126	$8.54^{+0.31}_{-0.26}$	-17.3 ± 0.2
JADES-GS+53.13377-27.78061	$8.54^{+0.26}_{-0.39}$	-18.0 ± 0.3
JADES-GS+53.14091-27.77279	$8.56^{+0.20}_{-0.03}$	-17.7 ± 0.1
JADES-GS+53.15106-27.75698	$8.59^{+0.17}_{-0.40}$	-18.1 ± 0.1
JADES-GS+53.14453-27.75413	$8.60^{+0.19}_{-0.19}$	-17.7 ± 0.1
JADES-GS+53.17257-27.79305	$8.65^{+0.19}_{-0.31}$	-16.8 ± 0.2
JADES-GS+53.17121-27.76998	$8.68^{+0.21}_{-0.12}$	-16.9 ± 0.2
JADES-GS+53.18467-27.79088	$8.69^{+0.13}_{-0.07}$	-18.0 ± 0.1

Table 5. JADES sources at $z \simeq 8.5$ within 2 arcmin from JADES-GS-z8.5-LAE identified in Hainline et al. (2024b) photometric redshift catalog. a: JADES-GS+53.16447-27.80218 has spectroscopic redshift ($z_{\text{spec}} = 8.473$) measured from JADES NIRSpec spectrum (Bunker et al. 2023a). b: JADES-GS+53.18354-27.77014 has spectroscopic redshift ($z_{\text{spec}} = 8.385$) measured from FRESCO NIRCам grism spectrum (Sun et al. in prep.).

neutral fraction is $x_{\text{HI}} \simeq 0.9$. If the bubble is 0.3 or 0.5 pMpc, the Ly α EW would be attenuated by 2–3 \times by the IGM damping wing. This would imply the galaxy would have been observed with Ly α EW = 40–50 Å at $z \simeq 5 - 6$ (or 50–60 Å after accounting for the small aperture correction).

More robust inferences of bubble sizes will require Ly α observations of other galaxies surrounding JADES-GS-z8.5-LAE. If the galaxy is situated in a moderate-sized bubble, we would expect to see numerous other ionizing sources surrounding the galaxy, many of which should also show Ly α . We search for additional sources at $z \simeq 8.5$ within 2 arcmin (physical separation $\simeq 0.6$ pMpc in projection at $z = 8.5$) from JADES-GS-z8.5-LAE. We utilize the up-to-date version of the JADES photometric redshift catalog created by Hainline et al. (2024b). The photometric redshifts in Hainline et al. (2024b) catalog were computed using the EAZY code (Brammer et al. 2008), taking advantage of JWST/NIRCам and HST/ACS imaging data. We select sources with $8.3 \leq z_{\text{phot}} \leq 8.7$ and < 2 arcmin away from JADES-GS-z8.5-LAE. To ensure the photometric redshifts are robust, we additionally require the 1σ confidence interval of the photometric redshift of each object is $z_{168} \geq 8.1$ and $z_{868} \leq 8.9$, where z_{168} and z_{868} are the lower and upper bound of the 1σ confidence interval. Adopting the above criteria we identify 24 sources at $z \simeq 8.5$ within 2 arcmin around JADES-GS-z8.5-LAE (Table 5). Most of these 24 galaxies are less luminous than JADES-GS-z8.5-LAE ($M_{\text{UV}} = -19.3$), with M_{UV} spanning a range from -19.7 to -16.8 with a median of $M_{\text{UV}} = -17.9$.

Among the 24 photometric redshift selected galaxies around JADES-GS-z8.5-LAE, two have already been spectroscopically confirmed. JADES-GS+53.18354-27.77014 has spectroscopic redshift

measured from the FRESCO dataset (Oesch et al. 2023). The resolved [O III] $\lambda 4959$ and [O III] $\lambda 5007$ doublet is detected in the NIRCам F444W grism spectrum obtained by the FRESCO survey, and the spectroscopic redshift measured for this galaxy is $z_{\text{spec}} = 8.385$ (Sun et al. in prep.). This galaxy is the brightest source among the above 24 objects around JADES-GS-z8.5-LAE, with $H_{150} = 27.5$ and $M_{\text{UV}} = -19.7$. In physical distance, JADES-GS+53.18354-27.77014 is 2.9 pMpc away from JADES-GS-z8.5-LAE, likely outside of any bubble that exists around the Ly α emitter. JADES-GS+53.16447-27.80218 is another galaxy with spectroscopic observation around JADES-GS-z8.5-LAE. It was observed with NIRSpec in the JADES program 1210, and the spectroscopic measurements were presented in Bunker et al. (2023a). [O III] and H β emission lines of this galaxy are detected from the NIRSpec spectrum, revealing a spectroscopic redshift $z_{\text{spec}} = 8.473$. This object has $H_{150} = 28.5$ and $M_{\text{UV}} = -18.7$ and is only 0.7 pMpc away from JADES-GS-z8.5-LAE, much closer than the other spectroscopically confirmed source. Deep spectroscopic follow-up of the other 22 photometric sources should better characterize the overdensity around JADES-GS-z8.5-LAE. If the bubble is large, we would expect additional sources to show Ly α with small velocity offsets. A separate analysis of the overdensity and the ionized bubble around JADES-GS-z8.5-LAE is presented in Witstok et al. (2024a).

6 SUMMARY

JWST has recently sparked a new era of Ly α spectroscopy at $z \gtrsim 7$. To fully realize the potential of these observations to provide a new insight into reionization, we need a much-improved understanding of Ly α emission in galaxies at $z \simeq 5 - 6$ when the IGM is mostly ionized. Using Ly α emission lines measured from ground-based Keck and VLT spectroscopic surveys and JWST observations from the JADES and FRESCO surveys, we characterize the Ly α EWs, escape fractions, and velocity offsets of $z \simeq 5 - 6$ galaxies. These measurements are meant to provide an “intrinsic” model to interpret the impact of the IGM H I damping wing absorption on Ly α emission at $z \gtrsim 7 - 12$. We summarize our key results below.

1. We identify 79 galaxies with Ly α and H α emission line detections at $z \simeq 5 - 6$, and we measure the Ly α EWs and Ly α escape fractions. We investigate the nature of Ly α emitters with EW > 100 Å, a population that is becoming very important in efforts to study the IGM at $z \gtrsim 7$ (Saxena et al. 2023; Chen et al. 2024). We find that the most significant difference between galaxies with moderate-EW Ly α (EW = 10–50 Å) and extremely strong Ly α ($> 100 - 300$ Å) is the transmission of Ly α through the ISM and CGM, with the most intense Ly α emitters tending to be those that leak over 60 per cent of their Ly α emission (compared to 10–20 per cent for the weaker line emitters). While Ly α EW also increases with ionizing photon production efficiency, we find that this quantity is not significantly different between moderate-EW and strong Ly α emitters.

2. We characterize the Ly α velocity offsets of the 79 Ly α emitters with H α detections. We find significant evolution in the velocity profiles of the strongest $z \simeq 5 - 6$ Ly α emitters with respect to those at $z \simeq 2 - 3$. At the lower redshifts, very intense Ly α emitters (> 100 Å) tend to have profiles that peak near the line center, likely reflecting direct escape of Ly α through very low H I density channels in the ISM and CGM. However at $z \simeq 5 - 6$, we find that the strongest Ly α emitters are significantly redshifted from the line center (median $\simeq 200$ km s $^{-1}$) with negligible Ly α central escape fractions. Galaxies with low velocity offsets (< 100 km s $^{-1}$) are extremely rare in our $z \simeq 5 - 6$ sample. The disappearance of Ly α emitters with

very low velocity offsets and large Ly α central escape fractions at $z \approx 5 - 6$ is likely driven by the IGM, with the residual H I fraction ($x_{\text{HI}} \gtrsim 10^{-4}$; e.g., Yang et al. 2020b; Bosman et al. 2022) large enough to resonantly scatter line photons near the line center given the high IGM density at $z \approx 5 - 6$. Given the link between low velocity offsets and LyC leakage (e.g., Verhamme et al. 2015; Choustikov et al. 2024a), these results suggest that strong Ly α emitters may not provide the best indicator of ionizing photon escape at $z \approx 5 - 6$.

3. The blue side of Ly α is also strongly attenuated by the mostly-ionized IGM at $z \approx 5 - 6$. Several recent detections of blue peaks at these redshifts have been challenging to explain, requiring either inflows or locally intense radiation fields. We constrain the strength of blue peak Ly α emission for the 79 galaxies with Ly α and H α detections in our $z \approx 5 - 6$ sample. In 77 of the 79 galaxies we do not find blue peak Ly α emission. The average blue-to-red flux ratio (< 0.04 at 5σ) is much smaller than that of Ly α emitters at $z \approx 0 - 2$ (≈ 0.3 ; e.g., Hayes et al. 2021; Matthee et al. 2021), consistent with expectations given the increasing IGM opacity at $z \approx 5 - 6$. We identify blue peak Ly α emission in two galaxies in our sample, with blue-to-red flux ratio = 0.06 and 0.07. This is $5 - 10\times$ below the ratios found in several cases in the literature at $z \approx 5 - 6$. These results suggest that very prominent blue peaks are rare at $z \approx 5 - 6$.

4. We derive statistical distributions of Ly α properties in a Lyman break selected sample at $z \approx 5 - 6$, with the goal of providing baseline models for comparison against $z \gtrsim 7$ studies. We find that galaxies with large Ly α escape fractions ($f_{\text{esc,Ly}\alpha} > 0.2$) or Ly α EWs ($> 25 \text{ \AA}$) are common at $z \approx 5 - 6$, comprising $\approx 30 - 40$ per cent of the Lyman break selected population. Our results suggest that strong Ly α emission with EW $> 25 \text{ \AA}$ becomes more common from $z \sim 3$ to $z \sim 5$, consistent with previous findings. We find that the evolution of the Ly α fraction begins to plateau between $z \sim 5$ (35^{+7}_{-7} per cent) and $z \sim 6$ (28^{+10}_{-10} per cent), likely reflecting the attenuation provided by the IGM at higher redshifts. We investigate the dependence of Ly α escape fraction and Ly α EW on galaxy properties, quantifying trends with UV luminosity, UV slope, and [O III]+H β EW.

5. Using the statistical distributions at $z \approx 5 - 6$, we investigate the likely impact of the IGM damping wing on Ly α at $z \gtrsim 8$. At these very high redshifts, little is still known about Ly α . We demonstrate that typical lines are likely to be attenuated by $3 - 5\times$ owing to the strong damping wing associated with small ionized bubbles ($\lesssim 0.3 \text{ pMpc}$). We show that small velocity offsets ($\Delta v_{\text{Ly}\alpha} \lesssim 250 \text{ km s}^{-1}$) are mostly likely to be observed in moderate-size bubbles ($\gtrsim 0.3 \text{ pMpc}$) at $z \gtrsim 8$.

6. We present a recently-discovered Ly α emitter at $z = 8.5$ from the JADES Cycle 2 program 3215 (Eisenstein et al. 2023b). This discovery is also described in Witstok et al. (2024a). The systemic redshift is confidently determined from very strong rest-frame optical emission lines. We measure Ly α emission with EW = 17 \AA and a relatively low Ly α velocity offset $\Delta v_{\text{Ly}\alpha} = 156 \text{ km s}^{-1}$. This is one of just five robustly confirmed Ly α emitters at $z \gtrsim 8$. The small velocity offset may provide a signpost of a moderate-size bubble ($\gtrsim 0.3 \text{ pMpc}$) for the $z \approx 8.5$ Universe. In this case, we may expect numerous ionizing sources in the vicinity of the Ly α emitter. We identify 24 photometric sources at $z \approx 8.5$ within 2 arcmin from this galaxy, with two of them currently spectroscopically confirmed. Deep JWST spectroscopic follow-up of the neighboring sources will better characterize the overdensity and constrain the ionized bubble around the Ly α emitter.

ACKNOWLEDGEMENTS

The authors thank the anonymous referee for insightful comments which improved the manuscript. We would like to thank the entire FRESCO team for their effort designing and executing this program and developing their observing program with a zero-exclusive-access period. We also thank Jorryt Matthee for kindly sharing data from the X-SHOOTER Lyman α survey at $z = 2$ (XLS-z2; Matthee et al. 2021). MT acknowledges funding from the JWST Arizona/Steward Postdoc in Early galaxies and Reionization (JASPER) Scholar contract at the University of Arizona. DPS acknowledges support from the National Science Foundation through the grant AST-2109066. RSE acknowledges funding from the European Research Council (ERC) under the European Union’s Horizon 2020 research and innovation program (grant agreement No. 669253). FS acknowledges JWST/NIRCam contract to the University of Arizona NAS5-02015. BER acknowledges support from the NIRCam Science Team contract to the University of Arizona, NAS5-02015, and JWST Program 3215. SA acknowledges support from Grant PID2021-127718NB-I00 funded by the Spanish Ministry of Science and Innovation/State Agency of Research (MICIN/AEI/10.13039/501100011033). WB, RM, and JW acknowledge support from the Science and Technology Facilities Council (STFC), by the ERC through Advanced Grant 695671 “QUENCH”, by the UKRI Frontier Research grant RISE-andFALL. RM also acknowledges funding from a research professorship from the Royal Society. KB is supported by the Australian Research Council Centre of Excellence for All Sky Astrophysics in 3 Dimensions (ASTRO 3D), through project number CE170100013. AJB, JC, GCJ, and AS acknowledge funding from the “FirstGalaxies” Advanced Grant from the ERC under the European Union’s Horizon 2020 research and innovation program (grant agreement No. 789056). LW acknowledges support from the National Science Foundation Graduate Research Fellowship under Grant No. DGE-2137419. The research of CCW is supported by NOIRLab, which is managed by the Association of Universities for Research in Astronomy (AURA) under a cooperative agreement with the National Science Foundation.

This work is based in part on observations taken by the MUSE-Wide Survey and the MUSE *Hubble* Ultra Deep Field Survey as part of the MUSE Consortium. Part of the data presented in this work were obtained at Keck Observatory. The authors wish to recognize and acknowledge the very significant cultural role and reverence that the summit of Maunakea has always had within the Native Hawaiian community. We are most fortunate to have the opportunity to conduct observations from this mountain. This research is based in part on observations made with the NASA/ESA/CSA *James Webb Space Telescope* and the NASA/ESA *Hubble Space Telescope* from the Space Telescope Science Institute, which are operated by the Association of Universities for Research in Astronomy, Inc., under NASA contract NAS 5-03127 for JWST and NAS 5-26555 for HST. These observations are associated with programs # 1180, 1181, 3215, and 1895. The JWST and the HST data were obtained from the Mikulski Archive for Space Telescopes at the Space Telescope Science Institute. The authors acknowledge use of the lux supercomputer at UC Santa Cruz, funded by NSF MRI grant AST 1828315. This work is based in part upon High Performance Computing (HPC) resources supported by the University of Arizona TRIF, UITS, and Research, Innovation, and Impact (RII) and maintained by the UArizona Research Technologies department.

This research made use of the following software: NUMPY (Harris et al. 2020), MATPLOTLIB (Hunter 2007), SCIPY (Virtanen et al. 2020), ASTROPY, a community-developed core Python package for Astron-

omy (Astropy Collaboration et al. 2013), and BEAGLE (Chevallard & Charlot 2016).

DATA AVAILABILITY

The VLT/MUSE data used in this work are available from MUSE-Wide (<https://musewide.aip.de/project/>) and AMUSED (<https://amused.univ-lyon1.fr/>). The *HST* data utilized in this work are available from the *Hubble* Legacy Field archive (<https://archive.stsci.edu/prepds/hlf/>). The *JWST* data used here are available on the Mikulski Archive for Space Telescopes (<https://mast.stsci.edu/>). Other data underlying this article will be shared on reasonable request to the corresponding author.

REFERENCES

- Almada Monter S., Gronke M., 2024, *arXiv e-prints*, p. arXiv:2404.07169
- Ando M., Ohta K., Iwata I., Akiyama M., Aoki K., Tamura N., 2006, *ApJ*, **645**, L9
- Ao Y., et al., 2020, *Nature Astronomy*, **4**, 670
- Arrabal Haro P., et al., 2018, *MNRAS*, **478**, 3740
- Astropy Collaboration et al., 2013, *A&A*, **558**, A33
- Bañados E., et al., 2018, *Nature*, **553**, 473
- Bacon R., et al., 2010, in McLean I. S., Ramsay S. K., Takami H., eds, Society of Photo-Optical Instrumentation Engineers (SPIE) Conference Series Vol. 7735, Ground-based and Airborne Instrumentation for Astronomy III, p. 773508 (arXiv:2211.16795), doi:10.1117/12.856027
- Bacon R., et al., 2017, *A&A*, **608**, A1
- Bacon R., et al., 2023, *A&A*, **670**, A4
- Becker G. D., Bolton J. S., Madau P., Pettini M., Ryan-Weber E. V., Venemans B. P., 2015, *MNRAS*, **447**, 3402
- Becker G. D., D'Aloisio A., Christenson H. M., Zhu Y., Worseck G., Bolton J. S., 2021, *MNRAS*, **508**, 1853
- Beckwith S. V. W., et al., 2006, *AJ*, **132**, 1729
- Behrens C., Dijkstra M., Niemeyer J. C., 2014, *A&A*, **563**, A77
- Blaizot J., et al., 2023, *MNRAS*, **523**, 3749
- Bolan P., et al., 2022, *MNRAS*, **517**, 3263
- Bosman S. E. I., Fan X., Jiang L., Reed S., Matsuoka Y., Becker G., Haehnelt M., 2018, *MNRAS*, **479**, 1055
- Bosman S. E. I., Kakiichi K., Meyer R. A., Gronke M., Laporte N., Ellis R. S., 2020, *ApJ*, **896**, 49
- Bosman S. E. I., et al., 2022, *MNRAS*, **514**, 55
- Bouwens R. J., et al., 2009, *ApJ*, **705**, 936
- Bouwens R. J., et al., 2010a, *ApJ*, **708**, L69
- Bouwens R. J., et al., 2010b, *ApJ*, **709**, L133
- Bouwens R. J., et al., 2012, *ApJ*, **754**, 83
- Bouwens R. J., et al., 2015, *ApJ*, **803**, 34
- Bouwens R. J., et al., 2021, *AJ*, **162**, 47
- Boyett K. N. K., Stark D. P., Bunker A. J., Tang M., Masada M. V., 2022, *MNRAS*, **513**, 4451
- Boyett K., et al., 2024, *arXiv e-prints*, p. arXiv:2401.16934
- Bradač M., et al., 2017, *ApJ*, **836**, L2
- Brammer G. B., van Dokkum P. G., Coppi P., 2008, *ApJ*, **686**, 1503
- Bruzual G., Charlot S., 2003, *MNRAS*, **344**, 1000
- Bunker A. J., Stanway E. R., Ellis R. S., McMahon R. G., 2004, *MNRAS*, **355**, 374
- Bunker A. J., et al., 2010, *MNRAS*, **409**, 855
- Bunker A. J., Caruana J., Wilkins S. M., Stanway E. R., Lorenzoni S., Lacy M., Jarvis M. J., Hickey S., 2013, *MNRAS*, **430**, 3314
- Bunker A. J., et al., 2023a, *arXiv e-prints*, p. arXiv:2306.02467
- Bunker A. J., et al., 2023b, *A&A*, **677**, A88
- Bushouse H., et al., 2024, *JWST Calibration Pipeline*, doi:10.5281/zenodo.6984365
- Caffau E., Ludwig H. G., Steffen M., Freytag B., Bonifacio P., 2011, *Sol. Phys.*, **268**, 255
- Calzetti D., Kinney A. L., Storchi-Bergmann T., 1994, *ApJ*, **429**, 582
- Cameron A. J., Katz H., Witten C., Saxena A., Laporte N., Bunker A. J., 2023a, *arXiv e-prints*, p. arXiv:2311.02051
- Cameron A. J., et al., 2023b, *A&A*, **677**, A115
- Cardelli J. A., Clayton G. C., Mathis J. S., 1989, *ApJ*, **345**, 245
- Caruana J., Bunker A. J., Wilkins S. M., Stanway E. R., Lacy M., Jarvis M. J., Lorenzoni S., Hickey S., 2012, *MNRAS*, **427**, 3055
- Caruana J., Bunker A. J., Wilkins S. M., Stanway E. R., Lorenzoni S., Jarvis M. J., Ebert H., 2014, *MNRAS*, **443**, 2831
- Cassata P., et al., 2015, *A&A*, **573**, A24
- Cassata P., et al., 2020, *A&A*, **643**, A6
- Chabrier G., 2003, *PASP*, **115**, 763
- Chen Z., Stark D. P., Mason C., Topping M. W., Whitler L., Tang M., Endsley R., Charlot S., 2024, *MNRAS*, **528**, 7052
- Chevallard J., Charlot S., 2016, *MNRAS*, **462**, 1415
- Chevallard J., et al., 2018, *MNRAS*, **479**, 3264
- Chisholm J., et al., 2018, *A&A*, **616**, A30
- Chisholm J., Prochaska J. X., Schaerer D., Gazagnes S., Henry A., 2020, *MNRAS*, **498**, 2554
- Chisholm J., et al., 2022, *MNRAS*, **517**, 5104
- Choustikov N., et al., 2024a, *arXiv e-prints*, p. arXiv:2401.09557
- Choustikov N., et al., 2024b, *MNRAS*, **529**, 3751
- Cooper O. R., et al., 2023, *arXiv e-prints*, p. arXiv:2309.06656
- Curtis-Lake E., et al., 2023, *Nature Astronomy*, **7**, 622
- D'Eugenio F., et al., 2024, *arXiv e-prints*, p. arXiv:2404.06531
- D'Odorico S., et al., 2006, in McLean I. S., Iye M., eds, Society of Photo-Optical Instrumentation Engineers (SPIE) Conference Series Vol. 6269, Ground-based and Airborne Instrumentation for Astronomy, p. 626933, doi:10.1117/12.672969
- Davies F. B., et al., 2018, *ApJ*, **864**, 142
- Davis M., et al., 2007, *ApJ*, **660**, L1
- De Barros S., et al., 2017, *A&A*, **608**, A123
- De Barros S., Oesch P. A., Labbé I., Stefanon M., González V., Smit R., Bouwens R. J., Illingworth G. D., 2019, *MNRAS*, **489**, 2355
- Dijkstra M., 2014, *Publ. Astron. Soc. Australia*, **31**, e040
- Dijkstra M., 2017, *arXiv e-prints*, p. arXiv:1704.03416
- Dijkstra M., Lidz A., Wyithe J. S. B., 2007, *MNRAS*, **377**, 1175
- Dijkstra M., Mesinger A., Wyithe J. S. B., 2011, *MNRAS*, **414**, 2139
- Dijkstra M., Gronke M., Venkatesan A., 2016, *ApJ*, **828**, 71
- Du X., Shapley A. E., Tang M., Stark D. P., Martin C. L., Mobasher B., Topping M. W., Chevallard J., 2020, *ApJ*, **890**, 65
- Eilers A.-C., Davies F. B., Hennawi J. F., 2018, *ApJ*, **864**, 53
- Eisenhauer F., et al., 2003, in Iye M., Moorwood A. F. M., eds, Society of Photo-Optical Instrumentation Engineers (SPIE) Conference Series Vol. 4841, Instrument Design and Performance for Optical/Infrared Ground-based Telescopes, pp 1548–1561 (arXiv:astro-ph/0306191), doi:10.1117/12.459468
- Eisenstein D. J., et al., 2023a, *arXiv e-prints*, p. arXiv:2306.02465
- Eisenstein D. J., et al., 2023b, *arXiv e-prints*, p. arXiv:2310.12340
- Ellis R. S., et al., 2013, *ApJ*, **763**, L7
- Endsley R., Stark D. P., 2022, *MNRAS*, **511**, 6042
- Endsley R., Stark D. P., Charlot S., Chevallard J., Robertson B., Bouwens R. J., Stefanon M., 2021, *MNRAS*, **502**, 6044
- Endsley R., et al., 2022, *MNRAS*, **517**, 5642
- Endsley R., et al., 2023a, *arXiv e-prints*, p. arXiv:2306.05295
- Endsley R., Stark D. P., Whitler L., Topping M. W., Chen Z., Plat A., Chisholm J., Charlot S., 2023b, *MNRAS*, **524**, 2312
- Erb D. K., 2015, *Nature*, **523**, 169
- Erb D. K., et al., 2014, *ApJ*, **795**, 33
- Faber S. M., et al., 2003, in Iye M., Moorwood A. F. M., eds, Society of Photo-Optical Instrumentation Engineers (SPIE) Conference Series Vol. 4841, Instrument Design and Performance for Optical/Infrared Ground-based Telescopes, pp 1657–1669, doi:10.1117/12.460346
- Fabricant D., et al., 2019, *PASP*, **131**, 075004
- Fan X., Bañados E., Simcoe R. A., 2023, *ARA&A*, **61**, 373
- Ferland G. J., et al., 2013, *Rev. Mex. Astron. Astrofis.*, **49**, 137

- Ferruit P., et al., 2022, *A&A*, **661**, A81
- Finkelstein S. L., et al., 2011, *ApJ*, **729**, 140
- Fletcher T. J., Tang M., Robertson B. E., Nakajima K., Ellis R. S., Stark D. P., Inoue A., 2019, *ApJ*, **878**, 87
- Flury S. R., et al., 2022, *ApJ*, **930**, 126
- Foreman-Mackey D., Hogg D. W., Lang D., Goodman J., 2013, *PASP*, **125**, 306
- Fujimoto S., et al., 2023, *arXiv e-prints*, p. [arXiv:2308.11609](https://arxiv.org/abs/2308.11609)
- Furlanetto S. R., Zaldarriaga M., Hernquist L., 2006, *MNRAS*, **365**, 1012
- Gardner J. P., et al., 2023, *PASP*, **135**, 068001
- Garel T., Blaizot J., Rosdahl J., Michel-Dansac L., Haehnelt M. G., Katz H., Kimm T., Verhamme A., 2021, *MNRAS*, **504**, 1902
- Gazagnes S., Chisholm J., Schaerer D., Verhamme A., Izotov Y., 2020, *A&A*, **639**, A85
- Giavalisco M., et al., 2004, *ApJ*, **600**, L93
- Goovaerts I., et al., 2023, *A&A*, **678**, A174
- Goto H., et al., 2021, *ApJ*, **923**, 229
- Greene T. P., et al., 2017, *Journal of Astronomical Telescopes, Instruments, and Systems*, **3**, 035001
- Greig B., Mesinger A., Davies F. B., Wang F., Yang J., Hennawi J. F., 2022, *MNRAS*, **512**, 5390
- Gronke M., Dijkstra M., 2016, *ApJ*, **826**, 14
- Gunn J. E., Peterson B. A., 1965, *ApJ*, **142**, 1633
- Guo Y., et al., 2023, *arXiv e-prints*, p. [arXiv:2309.05513](https://arxiv.org/abs/2309.05513)
- Gutkin J., Charlot S., Bruzual G., 2016, *MNRAS*, **462**, 1757
- Hainline K. N., et al., 2024a, *ApJ*, **964**, 66
- Hainline K. N., et al., 2024b, *ApJ*, **964**, 71
- Harikane Y., Nakajima K., Ouchi M., Umeda H., Isobe Y., Ono Y., Xu Y., Zhang Y., 2024, *ApJ*, **960**, 56
- Harris C. R., et al., 2020, *Nature*, **585**, 357
- Hashimoto T., Ouchi M., Shimasaku K., Ono Y., Nakajima K., Rauch M., Lee J., Okamura S., 2013, *ApJ*, **765**, 70
- Hashimoto T., et al., 2015, *ApJ*, **812**, 157
- Hashimoto T., et al., 2019, *PASJ*, **71**, 71
- Hayes M., 2015, *Publ. Astron. Soc. Australia*, **32**, e027
- Hayes M., et al., 2010, *Nature*, **464**, 562
- Hayes M., Schaerer D., Östlin G., Mas-Hesse J. M., Atek H., Kunth D., 2011, *ApJ*, **730**, 8
- Hayes M., et al., 2013, *ApJ*, **765**, L27
- Hayes M. J., Runnholm A., Gronke M., Scarlata C., 2021, *ApJ*, **908**, 36
- Heckman T. M., Sembach K. R., Meurer G. R., Leitherer C., Calzetti D., Martin C. L., 2001, *ApJ*, **558**, 56
- Henry A., Scarlata C., Martin C. L., Erb D., 2015, *ApJ*, **809**, 19
- Henry A., Berg D. A., Scarlata C., Verhamme A., Erb D., 2018, *ApJ*, **855**, 96
- Herenz E. C., Wisotzki L., 2017, *A&A*, **602**, A111
- Herenz E. C., et al., 2017, *A&A*, **606**, A12
- Herenz E. C., et al., 2019, *A&A*, **621**, A107
- Herrero Alonso Y., Wisotzki L., Miyaji T., Schaye J., Pharo J., Krumpe M., 2023, *A&A*, **677**, A125
- Hoag A., et al., 2019, *ApJ*, **878**, 12
- Horne K., 1986, *PASP*, **98**, 609
- Hu E. M., Cowie L. L., Songaila A., Barger A. J., Rosenwasser B., Wold I. G. B., 2016, *ApJ*, **825**, L7
- Hunter J. D., 2007, *Computing in Science and Engineering*, **9**, 90
- Hutchison T. A., et al., 2019, *ApJ*, **879**, 70
- Ichikawa T., et al., 2006, in McLean I. S., Iye M., eds, *Society of Photo-Optical Instrumentation Engineers (SPIE) Conference Series Vol. 6269, Ground-based and Airborne Instrumentation for Astronomy*. p. 626916, doi:[10.1117/12.670078](https://doi.org/10.1117/12.670078)
- Illingworth G. D., et al., 2013, *ApJS*, **209**, 6
- Inami H., et al., 2017, *A&A*, **608**, A2
- Inoue A. K., Shimizu I., Iwata I., Tanaka M., 2014, *MNRAS*, **442**, 1805
- Inoue A. K., et al., 2016, *Science*, **352**, 1559
- Itoh R., et al., 2018, *ApJ*, **867**, 46
- Izotov Y. I., Stasińska G., Meynet G., Guseva N. G., Thuan T. X., 2006, *A&A*, **448**, 955
- Izotov Y. I., Schaerer D., Worseck G., Verhamme A., Guseva N. G., Thuan T. X., Orlitová I., Fricke K. J., 2020, *MNRAS*, **491**, 468
- Izotov Y. I., Worseck G., Schaerer D., Guseva N. G., Chisholm J., Thuan T. X., Fricke K. J., Verhamme A., 2021, *MNRAS*, **503**, 1734
- Izotov Y. I., Thuan T. X., Guseva N. G., Schaerer D., Worseck G., Verhamme A., 2024, *MNRAS*, **527**, 281
- Jakobsen P., et al., 2022, *A&A*, **661**, A80
- Jaskot A. E., Oey M. S., 2014, *ApJ*, **791**, L19
- Jaskot A. E., Dowd T., Oey M. S., Scarlata C., McKinney J., 2019, *ApJ*, **885**, 96
- Jones T., Stark D. P., Ellis R. S., 2012, *ApJ*, **751**, 51
- Jones G. C., et al., 2024, *A&A*, **683**, A238
- Jung I., et al., 2018, *ApJ*, **864**, 103
- Jung I., et al., 2022, *arXiv e-prints*, p. [arXiv:2212.09850](https://arxiv.org/abs/2212.09850)
- Jung I., et al., 2023, *arXiv e-prints*, p. [arXiv:2304.05385](https://arxiv.org/abs/2304.05385)
- Kakiichi K., Gronke M., 2021, *ApJ*, **908**, 30
- Kim K. J., et al., 2023, *ApJ*, **955**, L17
- Kimm T., Blaizot J., Garel T., Michel-Dansac L., Katz H., Rosdahl J., Verhamme A., Haehnelt M., 2019, *MNRAS*, **486**, 2215
- Konno A., et al., 2018, *PASJ*, **70**, S16
- Kornei K. A., Shapley A. E., Erb D. K., Steidel C. C., Reddy N. A., Pettini M., Bogosavljević M., 2010, *ApJ*, **711**, 693
- Kron R. G., 1980, *ApJS*, **43**, 305
- Kusakabe H., et al., 2020, *A&A*, **638**, A12
- Labbé I., et al., 2013, *ApJ*, **777**, L19
- Laporte N., Nakajima K., Ellis R. S., Zitrin A., Stark D. P., Mainali R., Roberts-Borsani G. W., 2017, *ApJ*, **851**, 40
- Laporte N., Meyer R. A., Ellis R. S., Robertson B. E., Chisholm J., Roberts-Borsani G. W., 2021, *MNRAS*, **505**, 3336
- Larson R. L., et al., 2022, *ApJ*, **930**, 104
- Larson R. L., et al., 2023, *ApJ*, **953**, L29
- Laursen P., Sommer-Larsen J., Razoumov A. O., 2011, *ApJ*, **728**, 52
- Leclercq F., et al., 2017, *A&A*, **608**, A8
- Leclercq F., et al., 2020, *A&A*, **635**, A82
- Lehnert M. D., et al., 2010, *Nature*, **467**, 940
- Leonova E., et al., 2022, *MNRAS*, **515**, 5790
- Li Z., Gronke M., 2022, *MNRAS*, **513**, 5034
- Li Z., Steidel C. C., Gronke M., Chen Y., Matsuda Y., 2022, *MNRAS*, **513**, 3414
- Lin X., et al., 2024, *arXiv e-prints*, p. [arXiv:2401.09532](https://arxiv.org/abs/2401.09532)
- Lu T.-Y., Mason C. A., Hutter A., Mesinger A., Qin Y., Stark D. P., Endsley R., 2024, *MNRAS*, **528**, 4872
- Lyu J., et al., 2024, *ApJ*, **966**, 229
- Ma X., Quataert E., Wetzel A., Hopkins P. F., Faucher-Giguère C.-A., Kereš D., 2020, *MNRAS*, **498**, 2001
- Madau P., 1995, *ApJ*, **441**, 18
- Mainali R., Kollmeier J. A., Stark D. P., Simcoe R. A., Walth G., Newman A. B., Miller D. R., 2017, *ApJ*, **836**, L14
- Maiolino R., et al., 2015, *MNRAS*, **452**, 54
- Maiolino R., et al., 2023, *arXiv e-prints*, p. [arXiv:2308.01230](https://arxiv.org/abs/2308.01230)
- Mary D., Bacon R., Conseil S., Piqueras L., Schutz A., 2020, *A&A*, **635**, A194
- Maseda M. V., et al., 2020, *MNRAS*, **493**, 5120
- Maseda M. V., et al., 2023, *ApJ*, **956**, 11
- Mason C. A., Gronke M., 2020, *MNRAS*, **499**, 1395
- Mason C. A., Treu T., Dijkstra M., Mesinger A., Trenti M., Pentericci L., de Barros S., Vanzella E., 2018a, *ApJ*, **856**, 2
- Mason C. A., et al., 2018b, *ApJ*, **857**, L11
- Mason C. A., et al., 2019, *MNRAS*, **485**, 3947
- Matsuda Y., et al., 2012, *MNRAS*, **425**, 878
- Matthee J., Sobral D., Oteo I., Best P., Smail I., Röttgering H., Paulino-Afonso A., 2016, *MNRAS*, **458**, 449
- Matthee J., Sobral D., Gronke M., Paulino-Afonso A., Stefanon M., Röttgering H., 2018, *A&A*, **619**, A136
- Matthee J., Sobral D., Gronke M., Pezzulli G., Cantalupo S., Röttgering H., Darvish B., Santos S., 2020, *MNRAS*, **492**, 1778
- Matthee J., et al., 2021, *MNRAS*, **505**, 1382
- Matthee J., Mackenzie R., Simcoe R. A., Kashino D., Lilly S. J., Bordoloi R., Eilers A.-C., 2023, *ApJ*, **950**, 67
- Matthee J., et al., 2024, *ApJ*, **963**, 129

- McLinden E. M., et al., 2011, *ApJ*, **730**, 136
- McLinden E. M., Rhoads J. E., Malhotra S., Finkelstein S. L., Richardson M. L. A., Smith B., Tilvi V. S., 2014, *MNRAS*, **439**, 446
- McLure R. J., Dunlop J. S., Cirasuolo M., Koekemoer A. M., Sabbi E., Stark D. P., Targett T. A., Ellis R. S., 2010, *MNRAS*, **403**, 960
- Mesinger A., Aykatalp A., Vanzella E., Pentericci L., Ferrara A., Dijkstra M., 2015, *MNRAS*, **446**, 566
- Meurer G. R., Heckman T. M., Calzetti D., 1999, *ApJ*, **521**, 64
- Meyer R. A., Laporte N., Ellis R. S., Verhamme A., Garel T., 2021, *MNRAS*, **500**, 558
- Miralda-Escudé J., 1998, *ApJ*, **501**, 15
- Mitchell P. D., Blaizot J., Cadiou C., Dubois Y., Garel T., Rosdahl J., 2021, *MNRAS*, **501**, 5757
- Momose R., et al., 2014, *MNRAS*, **442**, 110
- Morales A. M., Mason C. A., Bruton S., Gronke M., Haardt F., Scarlata C., 2021, *ApJ*, **919**, 120
- Naidu R. P., et al., 2017, *ApJ*, **847**, 12
- Naidu R. P., Tacchella S., Mason C. A., Bose S., Oesch P. A., Conroy C., 2020, *ApJ*, **892**, 109
- Naidu R. P., et al., 2022, *MNRAS*, **510**, 4582
- Nakajima K., Ouchi M., Isobe Y., Harikane Y., Zhang Y., Ono Y., Umeda H., Oguri M., 2023, *ApJS*, **269**, 33
- Nakane M., et al., 2024, *ApJ*, **967**, 28
- Oesch P. A., et al., 2015, *ApJ*, **804**, L30
- Oesch P. A., et al., 2023, *MNRAS*, **525**, 2864
- Oke J. B., Gunn J. E., 1983, *ApJ*, **266**, 713
- Ono Y., Ouchi M., Shimasaku K., Dunlop J., Farrah D., McLure R., Okamura S., 2010, *ApJ*, **724**, 1524
- Ono Y., et al., 2012, *ApJ*, **744**, 83
- Osterbrock D. E., Ferland G. J., 2006, *Astrophysics of gaseous nebulae and active galactic nuclei*
- Ota K., et al., 2017, *ApJ*, **844**, 85
- Ouchi M., et al., 2010, *ApJ*, **723**, 869
- Ouchi M., Ono Y., Shibuya T., 2020, *ARA&A*, **58**, 617
- Pahl A. J., Shapley A. E., Steidel C. C., Reddy N. A., Chen Y., Rudie G. C., Strom A. L., 2023, *MNRAS*, **521**, 3247
- Pahl A. J., Shapley A. E., Steidel C. C., Reddy N. A., Chen Y., Rudie G. C., 2024, *arXiv e-prints*, p. [arXiv:2401.09526](https://arxiv.org/abs/2401.09526)
- Pei Y. C., 1992, *ApJ*, **395**, 130
- Pentericci L., et al., 2016, *ApJ*, **829**, L11
- Pentericci L., et al., 2018, *A&A*, **619**, A147
- Perrin M. D., Sivaramakrishnan A., Lajoie C.-P., Elliott E., Pueyo L., Ravindranath S., Albert L., 2014, in Oschmann Jacobus M. J., Clampin M., Fazio G. G., MacEwen H. A., eds, *Society of Photo-Optical Instrumentation Engineers (SPIE) Conference Series Vol. 9143, Space Telescopes and Instrumentation 2014: Optical, Infrared, and Millimeter Wave*. p. 91433X, [doi:10.1117/12.2056689](https://doi.org/10.1117/12.2056689)
- Planck Collaboration et al., 2020, *A&A*, **641**, A6
- Prieto-Lyon G., et al., 2023, *ApJ*, **956**, 136
- Raiter A., Schaerer D., Fosbury R. A. E., 2010, *A&A*, **523**, A64
- Reddy N. A., Steidel C. C., 2009, *ApJ*, **692**, 778
- Reddy N. A., Steidel C. C., Pettini M., Bogosavljević M., Shapley A. E., 2016, *ApJ*, **828**, 108
- Rieke M. J., et al., 2023a, *PASP*, **135**, 028001
- Rieke M. J., et al., 2023b, *ApJS*, **269**, 16
- Rinaldi P., et al., 2023, *ApJ*, **952**, 143
- Rivera-Thorsen T. E., et al., 2017, *A&A*, **608**, L4
- Roberts-Borsani G. W., et al., 2016, *ApJ*, **823**, 143
- Roberts-Borsani G. W., Ellis R. S., Laporte N., 2020, *MNRAS*, **497**, 3440
- Robertson B. E., 2022, *ARA&A*, **60**, 121
- Robertson B. E., Ellis R. S., Dunlop J. S., McLure R. J., Stark D. P., 2010, *Nature*, **468**, 49
- Robertson B. E., et al., 2023, *Nature Astronomy*,
- Roy N., et al., 2023, *ApJ*, **952**, L14
- Ryabchikova T., Piskunov N., Kurucz R. L., Stempels H. C., Heiter U., Pakhomov Y., Barklem P. S., 2015, *Phys. Scr.*, **90**, 054005
- Saldana-Lopez A., et al., 2022, *A&A*, **663**, A59
- Salmon B., et al., 2015, *ApJ*, **799**, 183
- Sanders R. L., et al., 2016, *ApJ*, **816**, 23
- Sanders R. L., Shapley A. E., Topping M. W., Reddy N. A., Brammer G. B., 2023, *ApJ*, **955**, 54
- Sanders R. L., Shapley A. E., Topping M. W., Reddy N. A., Brammer G. B., 2024, *ApJ*, **962**, 24
- Santos M. R., 2004, *MNRAS*, **349**, 1137
- Santos S., Sobral D., Matthee J., 2016, *MNRAS*, **463**, 1678
- Saxena A., et al., 2023, *A&A*, **678**, A68
- Saxena A., et al., 2024, *A&A*, **684**, A84
- Schenker M. A., Ellis R. S., Konidaris N. P., Stark D. P., 2014, *ApJ*, **795**, 20
- Shapley A. E., Steidel C. C., Pettini M., Adelberger K. L., 2003, *ApJ*, **588**, 65
- Shapley A. E., Reddy N. A., Sanders R. L., Topping M. W., Brammer G. B., 2023, *ApJ*, **950**, L1
- Shibuya T., et al., 2014, *ApJ*, **788**, 74
- Simmonds C., et al., 2023, *MNRAS*, **523**, 5468
- Simmonds C., et al., 2024, *MNRAS*, **527**, 6139
- Songaila A., Hu E. M., Barger A. J., Cowie L. L., Hasinger G., Rosenwasser B., Waters C., 2018, *ApJ*, **859**, 91
- Stanway E. R., Bremer M. N., Lehnert M. D., 2008, *MNRAS*, **385**, 493
- Stark D. P., 2016, *ARA&A*, **54**, 761
- Stark D. P., Ellis R. S., Bunker A., Bundy K., Targett T., Benson A., Lacy M., 2009, *ApJ*, **697**, 1493
- Stark D. P., Ellis R. S., Chiu K., Ouchi M., Bunker A., 2010, *MNRAS*, **408**, 1628
- Stark D. P., Ellis R. S., Ouchi M., 2011, *ApJ*, **728**, L2
- Stark D. P., et al., 2015, *MNRAS*, **450**, 1846
- Stark D. P., et al., 2017, *MNRAS*, **464**, 469
- Steidel C. C., Strom A. L., Pettini M., Rudie G. C., Reddy N. A., Trainor R. F., 2016, *ApJ*, **826**, 159
- Steidel C. C., Bogosavljević M., Shapley A. E., Reddy N. A., Rudie G. C., Pettini M., Trainor R. F., Strom A. L., 2018, *ApJ*, **869**, 123
- Tacchella S., et al., 2022, *ApJ*, **927**, 170
- Tacchella S., et al., 2023a, *MNRAS*, **522**, 6236
- Tacchella S., et al., 2023b, *ApJ*, **952**, 74
- Tang M., Stark D. P., Chevallard J., Charlot S., 2019, *MNRAS*, **489**, 2572
- Tang M., Stark D. P., Chevallard J., Charlot S., Endsley R., Congiu E., 2021, *MNRAS*, **503**, 4105
- Tang M., Stark D. P., Ellis R. S., 2022, *MNRAS*, **513**, 5211
- Tang M., et al., 2023, *MNRAS*, **526**, 1657
- Tang M., Stark D. P., Ellis R. S., Topping M. W., Mason C., Li Z., Plat A., 2024, *arXiv e-prints*, p. [arXiv:2404.06569](https://arxiv.org/abs/2404.06569)
- Tilvi V., et al., 2020, *ApJ*, **891**, L10
- Topping M. W., Stark D. P., Endsley R., Plat A., Whittler L., Chen Z., Charlot S., 2022, *ApJ*, **941**, 153
- Topping M. W., et al., 2024, *MNRAS*, **529**, 4087
- Torralba-Torregrosa A., et al., 2024, *arXiv e-prints*, p. [arXiv:2404.10040](https://arxiv.org/abs/2404.10040)
- Trebtsch M., Verhamme A., Blaizot J., Rosdahl J., 2016, *A&A*, **593**, A122
- Treu T., Schmidt K. B., Trenti M., Bradley L. D., Stiavelli M., 2013, *ApJ*, **775**, L29
- Umeda H., Ouchi M., Nakajima K., Harikane Y., Ono Y., Xu Y., Isobe Y., Zhang Y., 2023, *arXiv e-prints*, p. [arXiv:2306.00487](https://arxiv.org/abs/2306.00487)
- Urrutia T., et al., 2019, *A&A*, **624**, A141
- Vanzella E., et al., 2009, *ApJ*, **695**, 1163
- Vanzella E., et al., 2018, *MNRAS*, **476**, L15
- Verhamme A., Schaerer D., Maselli A., 2006, *A&A*, **460**, 397
- Verhamme A., Schaerer D., Atek H., Tapken C., 2008, *A&A*, **491**, 89
- Verhamme A., Orlitová I., Schaerer D., Hayes M., 2015, *A&A*, **578**, A7
- Virtanen P., et al., 2020, *Nature Methods*, **17**, 261
- Wang F., et al., 2020, *ApJ*, **896**, 23
- Whitaker K. E., et al., 2019, *ApJS*, **244**, 16
- Whittler L. R., Mason C. A., Ren K., Dijkstra M., Mesinger A., Pentericci L., Trenti M., Treu T., 2020, *MNRAS*, **495**, 3602
- Whittler L., Stark D. P., Endsley R., Leja J., Charlot S., Chevallard J., 2023, *MNRAS*,
- Whittler L., Stark D. P., Endsley R., Chen Z., Mason C., Topping M. W., Charlot S., 2024, *MNRAS*, **529**, 855
- Willott C. J., Carilli C. L., Wagg J., Wang R., 2015, *ApJ*, **807**, 180
- Wisotzki L., et al., 2016, *A&A*, **587**, A98

- Witstok J., et al., 2024a, [arXiv e-prints](#), p. [arXiv:2404.05724](#)
Witstok J., et al., 2024b, [A&A](#), 682, A40
Worseck G., et al., 2014, [MNRAS](#), 445, 1745
Wu J., Jiang L., Ning Y., 2020, [ApJ](#), 891, 105
Wyithe J. S. B., Loeb A., 2005, [ApJ](#), 625, 1
Xu X., et al., 2022, [ApJ](#), 933, 202
Xu X., et al., 2023, [ApJ](#), 943, 94
Yang H., et al., 2017, [ApJ](#), 844, 171
Yang J., et al., 2020a, [ApJ](#), 897, L14
Yang J., et al., 2020b, [ApJ](#), 904, 26
Zhang H., et al., 2024, [ApJ](#), 961, 63
Zheng Z.-Y., et al., 2017, [ApJ](#), 842, L22
Zhu Y., et al., 2023, [ApJ](#), 955, 115
Zitrin A., et al., 2015, [ApJ](#), 810, L12
de Graaff A., et al., 2024, [A&A](#), 684, A87
de La Vieuville G., et al., 2020, [A&A](#), 644, A39

APPENDIX A: TABLES OF GALAXIES WITH $\text{Ly}\alpha$ AND $\text{H}\alpha$ DETECTIONS AT $z \simeq 5 - 6$

This paper has been typeset from a $\text{\TeX}/\text{\LaTeX}$ file prepared by the author.

ID	R.A. (deg)	Decl. (deg)	M_{UV} (mag)	$z_{Ly\alpha}$	$F_{Ly\alpha}$ (10^{-20} erg s $^{-1}$ cm $^{-2}$)	$EW_{Ly\alpha}$ (Å)	$\Delta v_{Ly\alpha}$ (km s $^{-1}$)	$f_{esc, Ly\alpha}^{case B}$	$f_{esc, Ly\alpha}^{case A}$
MUSE-102049176	53.074469	-27.820237	-18.05 ± 0.10	5.1024	2126 ± 262	395 ± 60	179 ± 110	0.760 ± 0.393	0.580 ± 0.300
MUSE-107041159	53.087996	-27.813147	-19.25 ± 0.04	5.3161	4896 ± 269	333 ± 22	73 ± 19	0.847 ± 0.172	0.647 ± 0.131
MUSE-116039142	53.131702	-27.847032	-19.52 ± 0.06	5.3253	2849 ± 206	151 ± 13	85 ± 30	0.829 ± 0.211	0.633 ± 0.161
MUSE-117039091	53.156207	-27.836079	-18.68 ± 0.09	5.7675	1790 ± 178	248 ± 32	115 ± 35	0.678 ± 0.168	0.518 ± 0.128
MUSE-118034094	53.175266	-27.841127	-19.63 ± 0.08	5.2964	4217 ± 308	199 ± 20	86 ± 17	0.783 ± 0.172	0.598 ± 0.131
MUSE-119036075	53.188854	-27.833476	-18.39 ± 0.27	5.3345	1026 ± 139	154 ± 43	251 ± 17	0.413 ± 0.120	0.315 ± 0.092
MUSE-119039078	53.177428	-27.830966	-18.21 ± 0.07	5.6132	1176 ± 123	237 ± 29	77 ± 58	0.494 ± 0.185	0.377 ± 0.141
MUSE-119040079	53.191824	-27.824896	-19.88 ± 0.04	5.7880	2161 ± 244	100 ± 11	261 ± 31	0.383 ± 0.082	0.292 ± 0.063
MUSE-122002035	53.119796	-27.831269	-17.96 ± 0.32	5.3180	1354 ± 141	302 ± 94	163 ± 53	1.470 ± 0.997	1.122 ± 0.761
MUSE-123027133	53.144620	-27.831002	-18.34 ± 0.08	5.8024	1548 ± 141	298 ± 35	79 ± 37	0.766 ± 0.345	0.584 ± 0.263
MUSE-124033068	53.165978	-27.823859	-18.73 ± 0.06	5.0475	2480 ± 224	240 ± 25	119 ± 28	0.778 ± 0.234	0.594 ± 0.178
MUSE-125051124	53.188380	-27.819461	-20.11 ± 0.02	5.5815	2712 ± 628	93 ± 21	310 ± 52	0.309 ± 0.092	0.236 ± 0.070
MUSE-125052125	53.173472	-27.825016	-17.94 ± 0.06	5.6134	900 ± 240	232 ± 63	140 ± 49	0.598 ± 0.353	0.457 ± 0.270
MUSE-128044246	53.121016	-27.815916	-18.33 ± 0.09	4.9347	2444 ± 428	326 ± 63	60 ± 70	1.086 ± 0.664	0.828 ± 0.507
MUSE-128045247	53.119796	-27.821988	-19.32 ± 0.06	4.9666	3064 ± 500	166 ± 28	193 ± 51	1.387 ± 0.448	1.059 ± 0.342
MUSE-130033059	53.102725	-27.792042	-19.02 ± 0.15	5.1138	1494 ± 348	113 ± 30	326 ± 17	0.253 ± 0.072	0.193 ± 0.055
MUSE-131016106	53.104145	-27.783718	-19.28 ± 0.09	6.0641	2196 ± 428	197 ± 41	273 ± 41	0.998 ± 0.489	0.762 ± 0.373
MUSE-134036056	53.131273	-27.806806	-19.72 ± 0.03	5.1251	4024 ± 489	162 ± 20	113 ± 26	0.935 ± 0.219	0.713 ± 0.167
MUSE-134037057	53.132663	-27.798961	-18.40 ± 0.11	5.1302	3906 ± 407	533 ± 77	201 ± 26	0.599 ± 0.123	0.457 ± 0.094
MUSE-135049239	53.124788	-27.784118	-19.05 ± 0.08	5.7854	2252 ± 261	223 ± 30	147 ± 25	0.511 ± 0.149	0.390 ± 0.114
MUSE-136041192	53.115275	-27.772786	-18.49 ± 0.16	5.0806	2014 ± 291	246 ± 50	234 ± 24	0.293 ± 0.073	0.224 ± 0.056
MUSE-136044198	53.123258	-27.771197	-19.17 ± 0.11	5.2338	3847 ± 429	270 ± 40	111 ± 30	0.518 ± 0.093	0.395 ± 0.071
MUSE-139047301	53.142900	-27.758885	-18.14 ± 0.06	4.9374	963 ± 196	153 ± 32	177 ± 46	0.486 ± 0.298	0.371 ± 0.227
MUSE-140047114	53.134580	-27.756489	-20.16 ± 0.06	5.4481	3478 ± 447	108 ± 15	135 ± 16	0.539 ± 0.099	0.411 ± 0.076
MUSE-68	53.171196	-27.778448	-19.86 ± 0.04	4.9397	4855 ± 26	158 ± 5	258 ± 96	0.692 ± 0.332	0.528 ± 0.254
MUSE-313	53.170944	-27.782429	-17.68 ± 0.17	5.1382	530 ± 6	140 ± 22	186 ± 34	0.323 ± 0.199	0.247 ± 0.152
MUSE-417	53.157867	-27.779982	-18.01 ± 0.07	5.1321	224 ± 10	43 ± 3	156 ± 63	0.118 ± 0.056	0.090 ± 0.042
MUSE-547	53.160609	-27.771537	-18.42 ± 0.09	5.9775	581 ± 30	111 ± 10	236 ± 77	0.289 ± 0.085	0.221 ± 0.065
MUSE-1478	53.153168	-27.766165	-20.14 ± 0.04	4.9304	932 ± 48	23 ± 1	263 ± 66	0.096 ± 0.035	0.073 ± 0.027
MUSE-1670	53.166702	-27.804155	-21.30 ± 0.01	5.8325	2348 ± 112	29 ± 1	470 ± 15	0.079 ± 0.007	0.061 ± 0.005
MUSE-2069	53.151096	-27.782923	-19.39 ± 0.03	5.2678	536 ± 56	31 ± 3	249 ± 21	0.165 ± 0.047	0.126 ± 0.036
MUSE-2071	53.146133	-27.777782	-18.84 ± 0.05	4.9304	368 ± 32	30 ± 3	263 ± 203	0.102 ± 0.209	0.078 ± 0.159
MUSE-2168	53.135960	-27.798378	-18.95 ± 0.04	5.7811	1473 ± 49	159 ± 7	186 ± 26	0.263 ± 0.066	0.201 ± 0.050
MUSE-2296	53.168419	-27.804079	-18.64 ± 0.08	4.9500	488 ± 55	49 ± 6	227 ± 27	0.233 ± 0.095	0.178 ± 0.072
MUSE-2302	53.180447	-27.770603	-17.73 ± 0.08	5.0333	370 ± 38	89 ± 11	318 ± 90	0.152 ± 0.082	0.116 ± 0.063
MUSE-2307	53.183330	-27.795965	-17.86 ± 0.06	4.9489	1276 ± 50	263 ± 17	161 ± 30	0.373 ± 0.136	0.285 ± 0.104
MUSE-2350	53.156380	-27.809574	-18.16 ± 0.05	5.0488	1392 ± 49	227 ± 13	119 ± 20	0.595 ± 0.169	0.454 ± 0.129
MUSE-2449	53.164741	-27.769613	-18.71 ± 0.13	5.2709	363 ± 61	39 ± 8	62 ± 39	0.231 ± 0.117	0.176 ± 0.089
MUSE-2481	53.149803	-27.810652	-18.76 ± 0.05	5.0323	254 ± 47	23 ± 4	219 ± 108	0.111 ± 0.067	0.085 ± 0.051
MUSE-2502	53.158028	-27.817951	-19.24 ± 0.04	5.6411	655 ± 39	51 ± 3	330 ± 20	0.178 ± 0.039	0.136 ± 0.029
MUSE-2873	53.172489	-27.764322	-17.93 ± 0.09	5.0508	487 ± 32	98 ± 10	188 ± 40	0.258 ± 0.114	0.197 ± 0.087
MUSE-2964	53.149456	-27.809727	-17.85 ± 0.06	5.0591	313 ± 44	68 ± 10	253 ± 45	0.416 ± 0.306	0.318 ± 0.233
MUSE-3090	53.155037	-27.762585	-18.16 ± 0.10	5.1362	165 ± 27	28 ± 5	235 ± 46	0.155 ± 0.085	0.118 ± 0.065
MUSE-3093	53.139675	-27.796425	-17.69 ± 0.08	5.0518	339 ± 24	85 ± 8	154 ± 35	0.161 ± 0.081	0.123 ± 0.062
MUSE-3203	53.176548	-27.771025	-18.79 ± 0.05	5.8921	1405 ± 60	184 ± 11	91 ± 43	0.610 ± 0.274	0.465 ± 0.209
MUSE-3238	53.175571	-27.795835	-18.12 ± 0.16	5.6185	721 ± 43	158 ± 25	136 ± 41	0.234 ± 0.091	0.179 ± 0.069
MUSE-4405	53.170544	-27.812431	-18.77 ± 0.08	5.8376	419 ± 49	55 ± 7	285 ± 49	0.133 ± 0.060	0.102 ± 0.046
MUSE-6231	53.178307	-27.800921	-18.96 ± 0.04	6.3313	495 ± 94	66 ± 12	360 ± 49	0.147 ± 0.081	0.112 ± 0.062
MUSE-6294	53.166091	-27.785667	-19.56 ± 0.11	5.4715	697 ± 23	38 ± 4	130 ± 10	0.088 ± 0.013	0.067 ± 0.010
MUSE-6462	53.164040	-27.799646	-20.23 ± 0.04	5.4530	819 ± 55	23 ± 1	335 ± 16	0.061 ± 0.009	0.046 ± 0.007
MUSE-7125	53.128100	-27.789826	-19.31 ± 0.06	5.0313	216 ± 38	12 ± 2	295 ± 62	0.082 ± 0.038	0.063 ± 0.029
MUSE-7205	53.162998	-27.760258	-17.86 ± 0.10	4.9222	286 ± 30	58 ± 8	147 ± 138	0.075 ± 0.056	0.057 ± 0.043
MUSE-7225	53.161663	-27.763103	-18.81 ± 0.03	5.5589	557 ± 49	63 ± 5	215 ± 23	0.192 ± 0.054	0.147 ± 0.041
MUSE-7319	53.186211	-27.787121	-17.93 ± 0.15	5.1444	324 ± 54	68 ± 14	210 ± 60	0.249 ± 0.268	0.190 ± 0.204
MUSE-7337	53.169041	-27.787611	-17.93 ± 0.08	5.4715	193 ± 15	47 ± 5	222 ± 111	0.038 ± 0.017	0.029 ± 0.013
MUSE-7605	53.165718	-27.784885	-18.09 ± 0.08	5.4725	1096 ± 24	230 ± 17	278 ± 83	0.392 ± 0.160	0.299 ± 0.122
MUSE-7922	53.180718	-27.776484	-17.19 ± 0.52	5.3851	235 ± 45	109 ± 56	216 ± 40	0.303 ± 0.159	0.231 ± 0.121

Table A1. Information and Ly α properties of the 79 galaxies with both Ly α and H α detections at $4.9 < z < 6.5$ in our sample. We provide the Ly α fluxes measured from VLT/MUSE and Keck/DEIMOS spectra. For galaxies with DEIMOS observations, we first list the Ly α fluxes converted to MUSE aperture values in order to be consistent with MUSE measurements (Section 2.2), and then the original Ly α fluxes measured from DEIMOS spectra in parentheses. Converting from MUSE measured Ly α fluxes to *JWST*/NIRSpec MSA measurements is to multiply MUSE fluxes by a factor of $\simeq 0.8$ (Section 2.2). The Ly α velocity offset ($\Delta v_{Ly\alpha}$) is calculated using the redshift measured from Ly α emission lines ($z_{Ly\alpha}$) and the systemic redshift measured from H α emission lines (Section 2.4, see also Sun et al. in prep.). Note that the Ly α velocity offset measurement is also subject to an uncertainty of NIRCcam grism wavelength calibration ($\simeq 100$ km s $^{-1}$). We compute the Ly α escape fraction for both case B ($f_{esc, Ly\alpha}^{case B}$) and case A recombination ($f_{esc, Ly\alpha}^{case A}$).

ID	R.A. (deg)	Decl. (deg)	M _{UV} (mag)	$z_{Ly\alpha}$	$F_{Ly\alpha}$ (10^{-20} erg s $^{-1}$ cm $^{-2}$)	EW _{Lyα} (Å)	$\Delta v_{Ly\alpha}$ (km s $^{-1}$)	$f_{esc, Ly\alpha}^{case B}$	$f_{esc, Ly\alpha}^{case A}$
MUSE-7934	53.146606	-27.786125	-19.77 ± 0.03	5.5270	348 ± 41	16 ± 1	133 ± 55	0.111 ± 0.048	0.085 ± 0.037
MUSE-7984	53.179279	-27.773256	-18.88 ± 0.03	6.1071	320 ± 53	42 ± 7	232 ± 26	0.090 ± 0.031	0.069 ± 0.024
MUSE-8124	53.156754	-27.809155	-19.54 ± 0.04	5.5887	867 ± 52	50 ± 3	100 ± 45	0.503 ± 0.241	0.384 ± 0.184
DEIMOS-43_7167	189.085312	62.212612	-19.66 ± 0.08	4.9196	2379 ± 68 (1830)	92 ± 7	238 ± 54	0.232 ± 0.045	0.177 ± 0.034
DEIMOS-42_11827	189.143036	62.166759	-18.49 ± 0.18	4.9265	1674 ± 55 (1288)	190 ± 32	250 ± 64	0.170 ± 0.045	0.130 ± 0.034
DEIMOS-23_31399	189.362015	62.249187	-19.60 ± 0.10	5.0503	739 ± 63 (568)	32 ± 4	429 ± 63	0.228 ± 0.127	0.174 ± 0.097
DEIMOS-25458	189.272995	62.267040	-18.43 ± 0.23	5.2012	1548 ± 89 (1191)	212 ± 46	160 ± 52	0.378 ± 0.094	0.289 ± 0.071
DEIMOS-25824	189.301392	62.268780	-20.69 ± 0.06	5.2393	623 ± 125 (479)	10 ± 2	725 ± 56	0.149 ± 0.052	0.114 ± 0.040
DEIMOS-11505	189.265076	62.199612	-18.77 ± 0.10	5.2260	2007 ± 121 (1544)	203 ± 22	233 ± 75	0.364 ± 0.226	0.277 ± 0.172
DEIMOS-19842	189.363861	62.239918	-19.32 ± 0.09	5.2611	462 ± 151 (356)	28 ± 9	385 ± 55	0.135 ± 0.058	0.103 ± 0.044
DEIMOS-43_13063	189.156342	62.210011	-19.92 ± 0.05	5.1895	358 ± 97 (275)	12 ± 3	351 ± 49	0.052 ± 0.015	0.040 ± 0.012
DEIMOS-33_19970	189.230789	62.263546	-19.56 ± 0.05	5.1950	395 ± 92 (304)	19 ± 4	169 ± 54	0.055 ± 0.015	0.042 ± 0.012
DEIMOS-42_9127	189.110382	62.202064	-19.70 ± 0.10	5.2022	394 ± 58 (303)	16 ± 2	297 ± 56	0.040 ± 0.009	0.031 ± 0.007
DEIMOS-33_20014	189.231232	62.259106	-20.14 ± 0.06	5.1937	2923 ± 111 (2249)	82 ± 5	242 ± 49	0.078 ± 0.004	0.060 ± 0.003
DEIMOS-33_17440	189.205124	62.260712	-21.05 ± 0.03	5.1947	4586 ± 77 (3528)	56 ± 1	237 ± 49	0.229 ± 0.016	0.175 ± 0.012
DEIMOS-vdrop_225	189.183884	62.179928	-18.70 ± 0.08	5.2378	1371 ± 112 (1055)	148 ± 16	286 ± 56	0.932 ± 0.482	0.712 ± 0.368
DEIMOS-vdrop_375	189.285294	62.251411	-19.40 ± 0.08	5.2834	1301 ± 71 (1001)	75 ± 6	408 ± 49	0.253 ± 0.045	0.193 ± 0.034
DEIMOS-33_17034	189.200592	62.259441	-20.02 ± 0.05	5.6068	3081 ± 149 (2370)	116 ± 7	232 ± 47	0.354 ± 0.051	0.270 ± 0.039
DEIMOS-42_11693	189.141540	62.190292	-19.84 ± 0.30	5.6129	2368 ± 77 (1822)	106 ± 29	342 ± 46	0.162 ± 0.015	0.124 ± 0.012
DEIMOS-vdrop_167	189.142960	62.196960	-19.13 ± 0.60	5.6149	953 ± 86 (733)	82 ± 46	210 ± 48	1.097 ± 0.488	0.837 ± 0.373
DEIMOS-33_17705	189.208191	62.232136	-19.63 ± 0.05	5.8061	650 ± 41 (500)	38 ± 3	589 ± 83	0.092 ± 0.033	0.070 ± 0.025
DEIMOS-32_16773	189.197845	62.199963	-19.11 ± 0.06	5.9752	525 ± 38 (404)	53 ± 4	242 ± 48	0.103 ± 0.032	0.078 ± 0.024

Table A1. Continued.

ID	JADES ID	$\log(M_{\star}/M_{\odot})$	$\log(\text{age}/\text{yr})$	$A(H\alpha)$ (mag)	[O III]+H β EW (Å)	$\log(\xi_{\text{ion}}/\text{erg}^{-1} \text{ Hz})$
MUSE-102049176	JADES-GS+53.07450-27.82028	7.28 ^{+0.08} _{-0.07}	6.24 ^{+0.17} _{-0.16}	0.005 ^{+0.009} _{-0.003}	5206 ⁺⁶²² ₋₅₉₈	25.91 ^{+0.10} _{-0.08}
MUSE-107041159	JADES-GS+53.08803-27.81320	8.26 ^{+0.41} _{-0.32}	7.76 ^{+0.52} _{-0.41}	0.019 ^{+0.032} _{-0.019}	610 ⁺²⁹² ₋₃₀₁	25.36 ^{+0.09} _{-0.08}
MUSE-116039142	JADES-GS+53.13174-27.84712	8.79 ^{+0.13} _{-0.22}	8.42 ^{+0.18} _{-0.27}	0.003 ^{+0.007} _{-0.002}	252 ⁺¹⁴⁴ ₋₈₀	25.45 ^{+0.07} _{-0.07}
MUSE-117039091	JADES-GS+53.15625-27.83617	7.44 ^{+0.08} _{-0.07}	7.05 ^{+0.09} _{-0.10}	0.003 ^{+0.008} _{-0.002}	1496 ⁺¹⁰⁰ ₋₁₀₀	25.57 ^{+0.05} _{-0.05}
MUSE-118034094	JADES-GS+53.17529-27.84117	7.81 ^{+0.05} _{-0.03}	6.64 ^{+0.09} _{-0.06}	0.054 ^{+0.014} _{-0.012}	2096 ⁺⁵⁶⁰ ₋₄₃₄	25.81 ^{+0.10} _{-0.22}
MUSE-119039078	JADES-GS+53.17747-27.83105	7.29 ^{+0.08} _{-0.09}	7.12 ^{+0.10} _{-0.10}	0.003 ^{+0.004} _{-0.001}	1469 ⁺¹²⁵ ₋₁₁₂	25.54 ^{+0.05} _{-0.04}
MUSE-122002035	JADES-GS+53.11984-27.83136	8.39 ^{+0.27} _{-0.34}	8.22 ^{+0.38} _{-0.46}	0.007 ^{+0.021} _{-0.005}	347 ⁺²⁶³ ₋₁₇₇	25.29 ^{+0.12} _{-0.04}
MUSE-123027133	JADES-GS+53.14468-27.83103	7.13 ^{+0.26} _{-0.04}	6.37 ^{+0.85} _{-0.29}	0.002 ^{+0.002} _{-0.001}	2109 ⁺¹⁷⁶ ₋₉₇₅	25.74 ^{+0.02} _{-0.02}
MUSE-124033068	JADES-GS+53.16604-27.82394	7.33 ^{+0.09} _{-0.06}	6.83 ^{+0.11} _{-0.08}	0.007 ^{+0.020} _{-0.006}	1267 ⁺¹²⁶ ₋₁₄₀	25.60 ^{+0.09} _{-0.10}
MUSE-125051124	JADES-GS+53.18845-27.81950	8.49 ^{+0.14} _{-0.12}	7.52 ^{+0.18} _{-0.17}	0.077 ^{+0.021} _{-0.043}	796 ⁺¹²⁴ ₋₁₁₀	25.58 ^{+0.10} _{-0.10}
MUSE-125052125	JADES-GS+53.17350-27.82507	7.23 ^{+0.05} _{-0.05}	6.28 ^{+0.18} _{-0.19}	0.012 ^{+0.021} _{-0.009}	1757 ⁺¹²⁵ ₋₁₃₆	25.75 ^{+0.01} _{-0.07}
MUSE-128044246	JADES-GS+53.12103-27.81599	7.34 ^{+0.08} _{-0.07}	7.09 ^{+0.10} _{-0.08}	0.004 ^{+0.011} _{-0.003}	1429 ⁺¹¹⁸ ₋₁₄₂	25.55 ^{+0.05} _{-0.04}
MUSE-128045247	JADES-GS+53.11988-27.82207	8.14 ^{+0.11} _{-0.10}	7.46 ^{+0.19} _{-0.13}	0.005 ^{+0.011} _{-0.003}	787 ⁺¹⁷⁴ ₋₁₅₇	25.54 ^{+0.09} _{-0.07}
MUSE-134036056	JADES-GS+53.13135-27.80687	7.88 ^{+0.06} _{-0.05}	7.03 ^{+0.07} _{-0.07}	0.004 ^{+0.011} _{-0.003}	1496 ⁺¹³⁴ ₋₁₄₆	25.54 ^{+0.08} _{-0.06}
MUSE-134037057	JADES-GS+53.13271-27.79899	7.22 ^{+0.07} _{-0.07}	6.91 ^{+0.09} _{-0.09}	0.003 ^{+0.007} _{-0.002}	1446 ⁺¹²⁶ ₋₁₂₄	25.86 ^{+0.04} _{-0.03}
MUSE-135049239	JADES-GS+53.12487-27.78413	8.68 ^{+0.12} _{-0.14}	8.31 ^{+0.18} _{-0.19}	0.038 ^{+0.061} _{-0.034}	364 ⁺⁶⁴ ₋₅₆	25.33 ^{+0.06} _{-0.03}
MUSE-139047301	JADES-GS+53.14289-27.75896	7.55 ^{+0.09} _{-0.09}	7.43 ^{+0.14} _{-0.12}	0.003 ^{+0.007} _{-0.002}	963 ⁺¹⁴³ ₋₁₄₄	25.48 ^{+0.08} _{-0.06}
MUSE-68	JADES-GS+53.17123-27.77852	8.00 ^{+0.07} _{-0.08}	7.17 ^{+0.11} _{-0.08}	0.005 ^{+0.013} _{-0.004}	1297 ⁺¹³³ ₋₁₂₃	25.52 ^{+0.06} _{-0.09}
MUSE-313	JADES-GS+53.17095-27.78251	7.35 ^{+0.08} _{-0.06}	7.25 ^{+0.08} _{-0.08}	0.002 ^{+0.006} _{-0.001}	1260 ⁺¹²⁰ ₋₁₃₄	26.03 ^{+0.06} _{-0.15}
MUSE-417	JADES-GS+53.15788-27.78007	7.39 ^{+0.09} _{-0.08}	7.29 ^{+0.15} _{-0.11}	0.005 ^{+0.013} _{-0.004}	1131 ⁺¹⁴⁰ ₋₁₅₈	25.52 ^{+0.07} _{-0.06}
MUSE-547	JADES-GS+53.16062-27.77161	7.65 ^{+0.13} _{-0.10}	7.30 ^{+0.15} _{-0.15}	0.007 ^{+0.019} _{-0.006}	1110 ⁺¹⁵² ₋₁₂₉	25.50 ^{+0.08} _{-0.06}
MUSE-1478	JADES-GS+53.15321-27.76623	8.49 ^{+0.24} _{-0.13}	7.18 ^{+0.40} _{-0.24}	0.112 ^{+0.026} _{-0.055}	967 ⁺¹⁷¹ ₋₁₇₈	25.85 ^{+0.14} _{-0.29}
MUSE-1670	JADES-GS+53.16674-27.80425	8.97 ^{+0.15} _{-0.15}	7.48 ^{+0.19} _{-0.21}	0.101 ^{+0.019} _{-0.023}	840 ⁺¹⁰³ ₋₉₈	25.46 ^{+0.06} _{-0.05}
MUSE-2069	JADES-GS+53.15105-27.78294	7.98 ^{+0.15} _{-0.11}	7.44 ^{+0.22} _{-0.15}	0.007 ^{+0.015} _{-0.005}	915 ⁺¹⁹⁶ ₋₁₆₉	25.49 ^{+0.08} _{-0.08}
MUSE-2071	JADES-GS+53.14615-27.77786	7.54 ^{+0.09} _{-0.08}	7.06 ^{+0.10} _{-0.07}	0.008 ^{+0.021} _{-0.006}	1434 ⁺¹³¹ ₋₁₃₃	25.54 ^{+0.05} _{-0.05}
MUSE-2168	JADES-GS+53.13600-27.79849	7.62 ^{+0.05} _{-0.03}	6.55 ^{+0.05} _{-0.03}	0.072 ^{+0.017} _{-0.019}	3122 ⁺²⁶⁹ ₋₂₃₇	25.77 ^{+0.05} _{-0.04}
MUSE-2296	JADES-GS+53.16836-27.80420	7.56 ^{+0.08} _{-0.07}	7.18 ^{+0.11} _{-0.09}	0.004 ^{+0.010} _{-0.003}	1306 ⁺¹⁴² ₋₁₄₈	25.54 ^{+0.07} _{-0.06}
MUSE-2302	JADES-GS+53.18044-27.77066	7.07 ^{+0.05} _{-0.04}	6.30 ^{+0.14} _{-0.20}	0.005 ^{+0.010} _{-0.003}	4401 ⁺⁴⁷⁷ ₋₅₄₄	25.80 ^{+0.06} _{-0.03}
MUSE-2307	JADES-GS+53.18335-27.79602	7.12 ^{+0.08} _{-0.07}	6.31 ^{+0.16} _{-0.19}	0.006 ^{+0.009} _{-0.004}	3764 ⁺⁴¹² ₋₃₅₅	25.94 ^{+0.15} _{-0.17}
MUSE-2350	JADES-GS+53.15638-27.80966	7.12 ^{+0.06} _{-0.06}	6.50 ^{+0.43} _{-0.32}	0.002 ^{+0.004} _{-0.001}	2321 ⁺⁴³⁶ ₋₉₇₆	25.60 ^{+0.03} _{-0.03}
MUSE-2449	JADES-GS+53.16470-27.76965	7.34 ^{+0.17} _{-0.09}	6.96 ^{+0.23} _{-0.11}	0.012 ^{+0.029} _{-0.010}	1125 ⁺¹⁸⁴ ₋₂₈₀	25.59 ^{+0.06} _{-0.10}
MUSE-2481	JADES-GS+53.14988-27.81073	8.39 ^{+0.15} _{-0.19}	8.06 ^{+0.24} _{-0.31}	0.044 ^{+0.023} _{-0.030}	539 ⁺¹⁴¹ ₋₁₀₆	25.40 ^{+0.10} _{-0.08}
MUSE-2502	JADES-GS+53.15807-27.81801	7.74 ^{+0.12} _{-0.11}	6.97 ^{+0.15} _{-0.19}	0.007 ^{+0.021} _{-0.006}	1409 ⁺²²⁴ ₋₁₃₈	25.57 ^{+0.06} _{-0.05}
MUSE-2873	JADES-GS+53.17252-27.76436	7.38 ^{+0.05} _{-0.04}	6.73 ^{+0.09} _{-0.06}	0.057 ^{+0.027} _{-0.024}	1677 ⁺²¹⁸ ₋₂₀₀	26.06 ^{+0.11} _{-0.15}
MUSE-2964	JADES-GS+53.14946-27.80980	7.15 ^{+0.14} _{-0.10}	6.96 ^{+0.16} _{-0.11}	0.020 ^{+0.037} _{-0.017}	1457 ⁺¹⁵⁵ ₋₁₈₀	25.58 ^{+0.08} _{-0.09}
MUSE-3090	JADES-GS+53.15491-27.76255	7.59 ^{+0.13} _{-0.08}	7.39 ^{+0.19} _{-0.13}	0.007 ^{+0.017} _{-0.005}	963 ⁺¹³⁷ ₋₁₃₆	25.51 ^{+0.07} _{-0.07}
MUSE-3093	JADES-GS+53.13969-27.79649	7.41 ^{+0.15} _{-0.17}	7.16 ^{+0.17} _{-0.17}	0.088 ^{+0.026} _{-0.034}	1149 ⁺¹⁹³ ₋₁₆₈	25.53 ^{+0.09} _{-0.07}
MUSE-3203	JADES-GS+53.17655-27.77112	7.58 ^{+0.09} _{-0.08}	7.09 ^{+0.12} _{-0.10}	0.002 ^{+0.005} _{-0.001}	1363 ⁺¹²⁴ ₋₁₂₃	25.55 ^{+0.08} _{-0.04}
MUSE-3238	JADES-GS+53.17560-27.79589	7.66 ^{+0.03} _{-0.03}	6.55 ^{+0.02} _{-0.01}	0.233 ^{+0.019} _{-0.018}	1197 ⁺¹⁰⁴ ₋₁₀₈	25.71 ^{+0.03} _{-0.01}
MUSE-4405	JADES-GS+53.17051-27.81249	7.42 ^{+0.10} _{-0.10}	6.87 ^{+0.14} _{-0.16}	0.006 ^{+0.019} _{-0.005}	1574 ⁺²⁴² ₋₁₄₄	25.54 ^{+0.06} _{-0.05}
MUSE-6231	JADES-GS+53.17834-27.80097	7.67 ^{+0.07} _{-0.07}	7.19 ^{+0.09} _{-0.09}	0.004 ^{+0.007} _{-0.002}	1229 ⁺¹⁰⁰ ₋₁₂₃	25.83 ^{+0.06} _{-0.06}
MUSE-6294	JADES-GS+53.16611-27.78574	8.10 ^{+0.07} _{-0.07}	6.82 ^{+0.11} _{-0.09}	0.136 ^{+0.020} _{-0.018}	1620 ⁺²⁰¹ ₋₁₇₇	25.73 ^{+0.10} _{-0.08}
MUSE-6462	JADES-GS+53.16407-27.79972	8.69 ^{+0.08} _{-0.10}	7.31 ^{+0.12} _{-0.12}	0.113 ^{+0.019} _{-0.027}	1054 ⁺¹²³ ₋₁₁₇	25.59 ^{+0.09} _{-0.07}
MUSE-7125	JADES-GS+53.12813-27.78987	8.72 ^{+0.10} _{-0.20}	8.29 ^{+0.25} _{-0.32}	0.004 ^{+0.010} _{-0.003}	249 ⁺⁸³ ₋₅₅	25.42 ^{+0.08} _{-0.08}
MUSE-7205	JADES-GS+53.16298-27.76031	7.19 ^{+0.09} _{-0.10}	7.03 ^{+0.13} _{-0.10}	0.005 ^{+0.013} _{-0.004}	1452 ⁺¹⁶⁵ ₋₁₉₀	25.64 ^{+0.06} _{-0.05}
MUSE-7225	JADES-GS+53.16167-27.76318	7.71 ^{+0.06} _{-0.06}	7.35 ^{+0.09} _{-0.07}	0.002 ^{+0.003} _{-0.001}	1211 ⁺⁸⁹ ₋₉₆	25.48 ^{+0.04} _{-0.03}
MUSE-7337	JADES-GS+53.16904-27.78769	7.39 ^{+0.15} _{-0.16}	7.09 ^{+0.18} _{-0.19}	0.069 ^{+0.025} _{-0.035}	1236 ⁺¹³² ₋₁₄₀	25.55 ^{+0.10} _{-0.07}
MUSE-7605	JADES-GS+53.16577-27.78490	7.13 ^{+0.09} _{-0.07}	6.83 ^{+0.11} _{-0.09}	0.005 ^{+0.013} _{-0.003}	1351 ⁺¹⁶² ₋₁₃₃	25.62 ^{+0.07} _{-0.06}
MUSE-7922	JADES-GS+53.18071-27.77656	8.58 ^{+0.25} _{-0.27}	8.02 ^{+0.37} _{-0.35}	0.111 ^{+0.041} _{-0.039}	524 ⁺¹⁸⁶ ₋₁₆₃	25.38 ^{+0.11} _{-0.08}
MUSE-7934	JADES-GS+53.14667-27.78621	8.72 ^{+0.12} _{-0.11}	7.91 ^{+0.21} _{-0.25}	0.006 ^{+0.023} _{-0.004}	410 ⁺⁸⁴ ₋₇₅	25.52 ^{+0.11} _{-0.08}
MUSE-7984	JADES-GS+53.17929-27.77331	7.77 ^{+0.09} _{-0.11}	7.17 ^{+0.12} _{-0.14}	0.061 ^{+0.019} _{-0.028}	1125 ⁺¹²¹ ₋₁₀₄	25.55 ^{+0.06} _{-0.05}
MUSE-8124	JADES-GS+53.15677-27.80921	8.51 ^{+0.09} _{-0.10}	7.79 ^{+0.15} _{-0.14}	0.063 ^{+0.017} _{-0.020}	429 ⁺⁷⁴ ₋₅₈	25.53 ^{+0.06} _{-0.05}
DEIMOS-11505	JADES-GN+189.26510+62.19963	7.88 ^{+0.10} _{-0.15}	6.25 ^{+0.16} _{-0.15}	0.024 ^{+0.020} _{-0.016}	3662 ⁺⁶⁹⁴ ₋₄₄₂	26.21 ^{+0.08} _{-0.09}
DEIMOS-43_13063	JADES-GN+189.15632+62.21000	8.76 ^{+0.17} _{-0.13}	7.51 ^{+0.24} _{-0.18}	0.155 ^{+0.028} _{-0.027}	853 ⁺¹²⁴ ₋₁₂₉	25.54 ^{+0.11} _{-0.11}
DEIMOS-33_19970	JADES-GN+189.23078+62.26355	7.88 ^{+0.08} _{-0.05}	7.20 ^{+0.08} _{-0.07}	0.004 ^{+0.008} _{-0.003}	1283 ⁺¹⁰⁸ ₋₁₄₀	25.54 ^{+0.05} _{-0.03}
DEIMOS-33_20014	JADES-GN+189.23125+62.25912	8.05 ^{+0.35} _{-0.07}	6.53 ^{+0.04} _{-0.17}	0.030 ^{+0.015} _{-0.015}	3261 ⁺²⁸⁰ ₋₂₇₃	25.96 ^{+0.32} _{-0.16}
DEIMOS-33_17440	JADES-GN+189.20512+62.26072	8.65 ^{+0.08} _{-0.07}	7.34 ^{+0.12} _{-0.09}	0.006 ^{+0.013} _{-0.004}	1052 ⁺¹³⁷ ₋₁₂₅	25.53 ^{+0.07} _{-0.07}
DEIMOS-vdrop_225	JADES-GN+189.18385+62.17992	7.36 ^{+0.09} _{-0.07}	6.43 ^{+0.07} _{-0.27}	0.002 ^{+0.004} _{-0.001}	4042 ⁺⁵⁵⁶ ₋₅₂₀	25.79 ^{+0.12} _{-0.18}
DEIMOS-33_17034	JADES-GN+189.20058+62.25945	8.13 ^{+0.06} _{-0.07}	7.25 ^{+0.09} _{-0.08}	0.002 ^{+0.004} _{-0.001}	1318 ⁺⁹¹ ₋₉₂	25.97 ^{+0.08} _{-0.08}
DEIMOS-33_17705	JADES-GN+189.20819+62.23212	7.99 ^{+0.10} _{-0.09}	7.13 ^{+0.12} _{-0.12}	0.021 ^{+0.027} _{-0.018}	1319 ⁺¹¹⁸ ₋₁₁₆	25.73 ^{+0.06} _{-0.16}
DEIMOS-32_16773	JADES-GN+189.19779+62.19996	7.71 ^{+0.08} _{-0.06}	7.19 ^{+0.18} _{-0.09}	0.005 ^{+0.012} _{-0.004}	1332 ⁺¹⁰² ₋₁₀₀	25.96 ^{+0.10} _{-0.09}

Table A2. Physical properties (median values and marginalized 68 per cent credible intervals) derived from BEAGLE models for the 61 Ly α emitters with H α detections at $4.9 < z < 6.5$ with JADES NIRCcam SEDs.